ABSTRACT

KIM, JEONG YONG. Development of a System-level Electrohydraulic Model and Recruitment State Transition Strategy for Improved Performance in Variable Recruitment Fluidic Artificial Muscle Tissues. (Under the direction of Dr. Matthew Bryant).

Fluidic artificial muscles (FAMs), also referred to as McKibben actuators, have excellent power-to-weight ratios, are inherently compliant, and are simple in design, consisting of an inner elastic bladder and an outer braided mesh. The double-helix pattern of the braided mesh allows the actuator to expand radially and contract axially when pressure is applied to the bladder. When multiple FAMs are bundled together in parallel and selectively pressurized, they can act as a multi-chambered actuator with bioinspired variable recruitment capability.

During operation of a variable recruitment bundle, different pressures are applied to each MU which inevitably results in a strain difference between MUs. This strain difference causes MUs that are inactive or at low pressures to become compressed and buckle outward. While increasing the spatial envelope of the entire bundle, buckled FAMs also exert a *resistive force* that opposes the force generation of active high pressure MUs. To better understand the force-strain characteristics of a FAM bundle, a model that captures these resistive forces of FAMs was developed. An analysis of the force-strain space of a FAM bundle using the developed model reveals an overlapping region between consecutive recruitment states in which the same force and strain combination can be achieved by either state. The resistive force model also reveals that there exists a non-zero pressure at which a FAM is no longer buckled and exerts a resistive force. This force has been coined the *de-slack pressure.*

Resistive forces and de-slack pressures are further investigated in terms of their implications on the electrohydraulic system level. A fully-coupled dynamic model of a variable recruitment FAM bundle system that includes the motor/pump, accumulator, and pressure control

valves is used to analyze the efficiency and bandwidth limits of the system. The resistive interaction effects present in between FAMs within a bundle have the greatest impact during a recruitment transition. An inverse dynamics approach is taken to solve for the required pressures of FAMs for a variable recruitment bundle to track a sinusoidal motion given the rate limitations imposed by the electrohydraulic system model. Simulations were then performed for different hydraulic circuit topologies and operating conditions such as continuous motor operation, intermittent motor operation and the use of a variable pump displacement. Simulation results showed that by using a variable displacement pump under continuous motor operation has the potential to increase the system efficiency while increasing the bandwidth limit at low recruitment states.

The system level analysis if taken a step further by applying the findings from system dynamics and the implications of resistive forces to develop and experimentally test a control scheme that is aimed to improve strain tracking performance during recruitment state transitions. The control of a variable recruitment bundle poses a hybrid control problem, one which requires the control of pressure as a continuous variable while simultaneously having to shift between discrete recruitment states. In practical applications, the recruitment of a new MU experiences a *recruitment lag* due to the limited flowrate and pressure dynamics of the system. An anticipatory method of estimating when a recruitment state shift must occur is used to take into account the recruitment lag and determine when the state transition timing. To mitigate the effects of resistive forces of newly-recruited MUs, a state-based compensation term is used to modify the pressure of previously-recruited MUs. The proposed control scheme is tested on the linear hydraulic actuator characterization device (LHACD) and used to track a sinusoidal trajectory with a hanging mass.

When compared to a baseline control scheme that uses state shift pressure thresholds, the proposed control scheme showed significant improvement in both the average and maximum strain errors.

Development of a System-level Electrohydraulic Model and Recruitment State Transition Strategy for Improved Performance in Variable Recruitment Fluidic Artificial Muscle Tissues

by
Jeong Yong Kim

A dissertation submitted to the Graduate Faculty of
North Carolina State University
in partial fulfillment of the
requirements for the degree of
Doctor of Philosophy

Mechanical Engineering

Raleigh, North Carolina
2023

APPROVED BY:

_____	_____
Dr. Matthew Bryant Committee Chair	Dr. Andre Mazzoleni
_____	_____
Dr. Katherine Saul	Dr. Chris Vermillion

DEDICATION

To my parents, sister and family;

To all my mentors and many friends;

To God.

BIOGRAPHY

Jeong Yong Kim received his B.S. degree in mechanical engineering from University of California, Berkely in 2012. In fulfillment of his military service to his country, he worked as a technical research personnel at T-Robotics for three years. He went on to pursue a M.S. degree in mechanical engineering from University of Minnesota, Twin Cities, which he finished in 2017. After working at LG Electronics for one year as a production engineering researcher, he began his Ph.D. program in mechanical engineering at North Carolina State University. His research interests are focused on the modeling and control of soft robotic systems.

ACKNOWLEDGMENTS

To my parents, I am grateful for their unconditional love and undying support not only through graduate school but also through all stages of my life. They are my first mentors and the models whom I will forever strive to be. I am also grateful for my loving sister who is on her own Ph.D. journey, for simply being there to share both the ups and downs of graduate school.

I am grateful for Dr. Matthew Bryant for the opportunity to join his lab and participate in his research. He guided me through my research with his knowledge, supported me with his heart, and challenged me to become better. I express my gratitude to my committee members Dr. Andre Mazzoleni, Dr. Katherine Saul, Dr. Chris Vermillion and Dr. Jason Patrick. I am also grateful to have worked with and learn from the many members of iSSRL.

Lastly, I gratefully acknowledge funding support for this research by the Faculty Early Career Development Program (CAREER) of the National Science Foundation under NSF Award Number 1845203 and Program Manager Irina Dolinskaya.

TABLE OF CONTENTS

LIST OF TABLES

LIST OF FIGURES

CHAPTER 1

Introduction

1.1 Motivation

The invention of the McKibben actuator dates back to the 1950s when Joseph McKibben first devised the concept for an arm orthosis for his polio-stricken daughter [1]. These actuators, often referred to as fluidic artificial actuators (FAMs), have excellent power-to-weight ratios, are inherently compliant, and are simple in design, consisting of an inner elastic bladder and an outer braided mesh. The double-helix pattern of the braided mesh allows the actuator to expand radially and contract axially when pressure is applied to the bladder. Making use of this mechanism, FAMs are conventionally used as contractile actuators. However, the simple construction and the versatility in the mesh mechanism has led researchers to develop actuators with other modes of actuation. By altering the initial braid angle, extensile FAMs can be created [2]. By adding inextensible layers to the mesh, they can be made to produce bending or twisting motion [3], [4]. These FAMs themselves can be used as end-effectors, as in a gripper that uses bending FAMs as fingers, or as stand-alone soft robots, like a crawling inchworm robot [5], [6]. Other research groups have focused on the arrangement of multiple FAMs in different configurations. Inspired by natural muscle fiber topology, FAMs can be arranged in a bipennate configuration to increase the force or contraction output through variable gearing kinematics [7], [8].

Another bio-inspired concept is the variable recruitment bundle actuator [9]–[11]. Our skeletal muscle tissues are made of smaller units of actuation called motor units (MUs) that are bundled together. In response to an increasing load, the MUs are not recruited simultaneously, but in a sequential manner in which they are activated in the order from smallest to largest, following Henneman's Size principle [12]. This concept can be applied to build a variable recruitment bundle

with multiple FAMs in parallel with one or more grouped together as a single MU. Depending on the load requirement of the bundle actuator, different MUs are activated to meet that demand. By segmenting the actuator into smaller activation units, it is able to operate closer to the source pressure thus lowering the amount of energy loss due to throttling for force control [9]. In terms of energetics, the same amount of mechanical work output can be produced with a smaller amount of fluid energy input during lower recruitment states. Therefore, the average efficiency of a variable recruitment bundle is higher compared to a single equivalent cross-sectional area motor unit (SEMU). In addition to increased overall efficiency, the decrease in fluid volume required to activate lower recruitment state MUs decreases the force sensitivity to applied pressure, allowing more precise control [9].

The performance of variable recruitment bundle actuators has been evaluated as an independent system under simplifying assumptions such as constant source pressure and in the absence of source flow rate dynamics. However, in reality, any hydraulic or pneumatic actuator and its control valve should be perceived as a subsystem that is part of a larger fluidic circuit system. This cannot be overlooked especially when the research direction is headed towards developing a variable-recruitment-actuated robotic system. A steady-state analysis of the electrohydraulic system has been done before for a rudimentary hydraulic architecture with different modes of pump operation [13]. However, other variations of architectures exist that can be hypothesized to further enhance the performance of a variable recruitment bundle system. Therefore, the purpose of this research is to perform a macro-level analysis of a robotic system that uses variable recruitment bundle actuators and explore the implication of different system architectures and develop recruitment state transition control strategies. This investigation begins with the modeling of the FAM subsystem and further expands its scope to include modeling on

the system level. Ultimately, the findings of this research will provide guidelines for designing any robotic system using variable recruitment FAM bundle actuators.

1.2 Research aims

1.2.1 Objective 1: Model the buckling behavior and resistive forces of FAMs in a variable recruitment bundle.

The first objective of this research is to develop a model for FAMs that is applicable to variable recruitment bundles. Current models in the literature predict the force output of FAMs during tensile operation, which was conventionally the only force regime of interest [14]–[19]. However, for a variable recruitment bundle with only a subset of MUs active, the interaction between active and inactive/low-pressure MUs necessitates the FAM model to predict forces in the compressive region. Due to the pressure-dependent nature of free strain, active MUs and inactive/low-pressure MUs have different strain, resulting in the compression of the latter. This usually results in the outward buckling of the FAM which increases the volume envelope of the actuator [9]. A model of the resistive force and the buckling behavior is developed and used to analyze the implications on a variable recruitment bundle [20], [21].

1.2.2 Objective 2: Develop a system-level electrohydraulic model to understand the implications of resistive and de-slack effects and the use of a variable displacement pump on variable recruitment.

The second objective expands the model scope from the downstream actuator to the entire electrohydraulic system. Conventional energetics analysis of variable recruitment bundles typically includes the FAM model and the assumption that the pressure applied to the FAMs are

controlled perfectly [13]. A system-level analysis using a holistic model including dynamic models of the hydraulic and electromechanical components such as the valve, pump and motor is the next step to understanding variable recruitment and its application to FAM-actuated robots. Chapman et al. developed an electrohydraulic model using the ideal FAM model and a fixed-displacement pump with continuous and intermittent operation [13]. This objective aims to expand this analysis to include the FAM model from the first objective and explore the implication of inter-FAM effects when system dynamics are considered. Furthermore, different hydraulic architectures and operating conditions such as the use of variable displacement pumps are explored. A variable displacement pump has the capability to vary the source pressure by changing the angle of its swashplate. As a large portion of the efficiency losses of a variable recruitment system comes from the throttling down of pressure, the use of a variable displacement pump is a potential method of increasing the overall performance of an electrohydraulic variable recruitment system.

1.2.3 Objective 3: Develop and test a recruitment state control strategy that optimizes position tracking performance during state transitions, based on the understanding of resistive forces and hydraulic system dynamics.

The third objective of this research is to build upon the understanding of resistive effects from the dynamic system analysis to develop and test a control scheme to improve the strain tracking performance of a variable recruitment bundle. Control of a variable recruitment bundle is a complex hybrid control problem in which the recruitment state must be determined as a discrete variable while simultaneously, the pressure is determined as a continuous variable [11], [22]. When considering a practical application in which pressure dynamics are present, the *recruitment lag* associated with transitioning to a new state must be considered. An anticipatory method of

estimating the amount of time required to make a state shift is proposed and used to determine the timing at which state shifts are made. The resistive forces of newly-recruited MUs are counteracted by increasing the pressure of previously-recruited MUs. The proposed control scheme is tested on the linear hydraulic actuator characterization device (LHACD) developed by Chipka et al. and its tracking performance is compared to a baseline control scheme of when state shift pressure thresholds are used [23].

Based on the understanding of resistive forces and hydraulic system dynamics gained from the previous aims, a recruitment state transition strategy can be devised to improve the tracking performance of a variable recruitment bundle during state transitions. Current evaluations of system performance neglect intricacies such as resistive and de-slack effects and the limitations in flowrate and pressure dynamics due to the system. In prior literature, the decision to shift between recruitment state have been made using pressure thresholds that are determined as a percentage of the nominal source pressure. The purpose of this study is to utilize the FAM and hydraulic system model developed from previous objectives to develop a model-based control scheme to inform when state transitions need to occur.

1.3 Dissertation structure

Chapter 2 focuses on the development of a FAM model that captures the resistive forces of FAMs in compression. The implications of inter-FAM resistive effects on a variable recruitment bundle such as the overlapping region between states in the bundle force-strain space and the free strain gradient reversal phenomenon is discussed. Chapter 3 focuses on using an electrohydraulic system model by incorporating the resistive force FAM model and investigating different circuit topologies. The resistive effects discussed in Chapter 2 are expanded to include dynamic effects

of a practical system. Three different case studies are presented: 1) continuous motor operation with constant pump displacement, 2) intermittent motor operation with constant pump displacement, and 3) continuous motor operation with variable pump displacement. Chapter 4 focuses on the design and testing of a control scheme using model-based compensation terms. The proposed control scheme has a cascaded PI-PI structure with a strain feedback outer loop and pressure feedback inner loop. Two compensation methods are presented: 1) lag compensation is used to account for the recruitment lag associated with system dynamics and 2) pressure compensation is used to account for resistive forces. The main contributions and future investigations are presented in Chapter 5.

CHAPTER 2

Modeling of Resistive Forces and Buckling Behavior in Variable Recruitment Fluidic Artificial Muscle Bundles[1]

Fluidic artificial muscles (FAMs), also known as McKibben actuators, are a class of fiber-reinforced soft actuators that can be pneumatically or hydraulically pressurized to produce muscle-like contraction and force generation. When multiple FAMs are bundled together in parallel and selectively pressurized, they can act as a multi-chambered actuator with bioinspired variable recruitment capability. The variable recruitment bundle consists of motor units (MUs)– groups of one of more FAMs - that are independently pressurized depending on the force demand, similar to how groups of muscle fibers are sequentially recruited in biological muscles. As the active FAMs contract, the inactive/low-pressure units are compressed, causing them to buckle outward, which increases the spatial envelope of the actuator. Additionally, a FAM compressed past its individual free strain applies a force that opposes the overall force output of active FAMs. In this paper, we propose a model to quantify this *resistive force* observed in inactive and low-pressure FAMs and study its implications on the performance of a variable recruitment bundle. The resistive force behavior is divided into post-buckling and post-collapse regions and a piecewise model is devised. An empirically-based correction method is proposed to improve the model to fit experimental data. Analysis of a bundle with resistive effects reveals a phenomenon, unique to variable recruitment bundles, defined as *free strain gradient reversal*.

[1] This chapter is published as a journal article in a special issue of MDPI Actuators []

2.1 Introduction

The McKibben actuator has received growing interest in the soft robotics community due to its high power density, inherent compliance, and simple design. It consists of an inner elastic bladder that is wrapped around by an outer braided mesh with a double-helical pattern. One end of the bladder is closed off while the other end is used to provide pressure to the bladder, either pneumatically or hydraulically. As the bladder expands due to internal pressure, the braided mesh constrains the bladder to expand radially while contracting axially. Due to this kinematic relationship of the braided mesh, the McKibben actuator has conventionally been used as a tensile actuator. When a constant pressure is applied, the actuator maintains an equilibrium force-strain state. In terms of control, the actuator can be said to be stable in open loop in response to constant pressure, while any displacement from its equilibrium state results in an opposing force [1]. Thus, it can be characterized as an active spring, a classification that can also be applied to a biological muscle, which is why it is also commonly referred to as a fluidic artificial muscle (FAM), a term that will be used interchangeably in this paper.

Due to this biomimetic behavior of FAMs, researchers have used it in a myriad of robotic applications, including robotic arms, prosthetics, and orthoses [3], [4], [24]–[28] Although typically used as contractile actuators, modifications to the design have allowed them to be used as extensile or bending actuators [2], [29]. Recent studies have extended the use of the FAM to multi-chambered bundles with variable recruitment functionality [9]–[11], [30]. Rather than a single FAM acting in isolation, multiple FAMs are bundled together in parallel connected by rigid end plates to form a single actuator, as shown in Figure 2.1. The idea of variable recruitment is biomimetic, based on the hierarchical scheme in which subgroups of muscle fibers, or motor units (MUs), within a mammalian muscle tissue are sequentially activated in order from smallest to

largest, a concept known as Henneman's size principle [12]. Compared to a single FAM with equivalent cross-sectional area, the variable recruitment bundle can achieve higher efficiencies. By adaptively recruiting the number of active MUs to meet the load demand, the bundle has the potential to reduce the losses that arise from throttling down the supply pressure. As a result, the variable recruitment bundle has a higher efficiency over a larger force-strain space than a single actuator with equivalent cross-sectional area [9], [30]. In addition, by selecting the size and number of FAMs in a MU for a desired force, the force sensitivity can be controlled, allowing for more precise control of the actuator force. The efficiency gains of variable recruitment have been demonstrated experimentally for both pneumatic and hydraulic systems [10], [31]. In addition, real-time switching control schemes for variable recruitment have been developed and tested [13], [30], and it has been shown that the use of variable recruitment in a hydraulic system with an intermittent pump operation scheme can increase both efficiency and bandwidth when compared to a single actuator [13]. Due to both the compliant and hierarchical nature of variable recruitment, FAM bundles can experience a unique phenomenon during actuation: the compression and buckling of inactive MUs. These inactive FAMs generate a resistive force as the bundle contracts, resulting in a bundle force output and free strain that is lower than what would be predicted using a model or experimental characterization of a single FAM and applying it to a bundle [9].

Previous analytical variable recruitment studies have not accounted for resistive forces within a bundle, relying on either ideal virtual-work based models, such as the one presented by Tondu, or semi-empirical corrected models, such as the one presented by Meller et al. [1], [31]. These semi-empirical models correct the ideal model by accounting for pressure-dependent free strain that exists due to bladder elasticity, but they do not examine FAM forces past free strain, and therefore cannot account for resistive forces of buckled or post-free strain FAMs within a

variable recruitment bundle. In all the variable recruitment simulations or controller developments that exist in the literature, the force exerted by FAMs past free strain is assumed to be zero; in essence, the FAM is assumed to neither contribute positively nor negatively to overall bundle force production. However, resistive forces have been experimentally observed to contribute negatively to bundle force production [20]. In this paper, we propose a method of modeling these resistive forces and study their implications on the overall force output of a variable recruitment bundle. It is important to understand to what extent these resistive forces affect overall bundle performances, as this information will aid in the development of optimal bundle designs for a given application as well as improved variable recruitment controller performance. It should be noted that, although the motivation for modeling the resistive force comes within the context of a variable recruitment bundle, the analysis can be extended to any FAM that is compressed past its free strain.

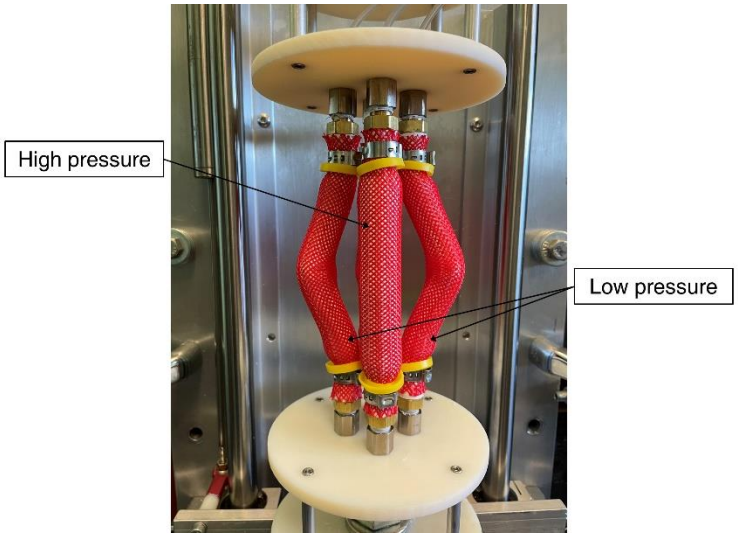

Figure 2.1: Variable recruitment FAM bundle that consists of multiple MUs in parallel connected at each end by rigid plates. A MU is the smallest unit of activation and can consist of one or more FAMs. Inactive/low-pressure MUs buckle outward as active MUs contract.

The remainder of this paper is organized in the following way. In Section 2.2, conventional methods of modeling the quasi-static force output up to free strain are introduced, giving us insight into how the total force can be decomposed. Section 2.3 begins with a qualitative description of the different regions of resistive force in FAMs compressed past free strain. The modeling of resistive force for each region is discussed in detail in the same section. In Section 2.4, the implications of resistive forces on the overall performance of a variable recruitment bundle are explored. In Section 2.5, an empirically-based correction method is proposed to better match experimental results. Section 2.6 presents a phenomenon we refer to as 'bundle free strain gradient reversal' and discusses its implication to bundle design. The conclusions of the paper are presented in the final section.

2.2 Quasi-static Modeling of Tensile Force Generation

Prior to modeling the resistive force, we first need an understanding of the quasi-static forces in the tensile force generation regime (i.e., for strains less than the FAM free strain). Chou and Hannaford [19] proposed a model based on the balance between the virtual work done by the equilibrium force F and internal pressure P which is expressed as:

$$-F\delta l = P\delta V \tag{2.1}$$

where δl is the variation of axial length and δV is the variation of the fluid volume upon which the pressure acts. A kinematic relationship can be derived between the instantaneous radius r, and length l, of the actuator based on the initial braid angle α_0 of the braided mesh, given as:

$$r = r_0\left(\frac{\sqrt{1 - cos^2\alpha_0(l/l_0)^2}}{sin\alpha_0}\right) \tag{2.2}$$

where r_0 is the initial radius and l_0 is the initial length of the braided mesh. By combining these equations, the expression for F_{mesh} can be expressed in terms of the internal pressure P, and strain ε.

$$F_{mesh} = \pi r_0^2 P \left(\frac{1}{tan^2 \alpha_0} (\varepsilon - 1)^2 - \frac{1}{sin^2 \alpha_0} \right) \quad (2.3)$$

This force will be referred to in this paper as the mesh force, as it expresses the force due to the internal pressure that is converted into axial force using the kinematic constraints of the braided mesh. From this formulation, we can see that the force output is a function of strain. Since the advent of this model, researchers have further developed models to account for the wall thickness of the bladder, tapered geometry of the bladder at its ends, and friction between the bladder and braided mesh [1], [14]. Although this model gives us the relationship between the pressure and the axial force output of the actuator due to the kinematic constraint imposed by the braided mesh, it is not able to predict the pressure-dependent nature of free strain. For a given pressure, maximum actuator force occurs at zero strain, which is also known as the blocked force condition. The strain at which the force is zero is known as the free strain, which is constant for all pressures when using (2.3). Experimental observation of isobaric force-strain curves tells us that the free strain increases with increasing pressure [31]. This pressure-dependent nature of free strain can be accounted for by the bladder elastic forces that oppose the mesh force output. Therefore, the bladder elastic forces are an integral component in understanding the force-strain relationship and have been incorporated into many models. Klute and Hannaford use the Mooney-Rivlin strain energy function W, and apply the principle of virtual work to model the elastic bladder force [18]. Kothera et al. further improved the elastic force term of the model by accounting for changes in bladder thickness [15]. Including the elastic bladder force term, the total force of a FAM is expressed as:

$$F_{total} = F_{mesh} + F_{bladder} = P\frac{dV}{dL} - V_b\frac{dW}{dL}, \quad (2.4)$$

where V_b denotes the volume of the bladder. Other models take a force balance approach to model the elastic forces by analyzing the stresses developed in the bladder in the hoop and axial directions [16], [17]. The mesh force derived from this approach matches the results from the virtual work balance method, as expected. For this study, the model developed by Klute and Hannaford will be used for forces up to free strain, with the addition of an empirical correction factor that will be discussed in detail in Section 2.5.

For the tensile force generation regime of the FAM, we note from the models discussed previously that the total axial force production of the actuator can be divided into two components: the contractile force generated by fluid pressure acting on the braided mesh due to the mesh kinematics, and the opposing force that acts against contraction due to the elasticity of the bladder. This idea serves as a basis for understanding the force-strain behavior of a FAM and is valid for force past free strain as well. Therefore, in modeling the resistive forces, the mesh and bladder forces will be modeled separately and summed to give the total force in the resistive force regime.

2.3 Resistive Force Modeling

2.3.1 Experimental Observations of Post-Free Strain FAM Behavior

Prior to presenting the modeling of the resistive force in the post-free strain (compressive) regime, we first present a qualitative description of the post-free strain behavior of a FAM based on our experimental observations. From these observations, the FAM behavior can be divided into two distinct regions: (1) the post-buckling region and (2) the post-collapse region. Immediately after the actuator is compressed past free strain and enters the resistive force-strain regime, the actuator exhibits deflection in the transverse direction due to buckling of the bladder. This behavior is

referred to as the post-buckling region. While classical column theory predicts that an axially-loaded, hollow cylindrical column such as the FAM bladder will experience linear axisymmetric deformation until a critical load is reached, experimental investigations have established that the classical critical load often overpredicts the load at which buckling occurs in practice [32]. The actual buckling load has been shown to be highly sensitive to geometric imperfections, both in the buckling specimen and in the end constraints of the column [33]. McKibben actuators in practical applications often operate in conditions in which the end constraints may not be perfectly aligned or are subject to perturbations. Therefore, in keeping with our experimental observations, we assume that the FAM bladder enters post-buckling immediately beyond the free-strain condition. As compressive strain is further increased, a second region of behavior begins when the bladder tube collapses; this region is referred to as the post-collapse region. In the literature on the bending of a hollow cylindrical beam with internal pressure, collapse is considered a structural failure that occurs due to significant deformation of the cross-sectional area of the beam from its circular shape [34]. For a column with clamped-clamped end constraints, the maximum internal moments occur at each end and at the middle. When this moment exceeds the collapse moment, the bladder folds upon itself, effectively acting as a 'hinge'. The end of the post-buckling region is defined by the collapse moment and the system then transitions to the post-collapse region.

The post-buckling and post-collapse regions make up the post-free strain regime of a McKibben actuator and govern the generation of resistive force. Figure 2.2 shows the FAM (a) at free length, (b) at free strain, which defines the beginning of the post-buckling region, (c) during the post-buckling region, and (d) during the post-collapse region in which the internal moment generated has reached the collapse moment. The post-collapse region follows immediately after

collapse and continues for the remaining strain range until the maximum strain of the actuator is reached. The following sections will address the quasi-static force modeling of each region.

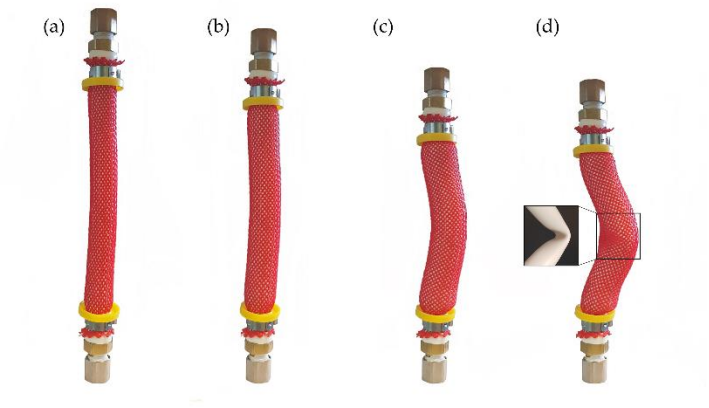

Figure 2.2: The progression of a FAM contracting from its free length (a), up to free strain (b), and into the resistive force regime. In the post-buckling region (c), the bladder is deformed into the first mode shape of a clamped-clamped column. The bladder enters the post-collapse region (d) as the bladder cross-section deforms from its initial circular shape.

2.3.2 Post-buckling region

The axial force required to maintain static equilibrium of the bladder in the post-buckling shape is solved using the principle of virtual work. For equilibrium, the first variation of the total potential energy, which is the potential energy stored in the bladder due to bending minus the work done to the system by external forces, needs to be zero and is expressed as:

$$F_b \delta x = \delta U_b, \tag{2.5}$$

where F_b is the additional force exerted by the bladder past free strain, and x is the amount of compression past free strain. U_b is the potential energy stored due to bending of the bladder expressed as:

$$\delta U_b = \int_0^L \frac{EI}{2} \kappa^2 dz, \tag{2.6}$$

where E is the Young's modulus of the bladder material, $I = 0.25\pi\left(r_0^4 - r_{inner,0}^4\right)$ and is the second moment of inertia, and κ is the curvature due to the bent shape.

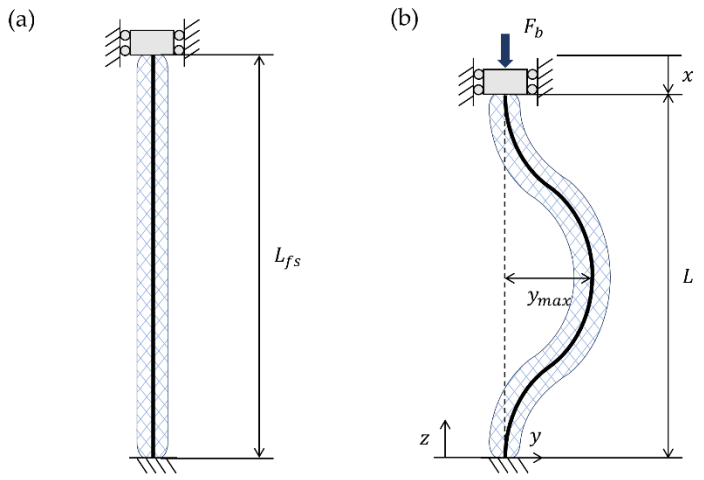

Figure 2.3: Parameters of McKibben actuator at free strain (a) and in post-buckling state (b)

From classical beam theory, the curvature can be approximated as:

$$\kappa = \frac{d^2y}{dz^2}, \tag{2.7}$$

The transverse deflection y of the bladder in the post-buckling region is given as:

$$y(z) = y_{max}\phi(z) = \frac{y_{max}}{2}\left[cos\left(\frac{2\pi}{L}z\right) - 1\right], \tag{2.8}$$

which is expressed by multiplying the maximum transverse deflection y_{max}, at the middle of the column and the first mode shape of a clamped-clamped column, $\phi(z)$. This first mode shape is used, as higher mode shapes for a column under axial load occur only when the corresponding nodal points are physically restrained [32], which is not true for the case we are analyzing. The bladder is first assumed to have no axial deformation, which allows us to solve for y_{max} by setting the expression for the axial deformation of a largely deformed column to zero [35].

$$\varepsilon_{axis} = \frac{dx}{dz} + \frac{1}{2}\left(\frac{dy}{dz}\right)^2 = 0. \tag{2.9}$$

$$y_{max} = \frac{\sqrt{4x(L_{fs}-x)}}{\pi}. \tag{2.10}$$

ε_{axis} is the strain along the axis of the column, which should not be confused with actuator strain. The first term in (2.9) simply is the strain in the axial direction due to extension. The second term is the contribution of finite rotations in the column to axial strain. The transverse deflection is expressed in terms of the actuator length at free strain L_{fs}, which is shown in Figure 2.3. Substituting the equations for maximum transverse deflection and curvature into (2.6) and performing the integral gives us an expression of the energy stored in the bladder as a function of the amount compressed.

$$U_b = \frac{4EI\pi^2 x}{(L_{fs}-x)^2}. \tag{2.11}$$

Performing the first variation of (2.11) and substituting into (2.5), the axial force exerted by the bladder due to bending is expressed as:

$$F_b = \frac{4EI\pi^2(L_{fs}+x)}{(L_{fs}-x)^3}. \tag{2.12}$$

It should be noted that the force from (2.12) is derived under the assumption that no axial deformation occurs. Thus, the arc length of the bladder remains constant and equal to the bladder length at free strain. However, this is not representative of the actual system in which stresses in the axial direction cause some amount of deformation and shortening of the arc length. This change in arc length is not the same as that of a simple column under axial load, as the braid kinematics affect the bladder length as well. Moreover, the actual system is far from ideal, as it contains geometric imperfections, as discussed previously. As a simple approximation of these effects, we

propose an equivalent spring system to approximate a corrected bladder force F_b' in the post-buckling region that accounts for axial deformation and non-ideal conditions.

Consider a system of springs that consists of a transverse spring and two springs oriented in the axial direction of the bladder, as shown in Figure 2.4. The transverse spring constant k_1 represents the bending rigidity of the bladder and any compression in the axial direction results in deformation of the transverse spring, causing an opposing axial force.

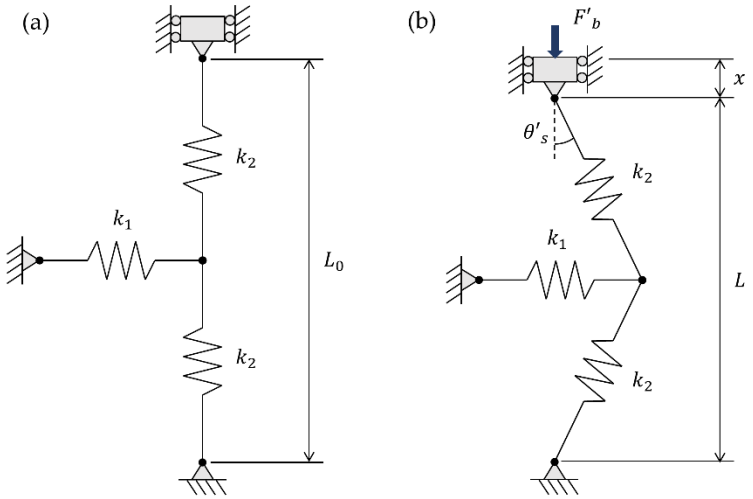

Figure 2.4: Parameters of equivalent spring system in the free strain (a) and in post-buckling state (b).

The force expression derived in (2.12) can be considered to be the case in which the axial spring constant k_2 is a very large value such that no deformation occurs in those springs. Calculating F_b and using the corresponding value of y_{max} as the deformation in the transverse spring, an expression for equivalent spring stiffness k_1 can be found as:

$$k_1 = \frac{2F_b}{y_{max} sin\theta_s cos\theta_s}. \tag{2.13}$$

$$\theta_s' = cos^{-1}\left(\frac{L_{fs}-x}{L_{fs}-2l}\right). \tag{2.14}$$

where θ_s' is the angle between the vertical axis and the axial spring, and θ_s is a special case for when the deformation in the axial spring $l = 0$ in (2.14). For a given amount of compression x, let us assume this spring stiffness is constant; yet it varies as the actuator is compressed and x changes. Given a value for k_1 and assuming a value for k_2 as the axial rigidity of the bladder, a relationship can be derived between the deformation in the transverse spring with axial deformation y_{max}' and l.

$$y_{max}' = \frac{k_2}{k_1}\frac{4l}{sin\theta_s'}. \tag{2.15}$$

The corrected post-buckling force with axial deformation is expressed as:

$$F_b' = \frac{1}{2}k_1 y_{max}' sin\theta_s' cos\theta_s' = \frac{y_{max}' sin2\theta_s'}{y_{max} sin2\theta_s}F_b. \tag{2.16}$$

Note that F_b' only accounts for the additional force exerted by the bladder past free strain. The total bladder force is a sum of the bladder force required to reach free strain $F_{bladder}(\varepsilon_{free})$, which is the bladder force from (2.4) evaluated at free strain ε_{free}, and F_b'. Furthermore, the total force in the post-buckling region is the sum of forces due to the braided mesh and the bladder, just as it is with the force before free strain. In the typical case of tensile contraction, the mesh deforms axisymmetrically by expanding radially while contracting axially. In such a case, the mesh force is a function of the instantaneous actuator length, as expressed in the ideal mesh force equation. Following the same principle, the mesh force in the post-buckling region remains a function of the braided mesh length; however, that mesh length is no longer the length of the actuator. Since the mesh deforms asymmetrically with some transverse deflection, mesh force becomes a function of the arc length of the buckled shape. The asymmetric mesh force is denoted F_{mesh}', for which computation is identical as (2.3**)** but uses the arc length instead of actuator length. Figure 2.6

illustrates the difference between F_{mesh} and F'_{mesh}. The forces up to free strain for both cases are obviously the same. However, as free strain is reached, the solid lines show axisymmetric deformation while the dashed lines show the forces as the bladder is bent into its post-buckling shape.

As the bladder is compressed further and continues to bend, the internal moment along the beam increases until it reaches the collapse moment. Due to its complex nature, the collapse moment of elastic inflatable tubes is a standalone research topic and has been extensively studied in various papers [36]–[39]. The earliest of models assume a cylindrical membrane with an applied internal pressure [34]. These models predict a collapse moment that is a linear function of pressure. Improvements to these models have taken into account the material properties of the bladder and some have used experiments to correct for discrepancies [37], [38]. The collapse moment adapted in this paper is a classical formulation in the field of bending inflatable bladders developed by Wood in 1958 [36]:

$$M_{collapse} = \frac{2\sqrt{2}}{9}\pi E r_0 t_0^2 \sqrt{\frac{1}{1-\nu^2} + \frac{4P}{E}\left(\frac{r_0}{t_0}\right)}. \tag{2.17}$$

where t_0 is the initial bladder wall thickness and ν is Poisson's ratio, which is assumed to be 0.5. Once the maximum internal moment generated in the post-buckled bladder reaches this collapse moment, the model detailed in this section no longer applies and proceeds to the post-collapse region, for which the model is described in the following section.

2.3.3 Post-collapse region

The virtual work balance modeling approach taken for the post-collapse region is similar to that taken for the post-buckling region, but with a different mode shape and a torsional spring to represent the 'hinge' at the middle of the column due to bladder collapse. The proposed model

does not account for the subtle transitional effects that occur between the post-buckling and post-collapse regions, such as the change in cross-sectional area. As a result, the resistive force is expressed in terms of two force equations corresponding to each region, resulting in a piecewise discontinuous model. After the derivation of the post-collapse force model is described, a simple method of making the transition between the two regions will be proposed.

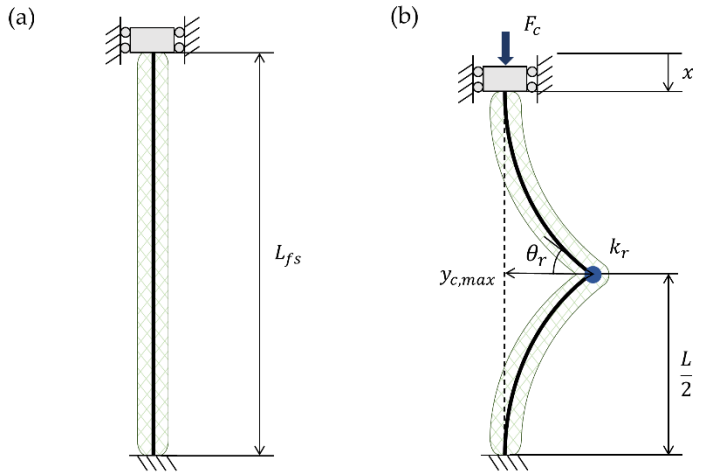

Figure 2.5: Parameters of McKibben actuator at free strain (a) and in the post-collapse region represented by the clamped-hinged-clamped column mode shape (b)

The assumed post-collapse mode shape is shown in Figure 2.5. It consists of two clamped-free columns connected at their free ends by a torsional spring with constant k_r. It is assumed that the torsional spring does not affect the boundary condition of the columns. Upon calculating the internal moment along the column based on the post-buckling mode shape, the magnitude of moment is greatest at each end and at the middle of the column. From the observation of the fact that FAM collapse occurs at one area at which it is most vulnerable, the mode shape is devised to create a hinge at the middle of the column which is represented by a torsion spring with some

stiffness. As done for the post-buckling force, the first variation of the total potential energy is set to zero for equilibrium.

$$F_c \delta x = \delta(2U_c + U_r). \tag{2.18}$$

For the post-collapse region, the strain energy stored in the column consists of energy stored in each clamped-free column and the torsional spring given as:

$$U_c = \int_0^{L/2} \frac{EI}{2} \kappa_c dz. \tag{2.19}$$

and

$$U_r = \frac{1}{2} k_r (2\theta_r)^2. \tag{2.20}$$

κ_c is the curvature of the clamped-free column, which is approximated by:

$$\kappa_c = \frac{d^2 y_c}{dz^2}. \tag{2.21}$$

where the transverse deflection in the post-collapse region y_c is expressed as:

$$y_c = y_{max} \phi_c(z) = y_{max} \left[1 - cos\left(\frac{\pi}{L} z\right)\right]. \tag{2.22}$$

where ϕ_c is the first mode shape of the clamped-free column. The torsional spring stiffness k_r is formulated by assuming the bladder has collapsed completely such that the inner walls of the bladder are in contact. Under this assumption the local radius of curvature is estimated by the wall thickness. The local cross-sectional area is assumed to be an ellipse and the second moment of inertia $I_r = \pi r_0 {t_0}^3/4$ is used. Therefore, the torsional spring stiffness is expressed as:

$$k_r = \frac{EI_r}{2\theta_r t_0}. \tag{2.23}$$

where θ_r is the between the column and the horizontal axis as shown in Figure 2.5. The angular displacement of the torsional spring is $2\theta_r$ and can be calculated from the slope of the column's

free end by taking the derivative of the transverse deflection and evaluating it at the middle. The angle between the column and the horizontal axis is given as:

$$\theta_r = arctan\left(\sqrt{\frac{x}{L_{fs}-x}}\right). \tag{2.24}$$

Taking the first variation of the sum of strain energy terms and substituting into (2.18) gives the expression for the post-collapse force.

$$F_c = \frac{IE\pi^2 L_{fs}}{4\left(L_{fs}-x\right)^2} + \frac{2k_r\sqrt{x/\left(L_{fs}-x\right)}\,tan^{-1}\left(\sqrt{x/\left(L_{fs}-x\right)}\right)}{x}. \tag{2.25}$$

Combining the post-buckling region force from (2.16) and (2.25) results in a piecewise model with a discontinuity at the collapse strain. This is to be expected due to the change in mode shape. The proposed mode shape used for the post-collapse region is representative of the column shape at strains much closer to the maximum strain rather than immediately after the collapse strain. Thus, this mode shape can be used to calculate the force to which the post-collapse region force converges at large strain. In the actual system, a much more gradual transition is observed as the cross-sectional area at the middle of the column deforms from its circular shape to an elliptical shape. The change in cross-sectional area that contributes to the geometric nonlinearity of the system can be applied to both the post-buckling and post-collapse regions. The most widely referenced analysis of this behavior is the study by Brazier on the change in moment due to change in cross-sectional area shape and the theory on inflatable structures [34], [39]. However, we propose a much simpler approach that approximates the transition from the post-buckling to post-collapse force as a first-order response formulated as the following.

$$F_c' = F_b' e^{-\beta(\varepsilon-\varepsilon_c)} + F_c\left(1-e^{-\beta(\varepsilon-\varepsilon_c)}\right) \tag{2.26}$$

$$= F_c + (F_b' - F_c)e^{-\beta(\varepsilon-\varepsilon_c)}.$$

The modified post-collapse force begins at the collapse strain ε_c, and is characterized by a transition rate constant β which is a parameter that can be tuned manually or through parameter optimization based on empirical data.

2.3.4 Summary of Resistive Force Piecewise Model

The piecewise model for the entire range of strain can summarized as below.

$$F_{total} = \begin{cases} F_{mesh} + F_{bladder} & F_{mesh} > F_{bladder} \\ F'_{mesh} + F_{bladder}(\varepsilon_{free}) + F'_b & F_{mesh} \leq F_{bladder} \ \ and \ \ M_b < M_{collapse} \\ F'_c & M_b \geq M_{collapse} \end{cases} \quad (2.27)$$

The criterion for the first piece is for strains below free strain. For F_{mesh} and $F_{bladder}$, any of the existing models can be used as long as they can be divided into those two force components. The second and third pieces are for the post-buckling and post-collapse regions, respectively.

Figure 2.6 shows the FAM force strain-curve for pressures (a) 0 kPa, (b) 34.5 kPa, (c) 137.9 kPa, and (d) 344.7 kPa for a FAM with an initial outer radius of $6.35 \times 10^{-3}\ m$ $(0.5\ in.)$, initial bladder wall thickness of $1.6 \times 10^{-3}\ m$ $(0.0625\ in.)$, and initial length of $0.127\ m$ $(5\ in.)$. The initial braid angle was assumed to be 33 degrees. The bladder is a commercial silicone tube with a Young's modulus of $1.78\ MPa$ as determined by a simple uniaxial tensile test. Figure 2.6(a) shows the resistive force of an inactive FAM. As no pressure is applied, no mesh force is present and only bladder forces exist. Figure 2.6(b) shows the resultant total force F_{total} as well as the breakdown of the all force components shown in (2.27). The tensile force region consists of the conventional force-strain relationship up to free strain as shown by the Klute-Hannaford model. After free strain, the post-buckling region begins, and both the mesh and bladder forces deviate from the Klute-Hannaford model. In this region, the bladder is in the post-buckled shape and

internal moment is generated along the bladder. When the maximum value of that internal moment exceeds the collapse moment, the resistive force shows a decrease in magnitude (i.e., becomes less negative). This happens during the post-collapse region for which the magnitude of resistive force remains less than its maximum value at collapse. Figure 2.6(b) and (c) illustrate the resistive force regime at higher pressures. For the pressure of 137.9 kPa, only the post-buckling region is shown as the bladder does not collapse before the maximum strain tested. As the applied pressure increases, the free strain increases, thus decreasing the resistive force regime until it is no longer of concern when the applied pressure reaches the maximum operating pressure as in (c). Therefore, the significance of the resistive force model is highlighted during lower pressures when the discrepancy between the resistive model and Klute-Hannaford model is greater as shown by the curves F_{total} and $F_{mesh} + F_{bladder}$ in (b). As shown in Figure 2.6(a) and (b), the proposed model shows a good qualitative agreement with the low-pressure FAM behavior past free strain, however quantitative discrepancies between the model and experimental data exist. To account for such discrepancies, empirical tuning of parameters can be performed in both the tensile and resistive force regimes to yield a better match as discussed in Section 2.5.

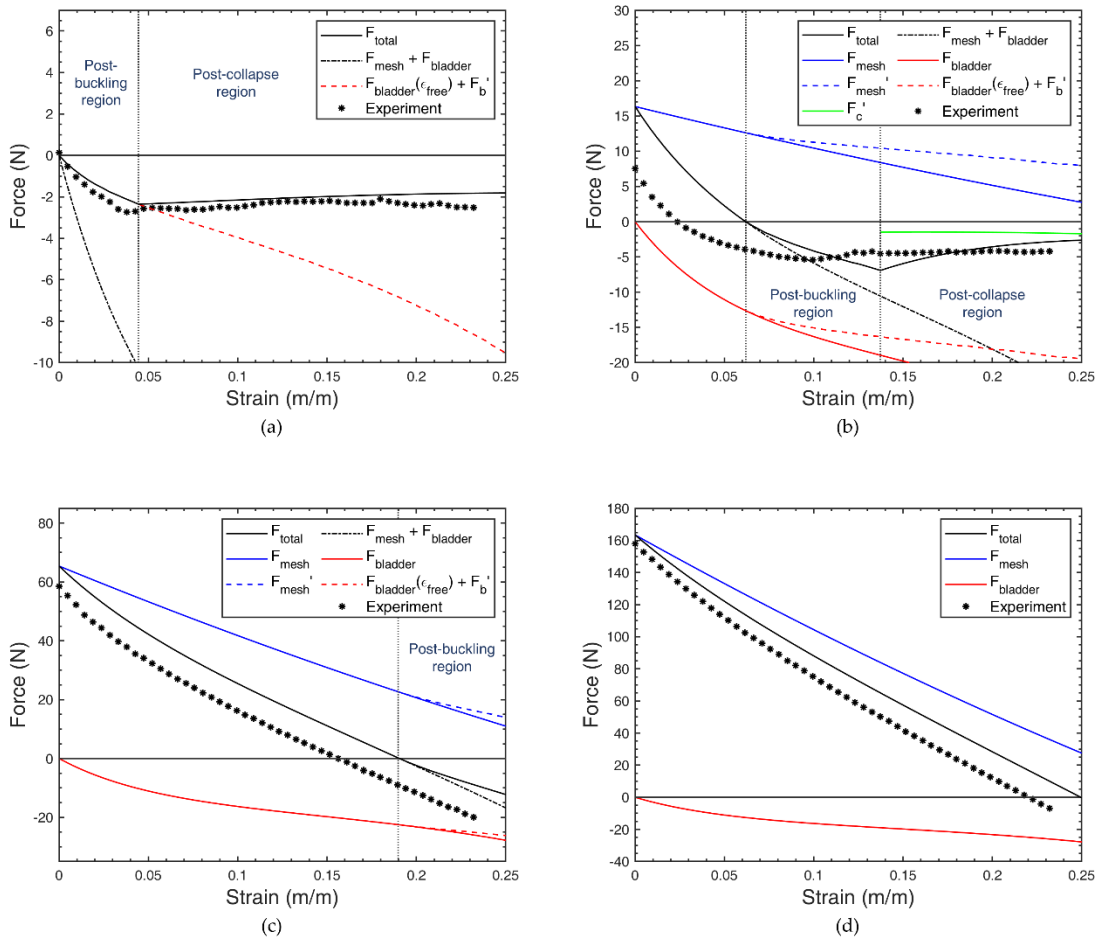

Figure 2.6: Breakdown of model forces along with corresponding experiment results for (a) 0 kPa, (b) 34.5 kPa, (c) 137.9 kPa, and (d) 344.7 kPa. The resultant force from the piecewise model is shown in solid black as well as force components shown in (2.27).

Figure 2.7 demonstrates the effect of the transition constant used to characterize the transition from post-buckling to post-collapse region discussed in (2.26). Lower values of βs characterize a gradual transition to the post-collapse state. In generating the model curves of Figure 2.6, a preliminary value of 25 was used. The transition constant is one of the parameters used to empirically tune in Section 2.5 using an empirically-based parameter tuning.

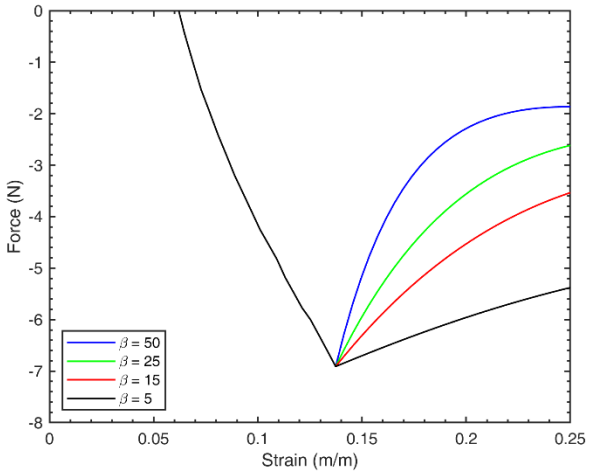

Figure 2.7: Effect of transition constant β used to characterize the transition from post-buckling to post-collapse region. The resistive forces are shown for a FAM with identical dimensions as that of Figure 2.6 and for an applied pressure of 34.5 kPa.

2.4 Effect of resistive force on overall performance of a variable recruitment bundle

The results of this new model are particularly significant within the context of a variable recruitment bundle. A conventional FAM model, such as the ideal or Klute-Hannaford model, was not intended for forces past free strain and the magnitude of the resistive force continues to increase as strain increases past free strain. During operation of a variable recruitment bundle, inactive or low-pressure FAMs are compressed significantly past their free strain, for which conventional models would predict a much greater magnitude of resistive force than what is present. Instead of a steady increase in resistive force magnitude past free strain as shown by $F_{mesh} + F_{bladder}$ in Figure 2.6, the proposed model better predicts the force behavior of FAMs past free strain. Therefore, this model is more suited to predict the overall force output of a variable recruitment bundle.

The force-strain curves for a simple variable recruitment bundle actuator consisting of two MUs, each made of one identical FAM, were generated. The bundle can be in two different states of operation called *recruitment states* (RS). The two primary variable recruitment schemes that have been used in previous work are called batch recruitment and orderly recruitment [22], [30]. Orderly recruitment will be assumed for this analysis, and Figure 2.8 shows a graphical depiction of the activation sequence for this recruitment scheme. In the first recruitment state, only one MU is activated (i.e. pressurized), and the other MU is inactive. A recruitment state can either be partially or fully activated depending on the pressure supplied. It is fully activated when the corresponding MU pressure is at its maximum.

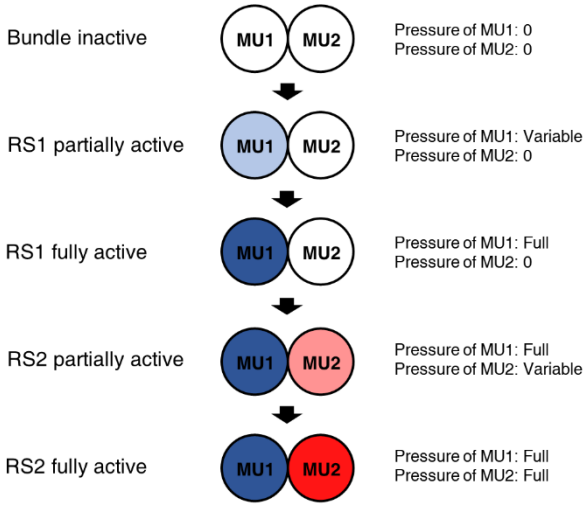

Figure 2.8: Orderly recruitment activation scheme for a bundle with two recruitment states.

2.4.1. Quasi-static force-strain space for variable recruitment bundle with resistive forces

Figure 2.9 shows the force-strain curves for a variable recruitment bundle with two recruitment states with and without resistive forces included in the analysis. The force curves plotted in blue show the force-strain relationship of the first recruitment state. Once the first

recruitment state is fully activated, the bundle can enter its second recruitment state, during which the first MU stays at its maximum pressure and a second MU is either partially or fully activated. The red isobaric curves show the force-strain space for the second recruitment state. To illustrate the increase in pressure of the MU of a recruitment state, higher pressures are depicted in relatively thicker lines. In this scenario, quasi-static force curves were plotted for pressures between 0 kPa and 413.7 kPa at 68.9 kPa intervals. The FAMs used in this simulation are assumed to have an initial length of 0.127 m, initial outer radius of 0.009 m, a radius-to-wall thickness ratio of 0.25, and an initial braid angle of 33 degrees. The force-strain space of Figure 2.9(a) is generated by neglecting the resistive forces and assuming any forces past free strain to be zero. A more realistic case is presented in (b) in which the resistive forces are included in the overall bundle force.

The key difference observed from the force-strain space of a bundle with resistive effects is an overlapping region between the first and second recruitment states that becomes prominent during strains near the maximum bundle free strain. As shown in Figure 2.9 (a), the boundary between recruitment states 1 and 2 is distinct when resistive forces are neglected. As the first MU is fully activated, any additional pressure supplied to the second MU, transitioning to the second recruitment state, either increases or maintains the force output of the bundle. In Figure 2.9 (c), the pressures applied to MU 2 are indicated for a bundle model with resistive forces are neglected. When a pressure of 275.8 kPa is supplied to the second MU, the model predicts that the force will increase for strain values less than 0.24. However, applying the same pressure for strains greater than 0.24 is predicted to not affect the force output of the bundle. This occurs because free strain is pressure-dependent and the free strain generated by the MU 2 FAM at these pressures is less than the bundle strain. Thus, for a specific force-strain output, the required operating state of the bundle can be easily categorized into either recruitment state 1 or 2. However, when resistive

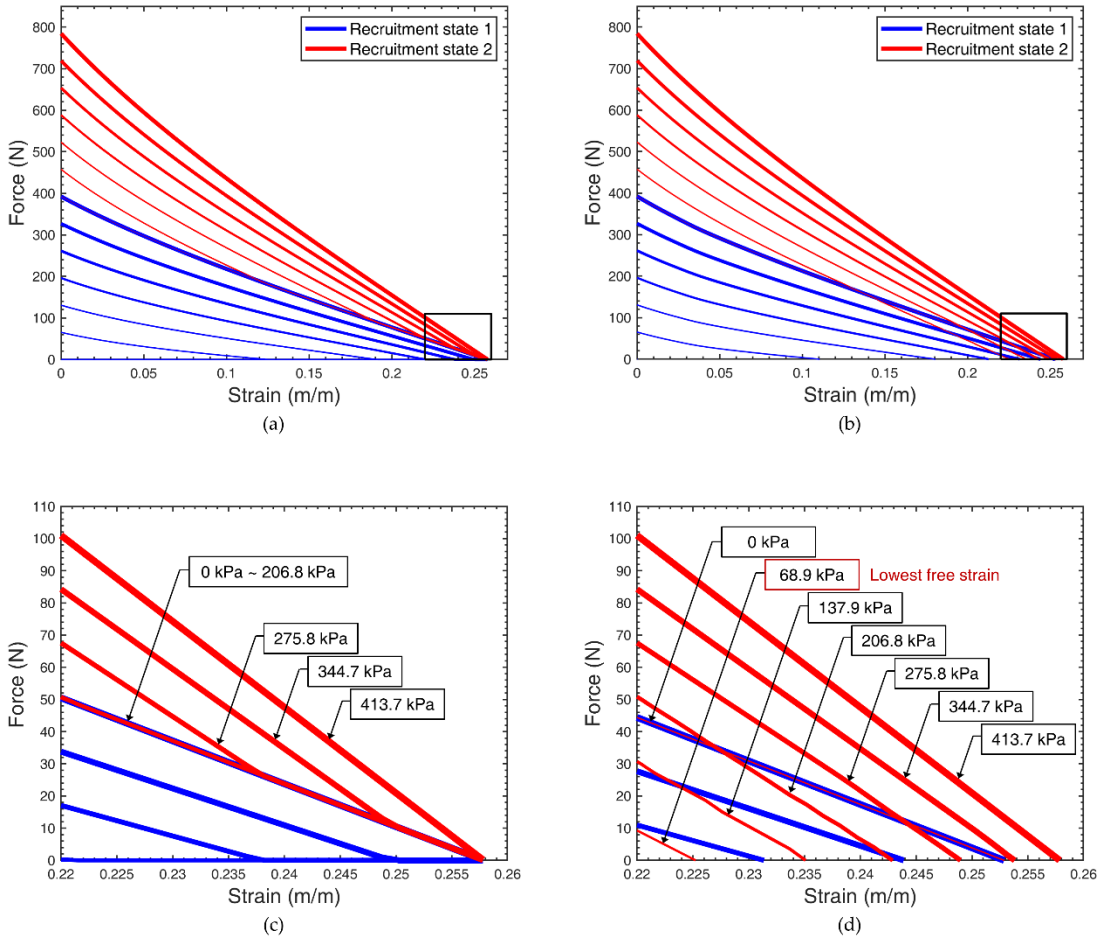

Figure 2.9: Force-strain space of a variable recruitment bundle with two MUs of equivalent cross-sectional area with (a) resistive forces neglected, and (b) resistive forces considered. (c) and (d) show zoomed-in views of the force-strain space near maximum strain with resistive forces neglected and included, respectively. Increasing pressure values are represented by increasing thickness of lines. In recruitment state 2 (red lines), the pressure applied to MU 1 is constant at 413.7 kPa while the pressure applied to MU 2 is indicated in (c) and (d) to show the progression from inactive to fully active.

forces are considered, the negative forces due to resistive effects cause the forces in recruitment state 2 to actually fall below that of recruitment state 1 for certain strains – therefore producing a region of overlap between the domains of each recruitment state. Within this overlapping region,

the bundle can output the same force and strain by operating in either recruitment state. In fact, as recruitment state 2 is activated and the pressure in MU 2 is increased, the isobaric force curve of recruitment state 2 recedes back into the force-strain space of recruitment state 1 as shown in Figure 2.9 (d). The effect of this phenomenon is discussed in further detail in Section 2.6.

2.4.2 Efficiency analysis for isobaric and isotonic contraction

One of the advantages of variable recruitment lies in its increased overall efficiency. Therefore, it is worth exploring the efficiencies of variable recruitment bundles when resistive forces are considered. By choosing a recruitment state that minimizes the energy input while meeting the force requirements, variable recruitment has the potential to increase overall efficiency when compared to a single equivalent motor unit (SEMU). The efficiency of an actuation reaching a given point in the force-strain space from zero strain is the ratio between mechanical work output and fluid energy input where the expression for mechanical work output is given as:

$$W_{mech,out} = \int_0^{\varepsilon L_0} F_{bundle} dx. \tag{2.28}$$

where F_{bundle} is the sum of all the forces generated by individual FAMs calculated by the proposed model, including the negative forces caused by resistive effects. The fluid energy input is defined as:

$$E_{fluid,in} = P_s \Delta V. \tag{2.29}$$

where P_s is the source pressure applied to the valve before losses due to throttling occur. The change in volume to reach a specific strain is calculated by subtracting the fluid volume at that strain value from the initial fluid volume. The fluid volume at a specific strain value is calculated

by solving for inner radius r_{inner} as a function of strain by assuming the bladder material is incompressible. Finally, the expression for efficiency is as follows:

$$\eta = \frac{W_{mech,out}}{E_{fluid,in}}. \tag{2.30}$$

To highlight the system efficiency over the entire force-strain space, two simple cases of quasistatic contraction are considered: isobaric contraction and isotonic contraction. During isobaric contraction, the pressure supplied to the FAM is kept constant while it contracts with varying force. For isotonic contraction, the load is kept constant while the FAM contracts under varying pressure. This is equivalent to moving horizontally through the force-strain space. For each point in the force-strain space, the efficiency for a FAM to move from free length to the strain at the specific point is calculated. The resulting isobaric and isotonic efficiencies for a bundle with two recruitment states are plotted in Figure 2.10(a) and (b). As discussed in Section 2.4.2, an overlapping region exists for an actuator bundle when resistive forces are considered. The efficiency plots in Figure 2.10show only the higher efficiency value within that region.

To study the potential detrimental impact of resistive forces on the overall efficiency of a variable recruitment bundle, the average efficiencies with resistive effects considered and neglected are compared in Figure 2.10 (c) and (d). Prior literature using simpler models that neglect resistive forces predicted that a variable recruitment bundle would show increased in efficiency compared to a SEMU with identical total cross-sectional area [9], [22]. As the number of MUs (and therefore recruitment states) is increased, the efficiency continues to increase, but at a decreasing rate. This trend still holds when resistive forces are considered, producing only a minor decrease in efficiency as shown in Figure 2.10 (c) and (d). As its name suggests, resistive forces act against the tensile force output of active MUs and lower the mechanical work output. However, if the number of recruitment states is increased while keeping the overall bundle cross-sectional

area constant, the slenderness ratio of each MU, defined as L_0/r_0, increases. As a result, the resistive force of each MU decreases, along with the impact it has on the overall efficiency of a bundle. Consider a comparison between a bundle with two MUs (as simulated in this study) to a bundle with five MUs with the same overall bundle cross-sectional area. Assume each bundle is operating in its first recruitment state. For the two-MU bundle, the resistive forces generated by the *single* inactive MU are greater than the resistive forces generated by the *four* inactive MUs in the bundle with five MUs. This is because to keep the cross-sectional area of both bundles the same, the bundle with five MUs must contain FAMs that are much more slender. The resistive force model in this paper predicts that resistive forces decrease with slenderness ratio, which is why we see very little decrease in efficiency, even as the number of MUs within a bundle is increased. Although not within the context of a variable recruitment bundle, Suzumori et al. investigated the mechanics of a bundle of multiple thin McKibben actuators, showing a decrease in bending rigidity of the overall bundle compared to a single large diameter FAM [40]. Therefore, while resistive forces affect the overall force-strain space, which has implications on the control and switching of recruitment states (to be discussed further in the following sections), their overall detriment to the efficiency of the bundle is negligible.

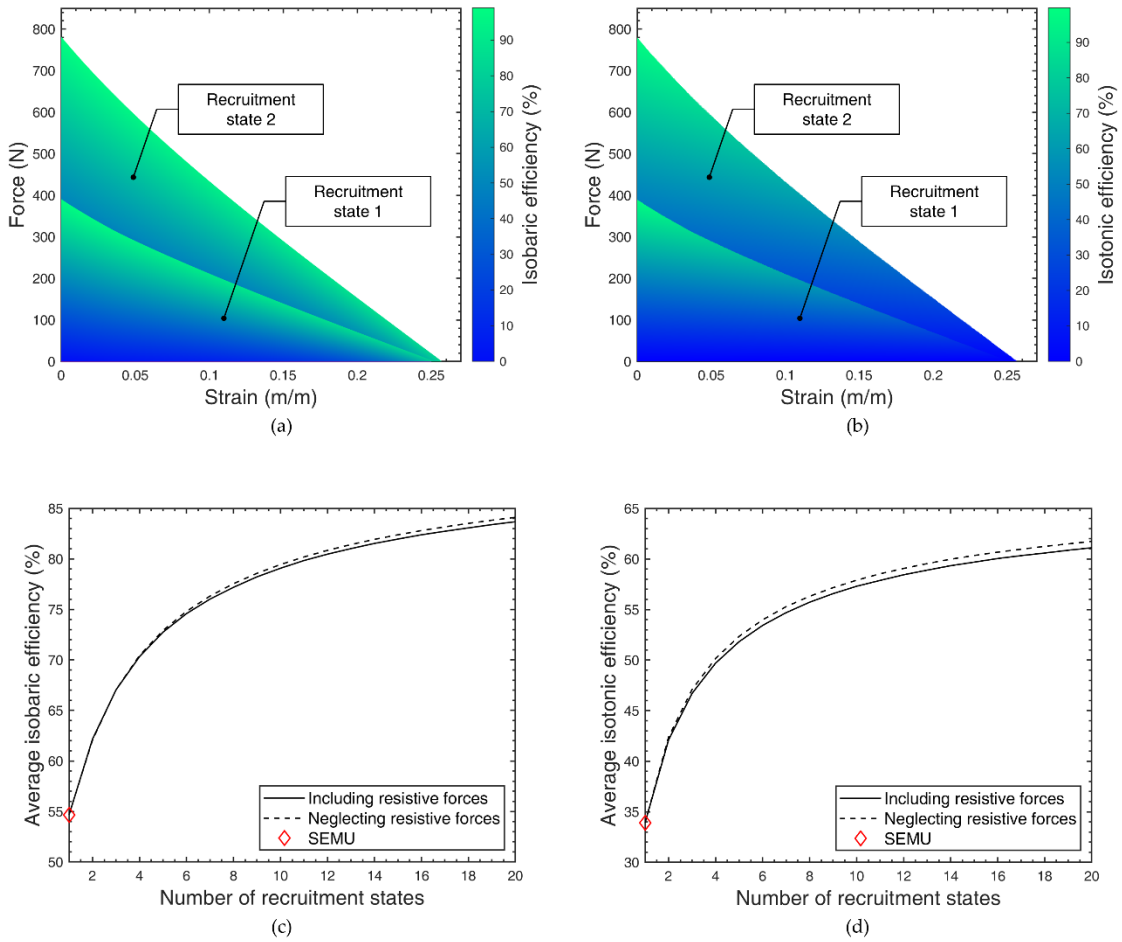

Figure 2.10: The efficiency of the bundle to arrive at a point in the force-strain space for (a) isobaric and (b) isotonic contractions. For isobaric contraction, the bundle is operated along the constant pressure curves; thus, the force varies while contracting. For isotonic contraction, the load is held constant while the bundle contracts, thus moving horizontally within the force-strain space by varying pressure. The average isotonic and isobaric efficiencies are plotted versus number of recruitment states and shown in (c) and (d), respectively.

2.5 Improving the model through empirical parameter tuning

While the model derived above provides a predictive and qualitatively reasonable analysis for understanding the implications of resistive forces on variable recruitment bundles, the model can be empirically corrected to improve quantitative agreement with experimental FAM characterization data. Such semi-empirical modeling has been shown to useful for model-based feedforward control of artificial muscles [41], and in simulation tools for understanding the implications of different recruitment strategies [30] or hydraulic system topologies [13] on FAM actuation systems. Therefore, to further improve the model to match the force from experiments, a method of force correction was developed. There are models in the literature that account for advanced effects such as the tapering effect at the ends of the FAM and the hyperelasticity of the bladder on the tensile force generation of the FAM [14]–[17]. However, it is often the case the blocked force and free strain is overpredicted even when calculated with these advanced models due to uncertainty in the material properties or imperfections in the components used to build the bladder. Tondu and Lopez use a tuning parameter that can either be a constant or a function of pressure to modify the ideal force model shown in (2.3**)** to account for the pressure-dependent free strain [14]. Building upon this method, Meller et al. use an additional parameter that is acquired from experiment data to correct for the discrepancy in blocked force [31]. These methods are used to modify the ideal force model, which does not consider forces due to the bladder. Similar to the method proposed by Meller, we employ two tuning parameters, based on the blocked force and free strain information from experimental data, to modify both the mesh force (ideal force) and bladder force in the tensile region. After these two parameters are used to correct for the tensile region in the piecewise model, additional parameters for the resistive forces are optimized using empirical data.

2.5.1 Tensile Force Correction

The modified model for forces up to free strain is expressed as:

$$F_{mod} = C_2(F_{total} - C_1), \tag{2.31}$$

$$F_{mesh,mod} = C_2 F_{mesh}, \tag{2.32}$$

and

$$F_{bladder,mod} = F_{mod} - F_{mesh,mod}, \tag{2.33}$$

where the forces prior to modification are equivalent to those from (2.4) and the strain tuning parameter C_1 is found by evaluating the theoretical force at the free strain obtained from experiment, known as $\varepsilon_{free,\text{exp}}$, in the equation:

$$C_1(P) = F|_{\varepsilon_{free,exp}} \tag{2.34}$$

and the force tuning parameter C_2 is expressed in terms of the experimental block force $F_{blocked,\text{exp}}$, theoretical block force $F_{blocked}$, and C_1 as:

$$C_2(P) = \frac{F_{blocked,exp}}{F_{blocked} - C_1} \tag{2.35}$$

Both tuning parameters are functions of pressure that are specific to an actuator. Note that the unit of C_1 is in Newtons and C_2 is unitless. Both factors are greater than zero and have no upper bound. The parameters are obtained by measuring the free strain and blocked force as functions of pressure, much like the procedure followed by Meller et al. [31]. As shown in [31], the function for free strain typically follows a low-order polynomial and blocked force typically increases linearly with pressure with a positive force x-intercept.

2.5.2 Resistive Force Correction

Once the forces before free strain have been corrected based on empirical data, several parameters of the proposed model for the post-buckling and post-collapse regions have been optimized based on experimental data. A least-squares fit analysis is conducted to determine correction factors for the following parameters.

1. Young's Modulus, E
2. Collapse moment, $M_{collapse}$
3. Transition constant, β
4. Torsional spring stiffness, k_r

The resistive force model does not consider the hyperelasticity of the bladder as the FAM is compressed. The bladder used for the experiments was an off-the-shelf component without any specification of material properties. To account for such uncertainties, a correction factor was used to optimize the Young's modulus and the optimized value was used across all pressures.

Furthermore, a correction factor was optimized to modify the collapse moment. Wielsgosz et al. used a factor of 0.25π to modify the collapse moment as experimental validation showed a tendency to overpredict the value [42]. Stephans et al. investigated the correlation of collapse moment to the slenderness ratio of the pressurized cylinder. For cylinders with low slenderness ratios, the collapse moment tends to be closer to the 'classical' formulation, whereas for that of higher slenderness ratios, the collapse moment reaches the load formulated by Brazier [43]. A similar correction factor is used to modify the collapse moment given in (2.17).

The third tuning parameter is the transition rate constant β given in (2.26), used in characterizing the transition from post-buckling to post-collapse regions. Lastly, a correction factor

is used to optimize the torsional spring stiffness k_r used in (2.20) to model the post-collapse 'hinge' at the middle of the bladder.

2.5.3 Experiments to generate correction factors

Experiments were performed on an in-house built linear dynamometer developed by Chipka et al. [23] as shown in Figure 2.11. The air pressure applied to the FAMs was controlled in closed-loop by pneumatic servo valves (FESTO MPYE-5-M5-010-B), while the drive cylinder is hydraulically powered and controlled by a MOOG Series G761-3005B servo valve. A Hydraulic power unit (HPU, Haldex GC9500) provided power to a drive cylinder that was used to control the contraction of the FAM. The FAM was constrained between two plates with a load cell (Transducer Techniques SSM-1K) to measure the FAM axial force. Prior to attaching the FAM to both plates, it was pressurized at the maximum test pressure and allowed to contract freely, and its maximum strain was measured. This value was used to determine the stroke of the drive cylinder. The FAM was then attached to both plates separated by the amount of actuator free length which is determined by adjusting the starting position of one of the plates until the axial force measured was zero. From this starting position, the FAM was pressurized to the maximum testing pressure and repeatedly contracted several times prior to collecting force data to account for Mullins effect [44]. Force data was measured for pressures from 0 kPa to 413.7 kPa (60 psi) in 34.5 kPa (5 psi) intervals. The position of the drive cylinder was controlled at a sufficiently slow rate to remove any dynamic effects and yield a quasi-static measurement. The force for two FAMs of different slenderness ratios were measured to demonstrate its correlation to resistive force magnitude and support the analytical efficiency hypothesis stated in Section 2.4.2. An initial radius of 0.0635 m,

initial braid angle of 33 degrees was used for both FAMs with an initial length of 0.102 m and 0.127 m, corresponding to slenderness ratios of 8 and 10, respectively.

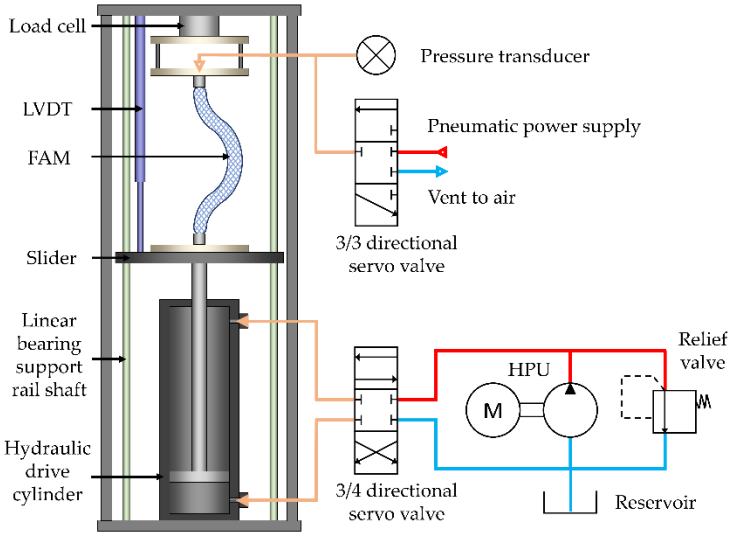

Figure 2.11: Experiment setup using the LHD developed by Chipka et al. [23]**. A hydraulic power supply is used to actuate the drive cylinder. The FAM is activated using a pneumatic power supply while the force and contraction is measured using a load cell and LVDT, respectively.**

2.5.4 Results from Empirical Parameter Tuning

The correction factors, which are a result of least-squares optimization, are summarized in Table 2.1. The correction factors for the Young's modulus, collapse moment, and transition constant were the same for all pressures. The correction factor for the torsional spring constant in the post-collapse region showed a dependence on pressure since the torsional spring constant calculation proposed does not consider the increase in bending rigidity due to increased pressure.

Table 2.1: Resulting correction factors from empirical parameter tuning

FAM No.	Slenderness Ratio, L_0/r_0	Correction Factors			Transition Constant, β
		Young's Modulus	Collapse Moment	Torsional Spring Constant	
1	8	1.25	1.1	$0.87P + 1.25$	100
2	10	0.95	0.75	$0.92P + 0.83$	100

The measured force data from experiments are shown in Figure 2.12 along with the simulated force curves from the empirically corrected model. The force curves from 0 kPa to 137.9 kPa in 34.5 kPa intervals are shown as resistive force bear more significance in low pressure ranges. In the resistive force regime, a good agreement is observed between the experiments and the corrected model. Free strains for constant pressure force curves past 137.9 kPa occur closer to the maximum free strain and do not show the collapse of the bladder. In the tensile force regime, the model blocked force and free strain obviously match those of the experiment as a result of the empirical tuning described in Section 2.5.2. Although the cross-sectional area is the same for both FAMs, a difference in blocked force is observed due to a difference in bladder force at zero strain. A significant difference in resistive force magnitude is observed between the two FAMs with different slenderness ratios. As predicted in the model, the FAM with a lower slenderness ratio exhibited a larger magnitude of resistive force. This supports the conclusion that efficiency does not decrease as the number of MUs increases due to slenderness ratio effects, as detailed in Section 2.4.2.

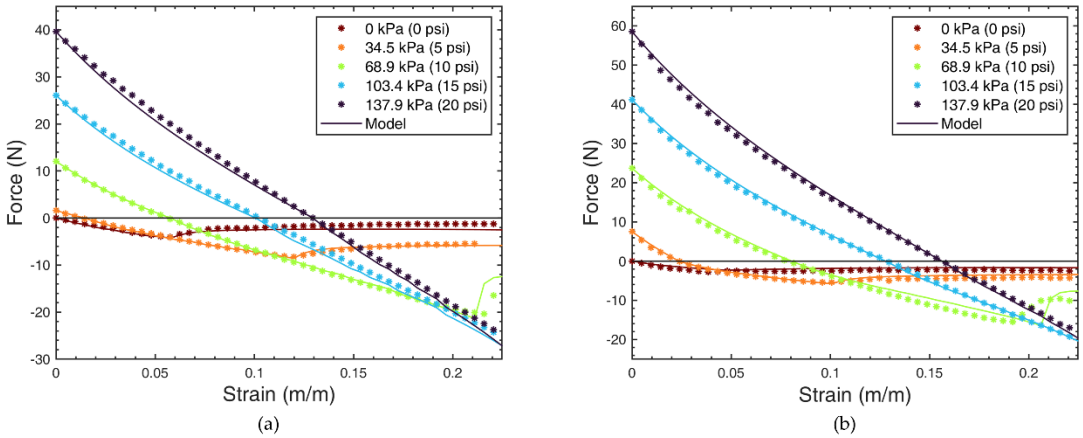

Figure 2.12: Result of empirical-based tuning of parameters and comparison to experimental data for a FAM with (a) slenderness ratio of 8 and (b) slenderness ratio of 10. Forces for 0 kPa, 34.5 kPa, 68.9 kPa, 103.4 kPa, and 137.9 kPa are measured and used to optimize the parameters specified in Table 2.1. The Young's modulus, collapse moment, and transition rate constant are independent of pressure, while the torsional spring stiffness varies with pressure.

2.6 Bundle Free Strain Gradient Reversal

The force-strain plots shown in Section 2.4 of this paper illustrate an interesting phenomenon that occurs within a bundle when resistive forces are considered. When MU 1 reaches source pressure, MU 2 is activated and the bundle transitions between recruitment states 1 and 2. Once MU 2 is activated, the overall bundle free strain actually begins decreasing because resistive forces are stronger in low-pressure FAMs than inactive FAMs. As MU 2 pressure is further increased, the free strain continues to decrease, until eventually, the kinematic forces generated by the FAM in MU 2 overcome the resistive forces, and free strain begins to increase. We call this phenomenon *free strain gradient reversal*, and the point at which the free strain ceases to decrease due to the presence of MU 2 is called the *free strain gradient reversal point*. This idea can be more clearly illustrated in Figure 2.13, which is a plot of overall bundle free strain vs. MU 2 pressure

for different models: the ideal model, the Klute-Hannaford model [18], the corrected Klute-Hannaford model neglecting resistive forces discussed in Section 2.5.1, and the corrected Klute-Hannaford model including resistive forces, as well as a plot for a 2-MU experiment. The experiment results shown in Figure 2.13 are measurements obtained from the FAM with a slenderness ratio of 10 in Section 2.5.4.

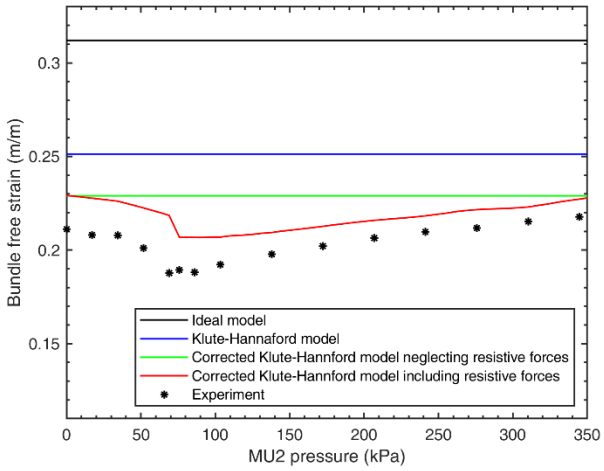

Figure 2.13: Free strain of actuator bundle versus pressure applied to MU 2 shown for the ideal model, the Klute-Hannaford model [18]**, the corrected Klute-Hannaford model neglecting resistive force, the Klute-Hannaford model including resistive forces, and experimental data. The pressure of MU1 is kept constant at 344.7 kPa. The free strain initially decreases in response to increased pressure in the second recruitment state.**

From Figure 2.13, we can see that previous models did not capture the gradient reversal phenomenon that exists due to the presence of resistive forces, but the model presented in this paper demonstrates this behavior. Every data point from the experiments falls within 10 percent of the predicted values, with the exception of one, which falls within 15 percent. The differences between the model and the experiment are believed to be largely due to fabrication uncertainties in the FAMs, which were constructed to be identical, but may have had slightly

different free lengths or initial braid angles. Such fabrication discrepancies result in slightly different blocked force and free strain for the two FAMs, leading to a different bundle blocked force and free strain than that predicted by the model. We can investigate this gradient reversal further by considering the purely analytical case of an actuator bundle consisting of 5 FAMs. We compare two different bundle configurations: one bundle with 2 MUs (MU1 having 1 FAM and MU2 having 4 FAMs) and another bundle with 5 MUs (1 FAM per MU). The comparison plot of these two bundle configurations is shown in Figure 2.14. The experimental results for a FAM with slenderness ratio 10 from Section 2.5.4 are used to generate these plots. Similar to the 2-MU bundle in Figure 2.13, the pressure of MU1 is kept at 344.7 kPa.

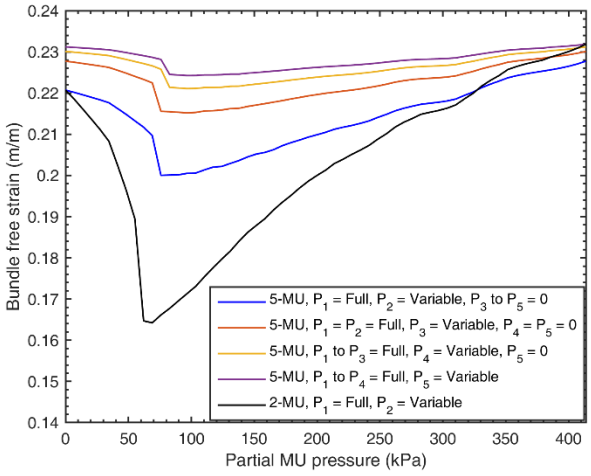

Figure 2.14: Model comparison of bundle free strain vs. the MU pressure while transitioning between recruitment states 1 and 2 for a bundle consisting of 5 FAMs. P_n denotes the pressure applied to MU n. The black line represents a bundle with two MUs, one containing a single FAM and the other containing four FAMs. The colored lines represent the different recruitment states of a five-FAM bundle that consists of 5 MUs (i.e., one FAM per MU).

The results from Figure 2.14 show that for the 2-MU bundle configuration, the reduction in free strain due to the resistive forces during the transition from recruitment state 1 to recruitment state 2 is much more pronounced than the reduction in free strain associated with transitioning from recruitment states 1 through 5 for the 5-MU bundle. This result is particularly significant when considering bundle design, because we can change the characteristics of a bundle without changing the number of FAMs in the bundle simply by changing the distribution of MUs within the bundle. In future work, we will investigate optimal methods to distribute these MUs to accomplish specific actuation tasks.

2.7 Conclusions

In this paper, the reaction forces of FAMs compressed axially past free strain, defined in this paper as resistive forces, have been modeled. Furthermore, the effect of resistive forces on the overall performance of a variable recruitment bundle was brought to attention. The resistive force of a FAM is divided into two regions: post-buckling and post-collapse. In the post-buckling region, the additional force required to bend the bladder into the post-buckling shape was derived using a virtual work balance. To account for geometric imperfections and axial deformation of the bladder, an equivalent spring system was proposed to refine the force in the post-buckling region. The termination of the post-buckling region is determined by when the internal moment generated in the bladder exceeds the collapse moment. After the bladder collapses, a similar approach is taken for the post-collapse region, in which a clamped-hinged-clamped mode shape is used to calculate the force required to bend the bladder into that shape. A first-order response is used in the post-collapse region to approximately capture the transition from post-buckling to post-collapse behavior.

To further improve the model to better match experimental results, a technique that uses two pressure-dependent tuning parameters to correct for the discrepancy in blocked force and free strain was proposed for forces up to free strain. Unlike other methods in the literature, the proposed method can modify the mesh and bladder force components. After tuning the parameters for forces up to free strain, several parameters of the proposed resistive force model are optimized using empirical data. The Young's modulus, collapse moment, and transition rate constant were determined to be constant for a given FAM geometry and independent of pressure. Only the torsional spring stiffness used in the post-collapse model was shown to be pressure-dependent. As a result, a viable semi-empirical physics-based model was validated with experimental results.

The force-strain space for a bundle with two recruitment was simulated to show an overlapping region between recruitment state 1 and 2, which was not observed until resistive forces were considered. An efficiency comparison between bundles with and without resistive forces showed a negligible amount of difference in both isobaric and isotonic efficiency, indicating that the presence of resistive forces in FAM bundles do not preclude variable recruitment from be used as energy-saving strategy. As the number of recruitment states increased, the slenderness ratio of FAMs increased, resulting in a decrease in resistive force magnitude. The addition of the resistive force exerted by the inactive/low-pressure MUs to the force output of active MUs results in a strain-dependent change in performance when advancing to a higher recruitment state. This free strain gradient reversal is significant when considering the problem of how to optimize bundle design how to develop control criteria for switching in between recruitment states, which is to be investigated in future work.

The post-buckling load-deflection behavior of an inflatable tube under axial load is a topic of extensive research and not a simple problem when applied to FAMs. However, a relatively

simple solution can be derived using the assumptions in this paper that will allow us to better evaluate bundle performance and design more effective variable recruitment controllers.

CHAPTER 3

Electrohydraulic system analysis of variable recruitment fluidic artificial muscle bundles with interaction effects

This study investigates the system-level performance of variable recruitment (VR) fluidic artificial muscle (FAM) actuator bundles using a model that incorporates FAM interaction effects. Previous models that characterize FAM force-strain behavior focus on output in the tensile region. While such models are effective in single-FAM actuator applications, a VR bundle combines multiple FAMs to act as one actuator in which the FAMs are sequentially recruited to increase overall efficiency. This approach is similar to how muscle fibers are recruited in mammalian muscle tissues. In a VR bundle, inactive/low-pressure FAMs are compressed beyond their free strains, exerting resistive forces opposing that of active FAMs. A recent model that is able to capture this behavior is used to simulate sinusoidal contraction of a VR bundle with a hanging mass load. The implications of inter-FAM effects on the force-strain space of a VR bundle are discussed and a method of recruitment state transition for a VR bundle to track a sinusoid is proposed. The dynamics of the electrohydraulic subsystems such as the motor/pump and valves required to power the VR bundle are presented and used to evaluate its system efficiency and bandwidth limits. Three different electrohydraulic configurations are considered: 1) continuous motor operation with constant pump displacement, 2) intermittent motor operation with constant pump displacement and 3) continuous motor operation with variable pump displacement. The simulation results show that a VR bundle is able to operate at greater bandwidths compared to a single equivalent cross-section area motor unit (SEMU). In addition to increased bandwidth limit, a VR bundle shows increased system efficiencies when using variable pump displacement.

3.1 Introduction

McKibben actuators, often referred to as fluidic artificial muscles (FAMs) are inherently compliant actuators known for their high power-to-weight ratio [1], [14]. These actuators were created by Joseph McKibben in 1958, motivated to aid his daughter whose hands had been paralyzed due to polio. As its moniker suggests, FAMs were created to mimic the contractile motion of the human muscle, which still motivates researchers today to investigate its application to exoskeletons, orthotics and prosthetics [4], [24], [25]. A FAM consists of a double-helical fiber mesh wrapped around an inner elastic bladder. While one end of the bladder is blocked off, the other end is connected to a fitting through which pressure is applied. The FAM is activated by applying pressure, either pneumatically or hydraulically, causing the mesh to constrain the bladder to expand radially and contract axially.

Although originally intended as a contractile actuator, modifications can be made to FAMs to produce other modes of actuation. Increasing the angle at which the mesh fibers are helically wrapped around the elastic bladder can alter the FAM to produce extensile motion [2]. Adding inelastic layers to the mesh allows the actuator to bend or twist [3], [45]. Other researchers have focused on the arrangement of multiple FAMs in different configurations. Conventional use of FAMs considers them as individual single-acting actuators with a single FAM applying unidirectional force to a joint or an antagonistic pair of FAMs producing bidirectional actuation. Others, however, have taken inspiration from parallel or pennate human muscle tissue topologies to view each FAM as a subcomponent of a single multi-unit actuator, much like how each natural muscle organ consists of multiple motor units (MUs) that act together to produce unidirectional force and displacement on a joint [7]. Kurumaya et al. developed a multifilament muscle actuator by bundling multiple thin FAMs to actuate a musculoskeletal robot [46]. Bryant et al. created a

FAM bundle using multiple FAMs in parallel with added variable recruitment (VR) functionality [9]. The FAMs within the bundle can be grouped into independently-activated units of actuation, which are equivalent to the MUs in biological muscle tissue. According to Henneman's size principle, MUs are sequentially recruited from smallest to largest in size and the subsequent MU is only activated when the previous MU has reached its peak force output [10]. Inspired by this recruitment scheme, the MUs within the FAM bundle are sequentially activated to meet the load demand. Compared to a single larger FAM with equal total cross-sectional area, this VR bundle can increase the average efficiency over the force-strain working space by reducing the energy losses due to pressure throttling during submaximal pressure actuation [9]. The performance increase of VR bundles has been experimentally validated for both pneumatic and hydraulic power sources [9], [30]. Different schemes of MU activation have also been investigated. In 'batch' recruitment, a single pressure control valve and multiple on-off valves are used to control the pressure of MUs, while in 'orderly' recruitment, the pressure of each MU is controlled separately and activated sequentially. This scheme can either be implemented by using a pressure valve for each MU, or by using a single orderly recruitment valve (ORV), which decreases fluid circuit complexity by using fewer valves [47]. In addition to such 'active' recruitment schemes, the bladder elastic properties can be separately tailored for each MU to passively recruit them in a desired sequence [48]. Real-time control schemes for variable recruitment have been developed and tested [30], [41].

Previous studies have mainly focused on the downstream actuator efficiency comparing the mechanical work output to the fluid energy input into the pressure control valve [9], [10]. Later studies have modeled the entire electrohydraulic system including the motor, pump and accumulator required to supply hydraulic power [13], [27]. Such studies compare the mechanical

work output of the actuator to the electrical energy input to the motor during a set period of time, providing a more holistic perspective of the performance when VR is applied to a robotic system. Chapman et al. showed that a FAM operating at its peak efficiency does not necessarily guarantee the peak efficiency of the overall system by building and modeling a quadrupedal wall-climbing robot and its fully-coupled electrohydraulic system [27]. A subsequent study compared system-level performance metrics such as overall efficiency and bandwidth of a FAM with equal cross-sectional area to that of a VR bundle during continuous and intermittent pump electrohydraulic configurations [13]. In these studies, a modified version of the ideal FAM model that takes into account the nonlinear properties of the inner elastic bladder were used to simulate the overall bundle force and strain [19], [49].

Recently, a FAM model that better captures the interaction effects between FAMs within a bundle has been proposed [21]. Due to the sequential manner in which bundle MUs are recruited, inactive or partially active FAMs within a bundle experience compression beyond their free strains, exerting ‘resistive forces’ acting against the overall force output of the bundle. In the physical system, the inactive/partially active FAMs tend to buckle outward, increasing the spatial envelope of the bundle. Several mitigation strategies have been implemented to prevent the FAMs from buckling. Embedding the bundle in silicone proved effective in inhibiting FAMs from buckling but decreased strain output [9]. Using tendons in series with the FAMs prevented buckling and thus increased overall bundle volumetric energy density while increasing efficiency in some portions of the bundle force-strain space at the expense of others [50]. Although such mitigation strategies can prevent motor unit buckling, they all require additional components and material as compared to a plain FAM bundle and come with tradeoffs in maximum bundle contraction and efficiency. This study first aims to address the challenges posed by bundle FAM

interaction effects without taking such measures. Using a FAM model that accounts for resistive effects gives insight into the overall force-strain space of a VR bundle that is not evident when using simpler models. The purpose of this study is to investigate the implications of these inter-FAM effects on the recruitment control strategy required to track a desired trajectory and to evaluate the full electrohydraulic system efficiency of a variable recruitment FAM bundle in the presence of inter-FAM effects with several pump operation architectures. The specific contributions of this paper are to (1) demonstrate the effects resistive force and electrohydraulic system dynamics on recruitment state transition, (2) integrate pressure control valve dynamics and the effects of a variable displacement pump into a fully-coupled system model and (3) evaluate the system efficiency and bandwidth of a VR bundle actuator with inter-FAM effects and under various electrohydraulic configurations.

The subsequent sections of the paper are organized in the following way. In Section 3.2, the FAM model used in this study and the electrohydraulic subsystem models are presented. The implications of resistive forces and electrohydraulic system dynamics during recruitment state transition are discussed in Section 3.3. In Section 3.4, the metrics for which the system performance is evaluated in presented, followed by the three different simulation electrohydraulic configurations. The simulation results from the different configurations are presented and compared. The conclusions of the paper are presented in the final section.

3.2 Modeling

3.2.1 Fluidic artificial muscle (FAM) modeling with resistive forces

Modeling of FAM behavior has evolved over the years. Chou and Hannaford used a virtual work balance approach to model a FAM's axial contractile behavior imposed by the kinematic

constraint of the double helix braided mesh [19]. This model is often referred to as the ideal FAM force-strain model as it assumes the FAM as a perfect cylinder throughout the entirety of its contractile motion and that forces exhibited by the elasticity of the bladder are negligible. The ideal FAM model is expressed as:

$$F_{ideal} = F_{mesh} = \pi r_0^2 P \left(\frac{1}{tan^2\alpha_0}(\varepsilon - 1)^2 - \frac{1}{sin^2\alpha_0}\right), \quad (3.1)$$

where P is the pressure applied, r_0 is the initial radius of the braid, α_0 is the initial braid angle, and ε is the strain of the FAM. researchers have further developed this model to include the tapered geometry of the bladder during contraction, wall thickness of the bladder, and bladder elasticity [14], [17], [49]. Rather than using a virtual work balance approach, some FAM models use a force balance approach to model a FAM's force output [15], [16].

Among the FAM models in the literature, this study uses the model proposed by Kim et al. [21], which expands the model by Klute and Hannaford [18] to strains past the free strain condition to include forces generated when the FAM is compressed. In the tensile region, the resistive force model is identical to the model by Klute and Hannaford, expressed as:

$$F_{total} = F_{mesh} + F_{bladder} = P\frac{dV}{dL} - V_b\frac{dW}{dL}, \quad (3.2)$$

where $F_{bladder}$ is the force contribution due to the hyperelasticity of the bladder and V_b is the volume of the incompressible bladder. The Mooney-Rivlin strain energy function, W, is used to characterize the energy stored and the principle of virtual work is applied to model the elastic bladder force. As the FAM is compressed past its free strain, it initially exhibits buckling behavior for which the force is expressed as:

$$F_{total} = F'_{mesh} + F_{bladder}(\varepsilon_{free}) + F_b, \quad (3.3)$$

where F'_{mesh} is the braided mesh force using the arc length of the FAM in its buckled shape and ε_{free} is the free strain. F_b is the bladder force in the axial direction required for static equilibrium of the bladder to maintain its buckled shape, calculated using the total potential energy stored. As the FAM is compressed further, the internal moment generated along the FAM reaches a critical value, at which the FAM collapses and folds upon itself. The forces after the FAM have collapsed is expressed as:

$$F_{total} = F_c + (F_b - F_c)^{-\beta(\varepsilon - \varepsilon_c)} \tag{3.4}$$

where F_c is the axial force of the bladder in its collapsed shape and ε_c is the strain at collapse. The transition from buckled to collapsed regions is characterized by β which is tuned based on parameter optimization. The Kim et al. resistive force FAM model captures the behaviors of and predicts the forces exerted by the FAM in both tensile and compressive regimes. For applications in which FAMs are used as stand-alone actuators, the axial force behavior past free strain may not be of interest. However, in predicting the overall force output of a VR FAM bundle, these negative forces must be considered. Depending on the recruitment state, FAMs within a bundle may be in a combination of fully active (maximally pressurized), partially active (submaximally pressurized), or inactive (unpressurized) states. In a situation when fully active FAMs and inactive/partially active FAMs coexist, the latter FAMs are compressed beyond their free strain exerting a force opposing the force output of the active FAMs. For this reason, the negative force is also referred to as the *resistive force*. Figure 3.1 illustrates a bundle with two FAMs, at an instance when one FAM is fully active (right) while the other is only partially active (left). The fully active FAM generates force while the partially active FAM contributes resistive force.

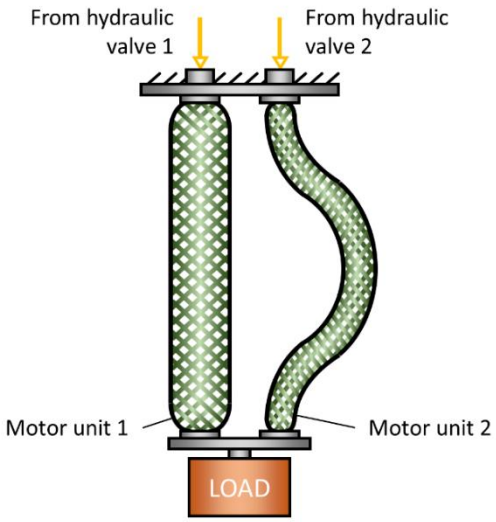

Figure 3.1: FAM bundle consisting of two FAMs. The fully active FAM (left) outputs contractile force while the partially active FAM (right) contributes resistive force that opposes that of the fully active FAM.

Figure 3.2 shows the isobaric force-strain curve of a FAM including the resistive forces. At the blocked force condition, the FAM force is at its maximum. As strain increases, the force output decreases, eventually reaching zero at its free strain condition according to (3.2). As strain is increased past free strain and the FAM begins to buckle outward, the FAM exerts a resistive force shown by the negative region. Further compression causes the FAM to collapse, which is when the magnitude of resistive force is largest. Immediately following collapse, the magnitude of resistive force decreases and eventually approaches the axial force of the collapsed force F_c from (3.4).

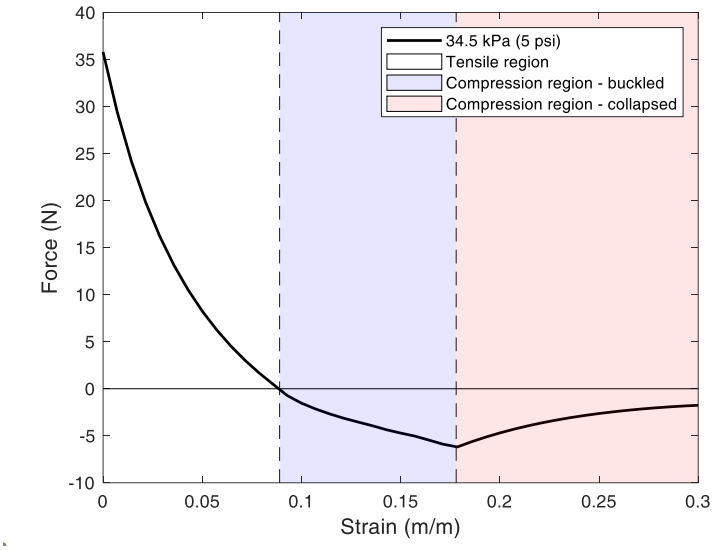

Figure 3.2: Force versus strain curve for a fluidic artificial muscle (FAM) including the compressive region. FAMs within a variable recruitment (VR) bundle experience compression past its free strain. The FAM begins to buckle outward until the internal moment generated in the bladder causes the bladder to collapse [21]**. The dimensions for the FAM used to generate this plot are listed in Table 3.1.**

Figure 3.3 illustrates the effects of resistive forces on the force-strain space of a VR bundle with two recruitment states. The bundle consists of two FAMs of equal dimensions, each representing one MU. The isobaric force-strain curves at various pressures are plotted as predicted by the model with resistive forces included and compared to the model prediction with resistive forces neglected. In recruitment state 1 (RS1), only one MU is either partially or fully activated. In recruitment state 2 (RS2), the first MU is fully activated while the second MU is partially or fully activated. The main difference between the force-strain space of the VR bundle when resistive forces are included and when they are neglected is shown by an overlapping region between RS1 and RS2. When resistive effects are neglected, the force-strain space of RS1 and RS2

do not overlap. During the transition from RS1 to RS2 when the first MU has reached its maximum pressure, any additional pressure supplied to the second MU either maintains or increases the force output of the bundle. However, in a more realistic case when resistive forces are considered, an initial increase in the pressure of MU2 results in a decrease in bundle force output. Due to the negative forces exerted by the second MU, which is in compression, the force generated in RS2 at low MU2 pressures falls below that generated in RS1. A detailed discussion of this overlapping region has been presented in the paper by Kim et al. [21]. The present study presents the implications of the electrohydraulic system dynamics, resistive forces and the resulting overlapping recruitment state region on controlling bundle strain and force to track a desired motion trajectory under VR.

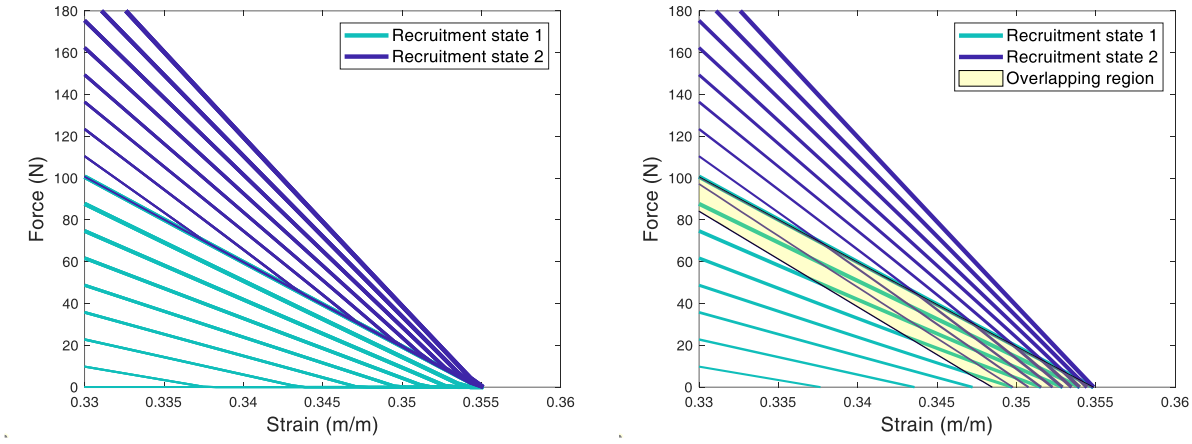

(a) (b)

Figure 3.3: Force-strain space for variable recruitment (VR) bundle with two recruitment states when (a) neglecting resistive forces and (b) including resistive forces. Isobaric force-strain curves are plotted at 68.9 KPa (10 psi) intervals from 0 KPa to 551.6 KPa (80 psi). Pressure magnitude is indicated by line width with thicker lines representing higher pressures. Due to the presence of resistive forces, an overlapping region, shown as the shaded region in (b), exists between recruitment states 1 and 2.

While the mathematical model itself provides qualitative information and shows similar trends to experimental measurements of FAM behavior past free strain, more refined modeling matching is required for model-based control applications. Isobaric force-strain curves for the FAMs used in this study have been measured and compared to the model. Figure 3.4 shows the result of using empirically-based correction factors to improve model matching to actual measurements. The method for model tuning using experimental data is presented in the paper by Kim et al. [21] and the FAM parameters and correction factors used are summarized in Table 3.1.

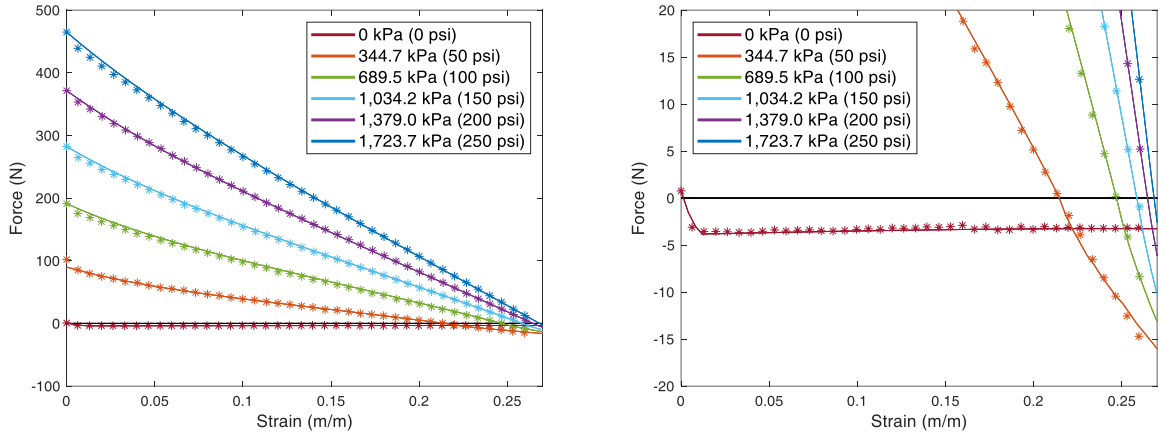

(a) (b)

Figure 3.4: Measured force versus strain of fluidic artificial muscle (FAM) compared to model with empirically-based tuning correction factors for (a) the entire force-strain space and (b) close-up of resistive forces. Model predicted force-strain curves are shown in solid lines and measured values are indicated in markers.

Table 3.1: Fluidic artificial muscle (FAM) parameters and empirical-based tuning correction factors.

FAM dimensions	Initial inner radius (m)	r_0	0.0063
	Initial thickness (m)	t_0	0.0016
	Initial braid angle (°)	α_0	33
	Initial length (m)	L_0	0.2286
Empirically-based tuning correction factors [21]	Young's modulus	-	1.25
	Collapse moment	-	0.8
	Torsional spring constant	-	0.87P + 1.25
	Transition constant	β	100

3.2.2 Electrohydraulic system modeling

3.2.2.1 Hydraulic servo control valve subsystem

The flowrate through the valve orifice is determined by the flow dynamics of the hydraulic servo valve controlling the MU, expressed as:

$$Q_v = c_v d_v sgn(P_{acc} - P_v)\sqrt{|P_{acc} - P_v|}, \tag{3.5}$$

where d_v is the port diameter, P_{acc} is the accumulator pressure and P_v is pressure immediately after the valve. The flow coefficient, c_v, is calculated using the nominal flowrate, Q_N, and nominal pressure drop, Δp_N, across the maximum port diameter, $d_{v,max}$ [51].

$$c_v = \frac{Q_N}{\sqrt{\Delta p_N/2} \cdot d_{v,max}} \tag{3.6}$$

The flowrate into the MU is then determined by the pressure out of the valve and the hose dimensions connecting the valve to the MU according to the Hagen-Poiseuille Law under steady and laminar flow assumptions [52].

$$Q_{MU} = \frac{\pi r_{c,down}^4}{8\eta} \frac{P_v - P_{MU}}{l_{c,down}}, \tag{3.7}$$

r_c and l_c are conduit radius and length downstream of the servo valve, respectively. η is the dynamic viscosity of hydraulic oil [52]. P_{MU} is the pressure applied to a MU. In later sections, the subscript is used to denote the MU number. (i.e. P_{MU1} is the pressure applied to the first MU.) The inflow of fluid into a MU as governed by (3.7) is used to determine its pressure dynamics. The MU force and strain is determined by the pressure as a result of compression of MU internal fluid. The pressure dynamics of the MUs are expressed as below:

$$\frac{dP}{dt} = E' \frac{Q_{MU} - \dot{V}_{MU}}{V_{MU}}, \tag{3.8}$$

where V_{MU} is the MU internal fluid volume and E' is the effective bulk modulus of fluid. The effective bulk modulus is used to capture the effect of entrained air and pressure-dependent characteristics.

$$E' = E_{max}\left[1 - e^{\left(-0.4 - 2\times10^{-7}P\right)}\right] \tag{3.9}$$

The instantaneous accumulator pressure is expressed as:

$$P_{acc} = \frac{P_{acc,0}\left(V_{acc,0} + V_{down} + V_{up}\right)}{\left(V_{acc,0} + V_{down} + V_{up} - V_m + V_p\right)}, \tag{3.10}$$

where $P_{acc,0}$ and $V_{acc,0}$ are the initial pressure and volume of the accumulator, respectively. V_{down} is the amount of fluid volume downstream of the servo valve while V_{up} is the upstream fluid volume. V_m denotes the fluid volume in the FAMs, which is a function of its strain. Lastly, V_p is the amount of fluid volume delivered by the pump/motor.

3.2.2.2 Pump and motor subsystem

A brushless DC motor and hydraulic axial pump subsystem is considered assuming constant voltage operating condition [13]. Given motor parameters and voltage applied, the current rate of change, $\dot{I}$, is expressed as:

$$\dot{I} = \frac{V_{motor} - k_b\dot{\theta} - IR}{L}, \tag{3.11}$$

where V_{motor} is the voltage applied to the motor, k_b is the back electromotive force (EMF) constant, $\dot{\theta}$ is the rotational speed output of the motor, R is the terminal resistance and L is the motor inductance. Based on a first principles analysis of a DC motor operating on constant voltage [53], the rotational acceleration of the motor output shaft, $\ddot{\theta}$, can be expressed as:

$$\ddot{\theta} = \frac{k_e I - B_m\dot{\theta} - \tau_p}{J}, \tag{3.12}$$

where k_e is the motor torque constant, B_m is the frictional damping coefficient and J is the rotor moment of inertia. The motor torque, τ_p, which is equal to the pump impeller torque, is expressed as:

$$\tau_p = \frac{P_{acc}D}{2\pi}, \tag{3.13}$$

where P_{acc} is the accumulator pressure and D is the pump displacement. The motor parameters and operating characteristics were adapted from a 20W Maxon motor (BRx42-40) with a nominal voltage rating of 12 V and are shown in Table 3.2.

Table 3.2: Valve, motor, conduit, and hydraulic oil parameters.

Nominal flowrate (l/m)	Q_N	63
Nominal pressure drop (kPa)	Δp_N	350
Max. port diameter (m)	$d_{v,max}$	0.001
Max. bulk modulus of hydraulic oil (kPa)	E_{max}	1.8×10^6
Motor voltage (V)	V_{motor}	12
Back EMF constant $(V \cdot s/rad)$	k_b	0.028
Terminal resistance (Ω)	R	1.250
Motor inductance (H)	L	0.89×10^{-3}
Motor torque constant (Nm/A)	k_e	0.03
Frictional damping coefficient $(Nm/rad \cdot s)$	B_m	6.3×10^{-4}
Rotor moment of inertia (kgm^2)	J	1.1×10^{-5}
Accumulator initial pressure (kPa)	$P_{acc,0}$	1.7×10^{-3}
Accumulator max. pressure (kPa)	$P_{acc,max}$	1.7×10^{-3}
Accumulator initial volume (m^3)	$V_{acc,0}$	1.0×10^{-3}
Accumulator max. volume (m^3)	$V_{acc,max}$	1.0×10^{-3}
Hydraulic oil grade	-	ISO 32
Downstream conduit radius (m)	$r_{c,down}$	6.25×10^{-3}
Downstream conduit length (m)	$l_{c,down}$	0.4572
Upstream conduit radius (m)	$r_{c,up}$	9.5×10^{-3}
Upstream conduit length (m)	$l_{c,up}$	1.8288
Oil dynamic viscosity $(N\,s/m^2)$	η	0.2742

3.3 Implications of resistive effects and electrohydraulic system dynamics on recruitment state transition

Previous studies have both mathematically and experimentally investigated the force and strain generation of a VR bundle and its transition between recruitment states. Jenkins et al. implemented a model-based recruitment state switching controller and discusses the discontinuities in force and strain that result from modeling errors during transitions [15]. In his

study, an empirically-based tuning method was used to smooth out discontinuities in bundle force that exist when transitioning to a higher recruitment state. Chapman et al. implemented a strategy in which the recruitment state transition occurs when the MUs in the lower recruitment state reaches a preset pressure equal to 90% of the maximum pressure [18]. Meller et al. implements a recruitment logic state machine to switch between recruitment states with separate thresholds for recruitment and de-recruitment [22]. This paper continues to investigate the transition between states in a variable recruitment FAM bundle by introducing two contributing factors: resistive forces and electrohydraulic system dynamics. In this section, the way these factors affect the force and strain during transition are discussed and demonstrated through experiments. Experiments were performed on an in-house built hydraulic testing platform called the linear hydraulic actuator characterization device (LHACD) as illustrated in Figure 3.5. More details about the characterization setup are provided in the paper by Chipka et al. [23].

Figure 3.5: The linear hydraulic actuator characterization device (LHACD) with fluidic artificial muscles (FAMs) used for experiments in this study.

3.3.1 De-slack pressure

As presented in Section 3.2.1, inactive/low-pressure FAMs under compression exert resistive forces that act against fully active ones. A transition to a higher recruitment state is required when the MU of the current recruitment state is saturated and force and/or strain is required from the subsequent MU. Thus, at the initiation of the recruitment state transition, the current MU has fully contracted and the FAMs in the subsequent MU are buckled outwards. In order for the subsequent MU to generate additional bundle force and/or strain, the subsequent MU must reach a *de-slack pressure*, at which the subsequent MU is no longer buckled and its strain has caught up to the strain of the current MU. Figure 3.6 shows the de-slack pressures of MU2 calculated from the model presented in Section 3.2.1 and measured from experiments. Using the LHACD, two MUs were bundled in parallel, and the force and strain of the bundle were measured. Figure 3.6 (a) and Figure 3.6 (b) show analytical results given by the model. The pressure of MU1 is held constant at 1379.0 kPa (200 psi) in Figure 3.6 (a) and 1723.7 kPa (250 psi) in Figure 3.6 (b). Two values of MU1 pressure are shown to demonstrate that the de-slack pressure is dependent on the strain of MU1 and independent of its pressure. For both MU1 pressures, the strain is held constant at three different values: 0.2 (blue), 0.225 (red) and 0.25 (magenta). The overall bundle force is plotted for different values of MU2 pressures. When MU2 pressure is zero, MU2 is in the buckled state. As pressure increases, MU2 remains buckled until it has reached the de-slack pressure indicated by a circle marker. The de-slack pressure is plotted for a range of bundle strain and shown in Figure 3.6(c) along with experimental data for the three different strain values.

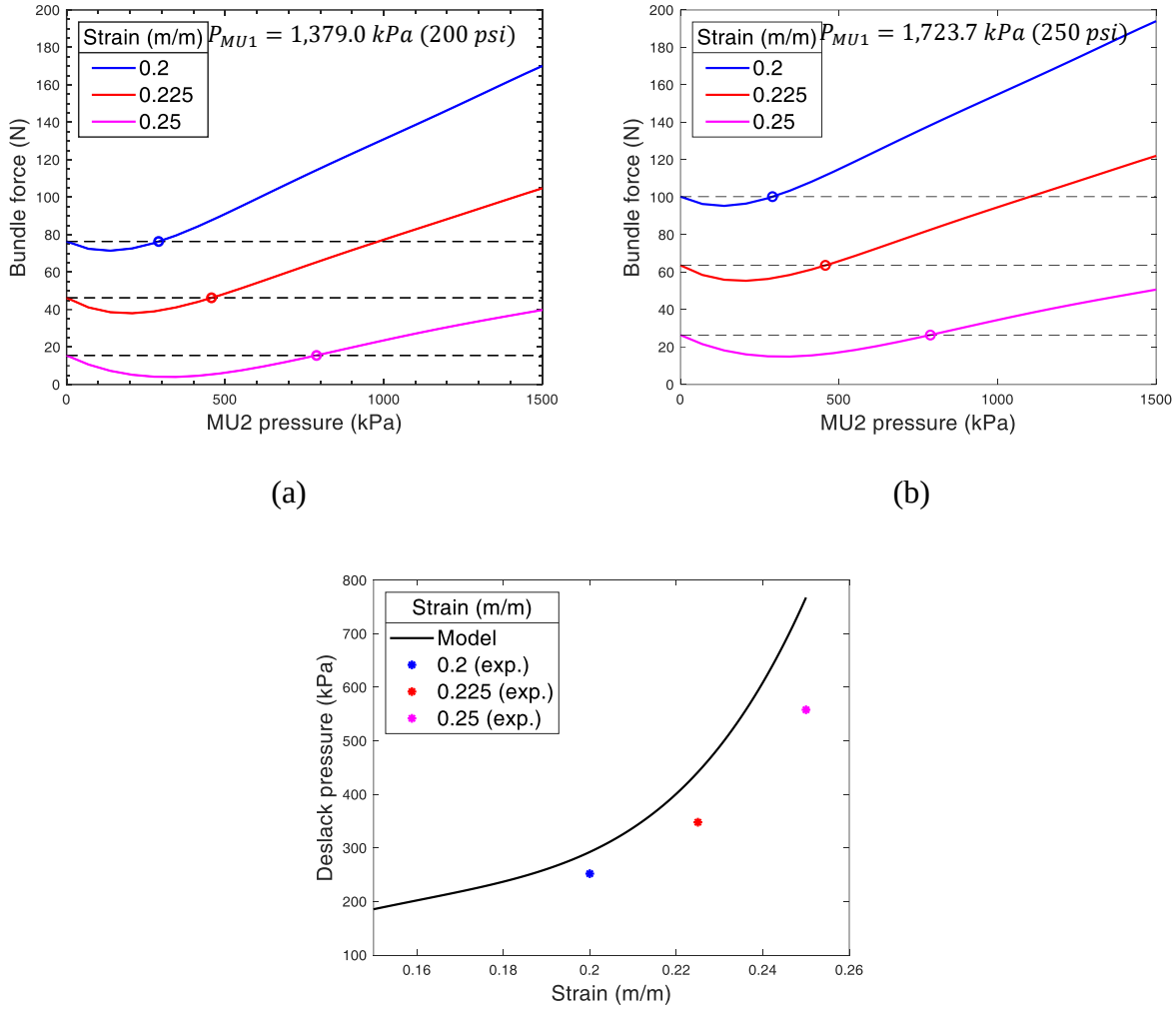

Figure 3.6: Overall bundle force output versus MU2 pressure when MU1 pressure is kept constant at (a) 1379.0 kPa (200 psi) and (b) 1723.7 kPa (250 psi.) The MU2 pressure at which MU2 is able to provide additional force to the bundle is the de-slack pressure of MU2, indicated by markers on (a) and (b). The de-slack pressure of MU2 is dependent on the overall bundle strain as shown by (c).

3.3.2 Resistive forces and pressure compensation

Whenever MU2 is below the de-slack pressure, the buckled FAMs exert resistive forces. This effect is visible in Figure 3.6 as a decrease in the overall bundle force when the MU1 pressure is held constant and the MU2 pressure is increased up to the de-slack pressure. This decrease in bundle force can be prevented via pressure compensation of MU1; i.e. increasing the pressure applied to MU1 while MU2 is being de-slacked. Thus, for a pressure of MU2 below de-slack pressure, there is a corresponding compensation pressure of MU1 that counteracts the resistive forces from MU2. Figure 3.7(a) shows the overall bundle force for a constant MU1 pressure of 1379.0 kPa (200 psi) and varying MU2 pressures. The source pressure is set at 1723.7 kPa (250 psi). Figure 3.7(b) shows the required pressure of MU1 for pressure compensation. For pressure compensation to be effective, the maximum additional pressure required of MU1 must be below the instantaneous *pressure margin*, defined as:

$$P_{margin} = P_{source} - P_{MU}, \tag{3.14}$$

For MU2 pressures that require additional MU1 pressures that are greater than the instantaneous pressure margin, the pressure of MU1 becomes saturated by the source pressure and MU1 is unable to provide enough force to counteract the resistive force of MU2.

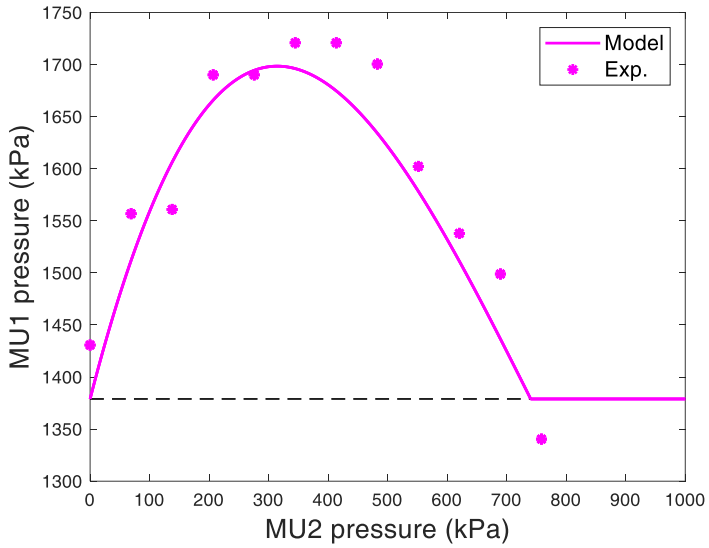

Figure 3.7: Result of pressure compensation using MU1 pressure. The pressure required by MU1 to compensate for the resistive force of MU2 is plotted as a function of MU2 pressure. The conditions for the solid magenta curve shown in (a) are identical to that of the magenta curve of Figure 3.6(a).

3.3.3 Electrohydraulic system dynamics and recruitment lag

Electrohydraulic system dynamics as modeled in Section 3.2, limit the fluid flowrate and the rate of increase of pressure. This results in a lag between when pressure is first applied to a MU and when it begins to provide positive force and strain to the bundle. Figure 3.8 plots an example of model predictions and experimental measurements for the pressure history of a FAM with parameters specified in Table 3.1, connected to the LHACD. Initially, the servo valve is fully closed and at $t = 0$, the servo valve is given a step command to fully open.

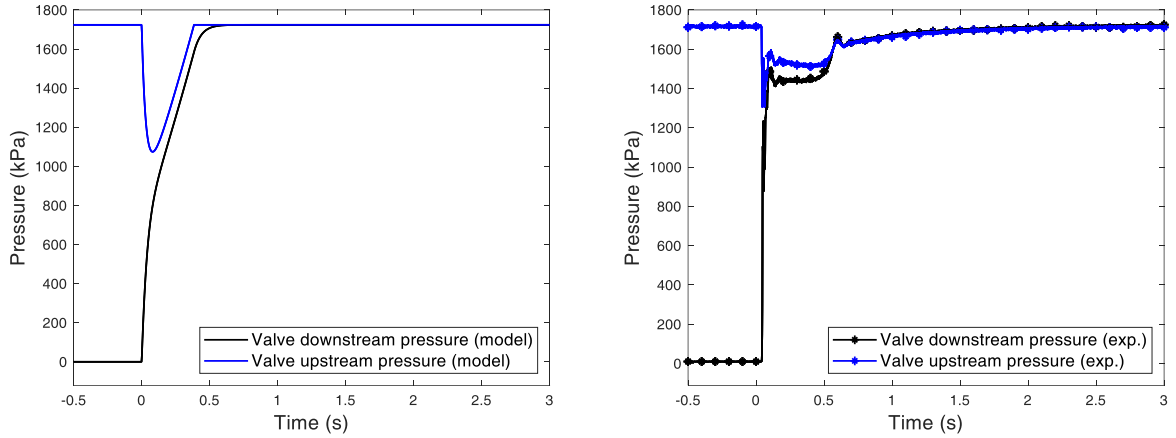

(a) (b)

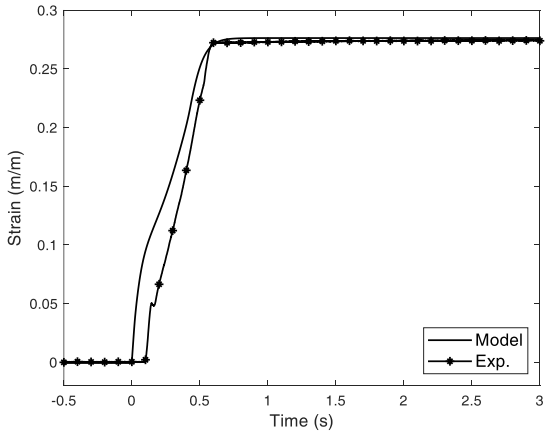

(c)

Figure 3.8: Comparison of (a) model and (b) experimental measurements of fluidic artificial muscle (FAM) open loop pressure growth when valve is fully open at $t = 0$. The strain measurements from the LVDT sensor along with its model prediction are shown in (c).

The model-predicted pressure growth is shown in Figure 3.8(a) while experimental measurements are shown in Figure 3.8(b). The model-predicted and experiment pressures upstream of the servo valve are shown as well. As the valve is opened, the upstream pressure immediately drops to equalize the upstream and downstream pressures. However, the fluid stored in the accumulator and additional fluid input from the motor/pump allows both the upstream and

downstream pressures to increase according to pressure dynamic equations given by (3.8). The discrepancy between the model and experiment pressure growth is due to fluid inertia that is not modeled in this study. However, the model is able to capture the trend of fluid flow between upstream and downstream circuits and the initial pressure growth rate. In a recruitment state transition, these effects result in a *recruitment lag*, which we define as the time from initial MU activation until the MU reaches its de-slack pressure and is able to begin contributing force output to the bundle. Therefore, to prevent this recruitment lag from causing tracking error during recruitment state transitions (which has been reported in prior implementations of variable recruitment [22]), the MU being recruited must be activated sufficiently prior to when additional bundle force is required to track the desired joint trajectory. The recruitment lag, and therefore the minimum amount of time that MU activation must begin before the MU force contribution is needed, is not constant and varies with the instantaneous states of the electrohydraulic system and the strain in the bundle. In this study, inverse dynamics is used to determine the required MU pressures for prescribed sinusoidal trajectories of various amplitudes and frequencies at every instant of time. Then, the electrohydraulic system dynamics required to generate those required pressures are simulated for the purpose of evaluating and comparing system metrics such as efficiency and bandwidth. Because the trajectories are prescribed, the time at which force and strain from MU1 becomes saturated is known. In other words, the required *time to saturation* is known at every instant in time. Making use of this information and calculating the required pressure margin and recruitment lag at each instant of time, the time at which MU2 should be activated to mitigate resistive effects and flowrate restrictions due to the electrohydraulic system dynamics is determined. In summary, we set MU activation to begin when at least one of the following two criteria is met; 1) when the additional pressure required for compensation becomes

greater than the instantaneous pressure margin, or 2) the recruitment lag becomes greater than time to saturation.

3.4 Simulation results and evaluation of system performance

3.4.1 System efficiency and bandwidth limit

The system efficiency of interest is the ratio between the mechanical work output of the actuator and the electrical energy consumed by the motor. During the prescribed sinusoidal motion output of the actuator, the mechanical work done as the actuator contracts, i.e. as the applied load is moved opposing gravity, is of interest.

$$W_{mech.out} = \int F_{actuator} dx, \tag{3.15}$$

where $F_{actuator}$ is the overall force output of the actuator. The electrical energy input into the motor is expressed as:

$$E_{elec,in} = \int P_{motor}\, dt = \int IV\, dt, \tag{3.16}$$

where the motor power, P_{motor}, is the product of motor current and voltage. Finally, the system efficiency is defined as the ratio of actuator mechanical work output to motor electrical energy input expressed as:

$$\eta_{sys} = \frac{W_{mech,out}}{E_{elec,in}}. \tag{3.17}$$

In addition to system efficiency, the bandwidth limit, which is the maximum operating frequency of the system, is evaluated for a single equivalent cross-sectional area motor unit (SEMU) and VR bundle with constant and variable pump displacements. A SEMU is defined as a single FAM for which the dimensions are chosen such that the blocked force and free strain are the same as a VR bundle at its highest recruitment state. The actuator bandwidth is limited by the

flowrate and pressure dynamics of the valve. For example, a FAM may be able to contract for a single cycle at a high frequency using the fluid stored in the accumulator. However, if the flowrate into the accumulator is not able to recharge the accumulator by replacing the depleted fluid and pressure in time for the next actuation cycle, the system cannot maintain cyclic operation. Therefore, the deciding factor in determining the bandwidth of an electrohydraulic system is the ability of the pump to replenish the accumulator volume output within the timespan of a cycle.

3.4.2 Electrohydraulic configuration case studies

Simulations are performed for various amplitude, frequency and loading scenarios to compare the overall system performance metrics such as efficiency and bandwidth. The cases considered can be categorized by the type of actuator and the pump operating configuration. The two actuator types are the SEMU and the VR bundle. Both actuator types are simulated for two different pump operating configurations: constant pump displacement or variable pump displacement. After all the results for each case are presented, a comparison of the efficiencies are discussed in Section 3.4.2.4.

The subsystem models presented in Section 3.2 are used to perform fully-coupled dynamic simulations of a VR bundle and electrohydraulic power system producing sinusoidal actuation under different electrohydraulic configurations. To demonstrate the capabilities of VR, the results are compared to that of a SEMU. FAM dimensions for the VR bundle are identical to that of Table 3.1 and dimensions of the SEMU are summarized in Table 3.3 and remain the same for all cases.

Table 3.3: SEMU dimensions and system parameters.

SEMU	Initial inner radius (m)	r_0	0.0088
	Initial thickness (m)	t_0	0.001
	Initial braid angle (°)	α_0	33
	Initial length (m)	L_0	0.2286
	Initial position (m)	x	0
	Initial velocity (m/s)	$\dot{x}$	0

3.4.2.1 Case 1: Continuous motor operation with constant pump displacement

In the first electrohydraulic configuration case considered, the pump displacement remains constant while the motor runs continuously. The electrohydraulic system circuit containing the subsystems modeled in Section 3.2 is illustrated in Figure 3.9.

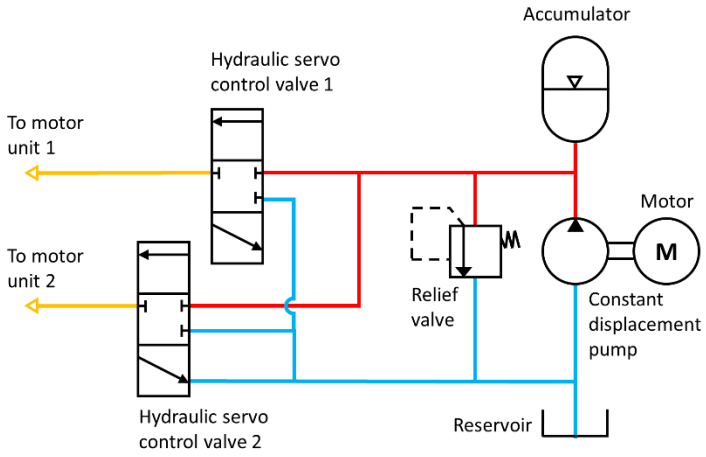

Figure 3.9: Electrohydraulic system circuit for Case 1: Continuous motor operation with constant pump displacement

The ratio between flowrate output of the pump and the motor speed remains constant as expressed by:

$$Q_p = D_{p,const}\dot{\theta}, \tag{3.18}$$

where Q_p is the pump flowrate output and D_{const} is the constant pump displacement. The pump is decoupled from the volume requirement of the bundle during actuation. When the accumulator is full and has reached its maximum pressure, the excess fluid out of the pump returns back to the reservoir through a relief valve. The initial conditions are presented in Table 3.4 and the simulated results for both a SEMU and a VR bundle are shown in Figure 3.10.

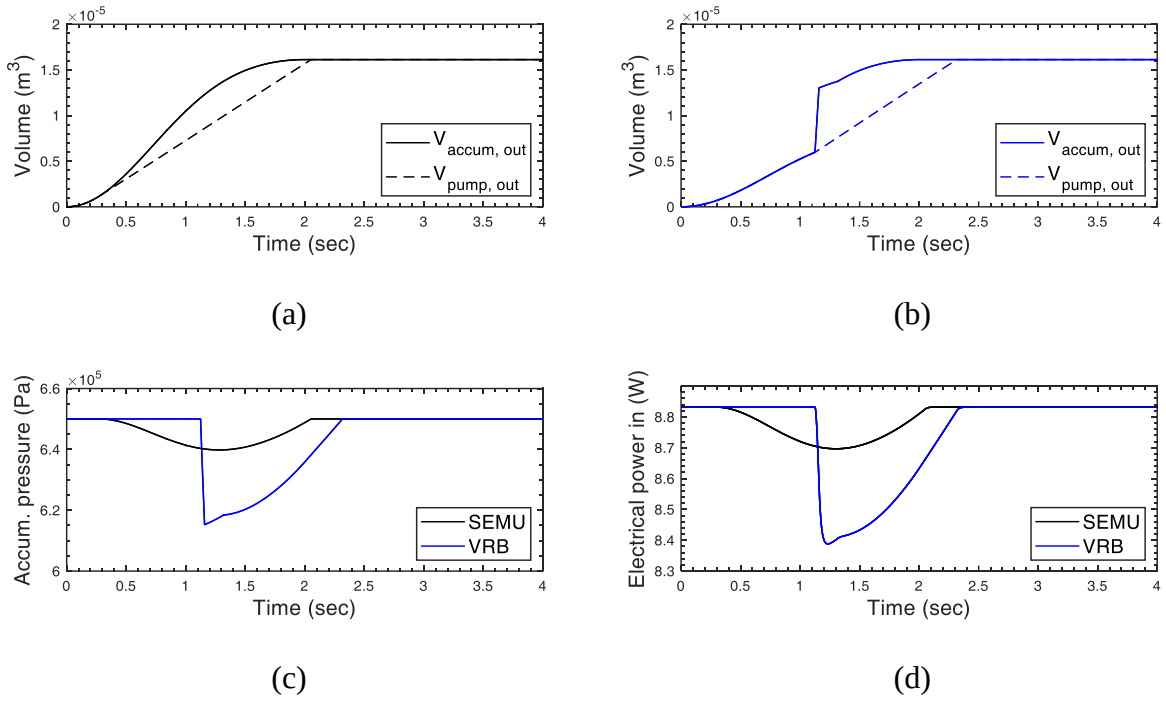

Figure 3.10: Volume simulation results for (a) single equivalent cross-sectional area motor unit (SEMU) and (b) variable recruitment (VR) bundle. The (c) accumulator pressures and (d) motor input electrical powers for both SEMU and VR bundle are shown in comparison. A sinusoidal contraction with an amplitude of $x/L_0 = 0.232$ and frequency of 0.25 Hz is simulated with a hanging mass weighing 20% of the actuator blocked force ($mg/F_{bf} = 0.2$).

A prescribed sinusoidal contraction with frequency of $0.25\,Hz$ and an amplitude of $x/L_0 = 0.232$ is tracked for both SEMU and VR bundle cases. For the VR bundle, the sinusoid is tracked using the method presented in Section 3.3.1. In case of the SEMU, the required pressure or volume is continuous and thus, does not require the anticipation and compensation methods previously discussed. A hanging mass weighing 20% $(mg/F_{bf} = 0.2)$ of the overall actuator blocked force attached to the end of the actuator. Initially, the accumulator is at its maximum pressure as shown in Figure 3.10(c). While the volume output from the pump into the accumulator is greater than that of the actuator, the accumulator pressure remains constant at maximum pressure. However, as the volume required by the actuator exceeds the pump output capability, the fluid stored in the accumulator is used and thus, the accumulator pressure decreases. Consequently, the electrical power required by the motor decreases as the torque required by the pump decreases while motor speed increases. The total fluid volumes required for one cycle of contraction are equal for both actuators. However, the fluid required by the VR bundle during recruitment state 1 is lower than that of a SEMU. A sharp increase in volume is observed for the VR bundle when the transition from recruitment state 1 to 2 occurs. This difference in required volume impacts the bandwidth performance of the actuation system.

Table 3.4: System parameters for Case 1: Continuous pump operation with constant pump displacement

			SEMU	VR bundle
Motor	Initial current (A)	I	0.49	
	Initial speed (rad/s)	$\dot{\theta}$	656.7	
Pump	Displacement (ml/rev)	$D_{p,const}$	0.08	

The system efficiency and bandwidth limit for a sinusoidal contraction operating with constant pump displacement values of 1.27×10^{-8} $\mathrm{m}^3/\mathrm{rad}$ $(0.08$ $\mathrm{ml/rev})$ and 0.32×10^{-8} $\mathrm{m}^3/\mathrm{rad}$ $(0.02$ $\mathrm{ml/rev})$ are evaluated by varying its amplitude and frequency and shown in Figure 3.11 and Figure 3.12, respectively. For the higher pump displacement case, the simulated range of amplitude is 0.01 m to 0.023 m and a frequency range of 0.2 Hz to 0.8 Hz. The load applied is $\mathrm{mg/F_{bf}} = 0.2$. The color bar limits are equivalent across Figure 3.11 to Figure 3.18 in order to make the system efficiencies comparable. For both pump displacement values, the system efficiencies for SEMU and VR bundle within the limits of the bandwidth of the SEMU actuator are nearly identical with differences less than 0.1%. A similar result has been reported by Chapman et al. when using a FAM model neglecting resistive forces [13]. Given the same amplitude and frequency, a VR bundle operating in a recruitment state other than its highest recruitment state requires less volume relative to a SEMU. The use of less fluid volume translates to less energy input and thus increases the downstream actuator efficiency [9]. However, this does not lead to an increase in overall system efficiency for this configuration. As shown by the motor/pump subsystem (3.11)-(3.13) and demonstrated in Figure 3.10, the motor power is determined by the accumulator pressure, as it determines the torque load applied to the motor. The lower volume requirement of a VR bundle at lower recruitment states results in a smaller drop in accumulator

pressure and thus a slightly lower motor load, to which the minute differences in efficiency (<0.1%) can be attributed. However, such differences in torque applied to the motor are negligible compared to effects of pump fluid volume loss through the relief valves. The fluid volume output from the pump remains nearly identical between a SEMU and VR bundle and is independent of the volume requirements of the actuator. Although the system efficiency is marginally affected by the low volume requirement of a VR bundle, it broadens the amplitude and frequency space in which the actuator can operate. The bandwidth limits for a SEMU and a VR bundle operating at its highest recruitment state are identical. However, the bandwidth limit is higher for a VR bundle when operating at a lower recruitment state as shown in Figure 3.11. The tradeoff between efficiency and bandwidth limit is demonstrated in Figure 3.11 and Figure 3.12 showing the two pump displacement values. The frequency range for the low pump displacement case is shown for only 0.2 Hz to 0.5 Hz. While a higher pump displacement broadens the actuation frequency range, the efficiencies are higher for motions that are within the bandwidth limit of the lower pump displacement case.

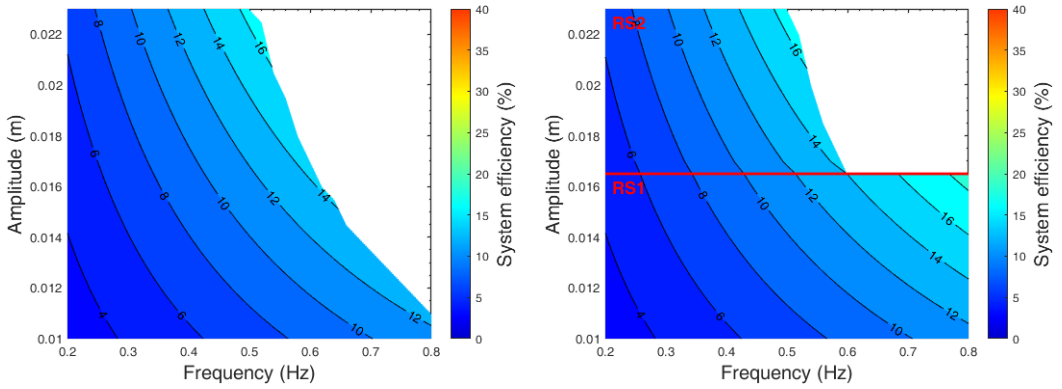

(a) (b)

Figure 3.11: Comparison of efficiency and bandwidth limit with continuous motor operation and constant pump displacement of $1.27 \times 10^{-8}\ m^3/rad$ $(0.08\ ml/rev)$ for (a) SEMU and (b) variable recruitment (VR) bundle. Applied load is 20% of the actuator blocked force $(mg/F_{bf} = 0.2)$.

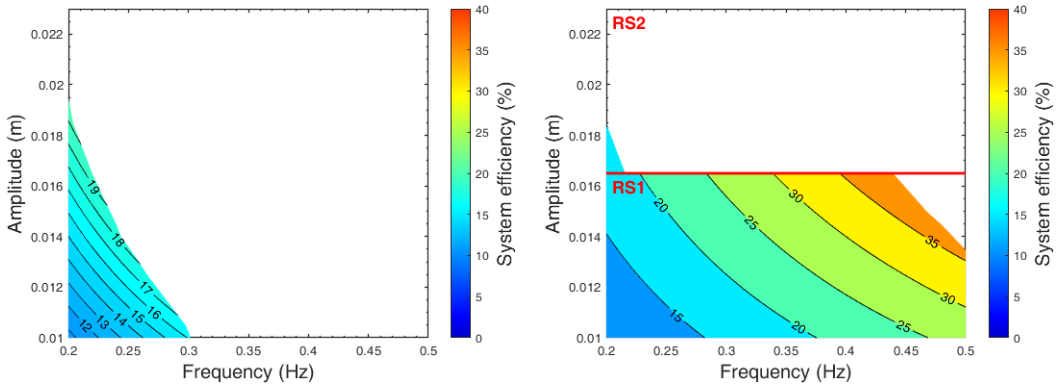

(a) (b)

Figure 3.12: Comparison of efficiency and bandwidth limit with continuous motor operation and constant pump displacement of $0.32 \times 10^{-8}\ m^3/rad$ $(0.02\ ml/rev)$ for (a) SEMU and (b) variable recruitment (VR) bundle. Applied load is 20% of the actuator blocked force $(mg/F_{bf} = 0.2)$.

3.4.2.2 Case 2: Intermittent motor operation with constant pump displacement

In the second electrohydraulic configuration considered, the pump operates intermittently in response to the accumulator pressure. During continuous motor operation, the excess fluid from the pump flows through the relief valve and back to the reservoir, wasting energy. When the accumulator pressure is close to or at its maximum value, there is no need for the motor to keep running. Therefore, by intermittently turning the motor on and off according to the accumulator pressure has potential to reduce energy losses and increase system efficiency. The fluid volumes into the actuators and out of the pump as well as the accumulator pressures for both SEMU and VR bundle are identical to Case 1. The main difference is demonstrated by the power input to the motor. At time zero, a current spike is observed when the motor is turned on. As the accumulator pressure reaches its maximum value, the motor is switched off until the start of the next contraction cycle.

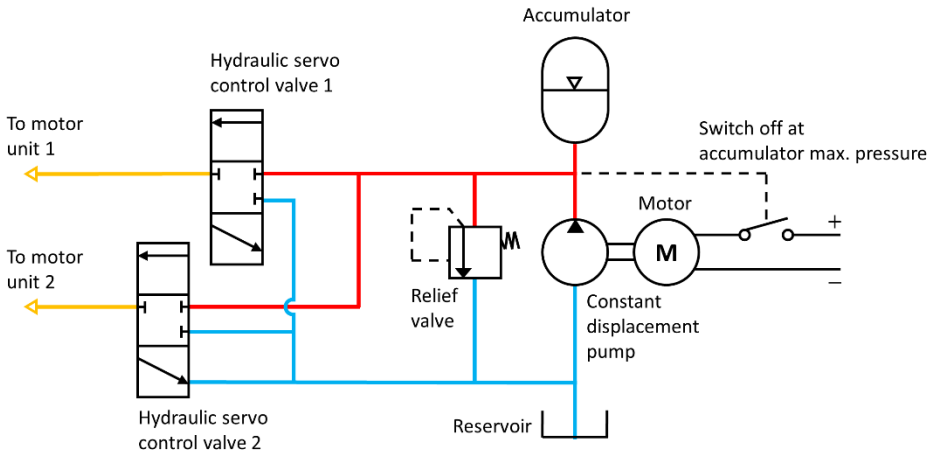

Figure 3.13: Electrohydraulic system circuit for Case 2: Intermittent motor operation with constant pump displacement.

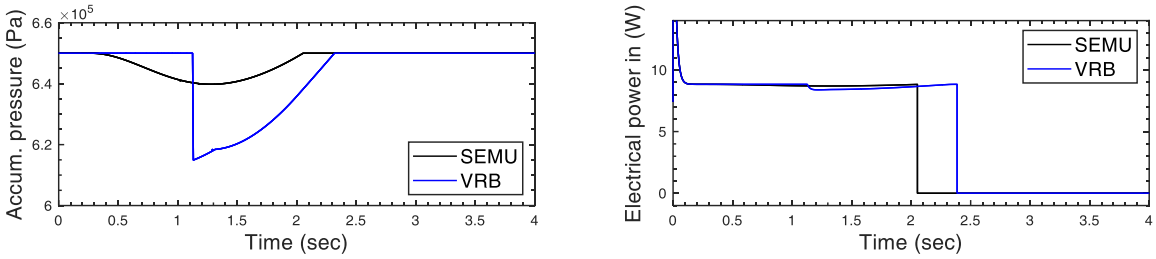

(a) (b)

Figure 3.14: The (a) accumulator pressures and (b) motor input powers for both SEMU and VR bundle during intermittent motor operation are shown in comparison. A sinusoidal contraction with an amplitude of $x/L_0 = 0.232$ and frequency of 0.25 Hz is simulated with a hanging mass weighing 20% of the actuator blocked force ($mg/F_{bf} = 0.2$).

Table 3.5: System parameters for Case 2: Intermittent pump operation with constant pump displacement

			SEMU	VR bundle
Motor	Initial current (A)	I	0	
	Initial speed (rad/s)	$\dot{\theta}$	0	
Pump	Displacement (ml/rev)	$D_{p,const}$	0.08	

Simulations are performed for identical constant pump displacement, sinusoidal contraction amplitude and frequency ranges as Case 1 but with intermittent motor operation. A significant increase in system efficiency can be observed for both SEMU and VR bundle actuators. Although the motor initially requires more power during startup, the energy conserved by turning off the motor is much greater. The effectiveness of intermittent motor operation is noticeable by comparing the SEMU efficiencies shown in Figure 3.11(a) and Figure 3.15(a). Also, the efficiencies for a VR bundle operating with intermittent motor operation are shown in Figure

3.15(b). Compared to the continuous motor operation case in Figure 3.11(b), an increase in efficiency is observed over the entire amplitude-frequency space.

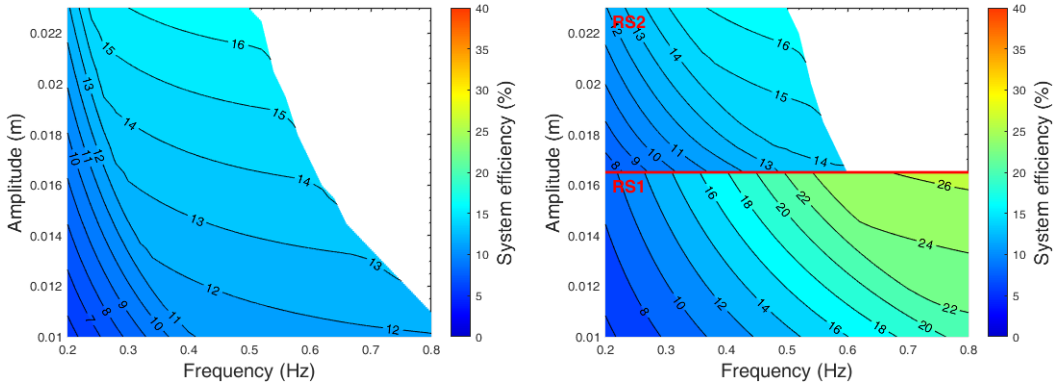

(a) (b)

Figure 3.15: Comparison of efficiency and bandwidth limit with intermittent motor operation and constant pump displacement of $1.27 \times 10^{-8}\ m^3/rad$ $(0.08\ ml/rev)$ for (a) SEMU and (b) variable recruitment (VR) bundle. Applied load is 20% of the actuator blocked force $(mg/F_{bf} = 0.2)$.

3.4.2.3 Case 3: Continuous motor operation with variable pump displacement

The third electrohydraulic configuration case considered is when the pump displacement is able to adjust itself to the volume needs of the actuator. The system circuit is identical to Case 1 as shown in Figure 3.9 with the except of the constant displacement pump which is replaced with a variable displacement pump. In the constant pump displacement case with continuous motor operation, fluid output of the pump that exceeds the maximum accumulator volume must flow through a relief valve back to the reservoir, resulting in excess motor energy consumption. The purpose of variable pump displacement is to minimize this loss by using knowledge of the volume required by the actuator to instantaneously adjust the pump displacement. It should be noted that

this study assumes that no energy is required to change the pump displacement and that the displacement is able to change instantaneously in response to volume demand.

The change in pump displacement in response to the actuator volume needs are shown in Figure 3.16(b). The change in volume and accumulator pressure remains the same as the constant displacement case. For the system to be comparable, the maximum pump displacement is set equal to that of the constant pump displacement case. During operation, the accumulator fluid volume is depleted when the volume required by the actuator is greater than the fluid volume supplied by the pump, which results in a decrease in accumulator pressure. In such circumstances, no fluid from the pump is wasted through the relief valve and the pump operates at maximum displacement. However, when the accumulator pressure is at its maximum, the pump displacement is adjusted to a sub-maximal value. The displacement range and the initial conditions are summarized in Table 3.6. The change in pump displacement does not affect the contraction as the volume supplied to the actuator remains the same as the constant pump displacement case. However, the current drawn by the motor at sub-maximal pump displacement values is lower than when the pump displacement is constant. Additionally, lower pump displacement results in faster motor speeds, which can allow the motor to operate more efficiently. As a result, a significant decrease in motor power can be observed as shown in Figure 3.16(a) compared to cases 1 and 2 shown in Figure 3.10(d) and Figure 3.14(b), respectively.

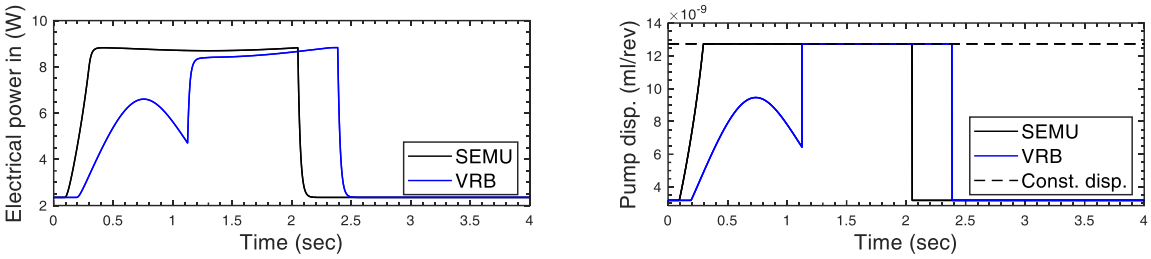

(a) (b)

Figure 3.16: The (a) motor electrical power input and (b) pump displacement for both single equivalent cross-sectional area motor unit (SEMU) and variable recruitment (VR) bundle. A sinusoidal contraction with an amplitude of $x/L_0 = 0.232$ and frequency of 0.25 Hz is simulated with a hanging mass weighing 20% of the actuator blocked force ($mg/F_{bf} = 0.2$).

Table 3.6: System parameters for Case 3: Continuous pump operation with variable pump displacement

			SEMU VR bundle
Motor	Initial current (A)	I	0.13
	Initial speed (rad/s)	$\dot{\theta}$	947.2
Pump	Max. displacement (ml/rev)	$D_{p,var,max}$	0.08
	Min. displacement (ml/rev)	$D_{p,var,min}$	0.02

The simulation results for variable pump displacement operation for applied load values of $mg/F_{bf} = 0.2$ and $mg/F_{bf} = 0.28$ are shown in Figure 3.17 and Figure 3.18. The simulations are conducted using identical sinusoid amplitude and frequency ranges as the constant pump displacement case. The effectiveness of variable pump displacement is noticeable by comparing the SEMU efficiencies shown in Figure 3.11(a) and Figure 3.17(a). The efficiencies for a VR bundle operating with variable pump displacement are shown in Figure 3.17(b).

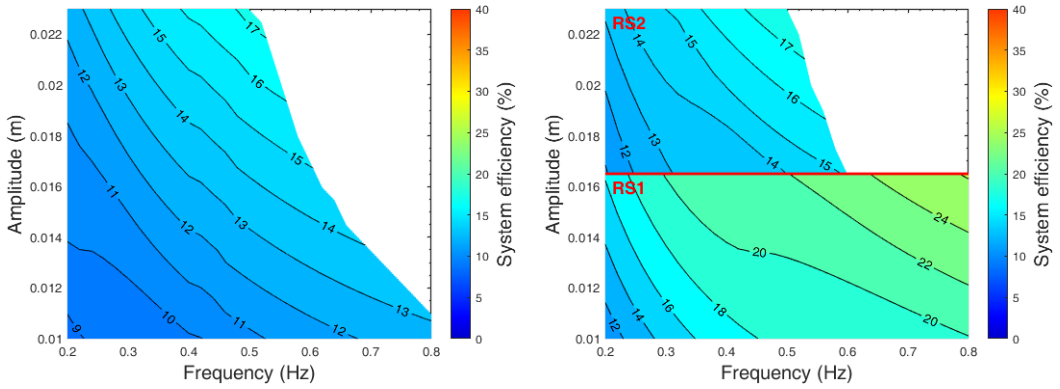

(a) (b)

Figure 3.17: Comparison of efficiency and bandwidth limit with continuous motor operation and variable pump displacement from $0.32 \times 10^{-8}\ m^3/rad$ $(0.02\ ml/rev)$ to $1.27 \times 10^{-8}\ m^3/rad$ $(0.08\ ml/rev)$ for (a) SEMU and (b) variable recruitment (VR) bundle. Applied load is 20% of the actuator blocked force $(mg/F_{bf} = 0.2)$.

The amplitude-frequency efficiency map for a higher loading condition is shown in Figure 3.18. It has been shown for isotonic contractile motions, the downstream actuator efficiency is higher for higher loads [22], during which there are less valve throttling losses. Although the simulation is not for isotonic loading conditions, the same principles apply that increase the downstream efficiency of the actuator and thus increasing overall system efficiency.

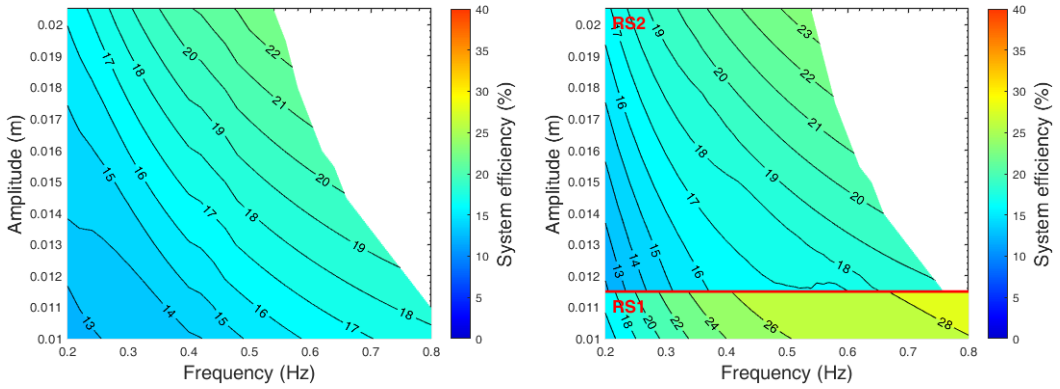

(a) (b)

Figure 3.18: Comparison of efficiency and bandwidth limit with continuous motor operation and variable pump displacement from $0.32 \times 10^{-8}\ m^3/rad$ $(0.02\ ml/rev)$ to $1.27 \times 10^{-8}\ m^3/rad$ $(0.08\ ml/rev)$ for (a) SEMU and (b) variable recruitment (VR) bundle. Applied load is 28% of the actuator blocked force $(mg/F_{bf} = 0.28)$.

3.4.2.4 Case study results comparison

The percentage increases in average efficiency with respect to frequency is shown in Figure 3.19 for the amplitude and frequency ranges considered. The average efficiency for a given frequency is computed for each case study using results from Figure 3.11, Figure 3.15, and Figure 3.17. The average efficiency for the SEMU in Case 1 is used as the baseline case to which other average efficiencies are compared. The lines in black compare the SEMU actuators of Case 2 and Case 3 to Case 1. The blue lines compare the VR bundle actuators of Cases 1, 2, and 3 to the SEMU actuator of Case 1.

The efficiency increases due to the electrohydraulic configuration changes alone are demonstrated by the black lines that compare the average efficiencies of SEMUs. These results show that changing the electrohydraulic configuration to either and intermittently-operating constant displacement pump (Case 2) or a variable displacement pump (Case 3) can produce

significant average efficiency improvements at lower frequencies, even with a SEMU actuator. For Case 2, this can be attributed to a larger fraction of the cycle period with the motor turned off. Similarly for Case 3, the variable displacement of the pump results in energy savings during a larger fraction of the cycle.

The blue lines in Figure 3.19 illustrate the effects of combining the VR bundle actuator with each electrohydraulic configuration. Compared to the SEMU, the VR bundle for Case 1 shows a slight increase in average efficiency at higher frequencies which can be attributed to the functionality of the VR bundle that requires less fluid volume while operating in recruitment state 1. While the efficiencies of a VR bundle for Case 1 may even decrease compared to a SEMU at lower frequency ranges due to the presence of resistive forces, the efficiencies of VR bundles for Cases 2 and 3 show a significant efficiency increase for the entire frequency range considered. For Case 3, this frequency-dependent behavior depends on the fraction of cycle period that is spent at maximum pump displacement. At higher frequencies, the pump is operating at its maximum displacement for a larger percentage of the contraction cycle. As the frequency decreases, the time during which the pump operates at its maximum displacement becomes shorter. At lower frequencies, the potential to conserve energy is greater due to the fact that the amount of fluid energy loss through the relief valve is greater than at higher frequencies. Using variable pump displacement minimizes the relief valve energy losses and thus shows a greater increase in average efficiency at lower frequencies. Due to the ability of the variable displacement pump to beneficially take advantage of reductions in the required fluid volume with the VR bundle, this combination shows the largest efficiency gains.

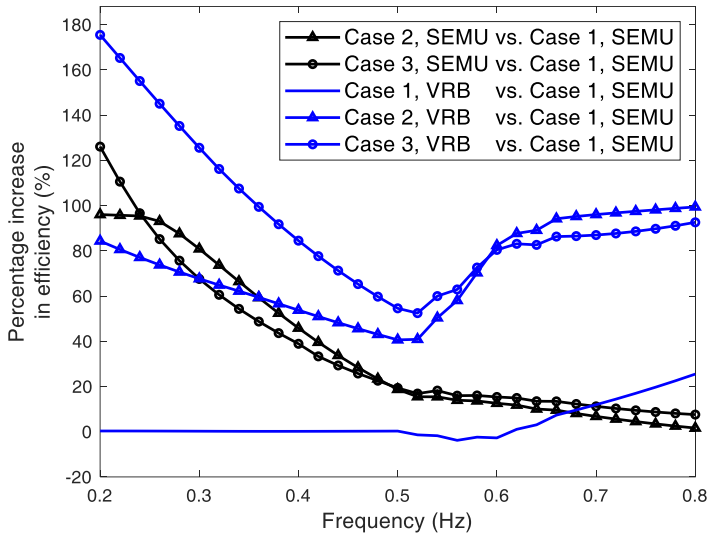

Figure 3.19: Percentage increase in system efficiency of various cases with respect to the SEMU actuator in Case 1. Black lines compare the efficiencies of SEMUs for different cases to demonstrate the effects of the electrohydraulic configuration changes alone. Blue lines illustrate the efficiency increases due to using variable recruitment (VR) in combination with each electrohydraulic configuration case.

3.5 Conclusion

In this study, a FAM model that is able to capture the inter-FAM forces within a VR bundle is used to simulate actuation under load. Previous models that neglect the resistive forces of inactive/low-pressure FAMs were not able to fully convey the complicated force-strain space of a VR bundle, such as the overlapping region between recruitment states. By modeling the inter-FAM resistive forces and electrohydraulic system dynamics, this study more accurately captures the hydraulic pressure, flow rate, and motor current demand during the recruitment transition, thereby enabling analysis of system-level electromechanical efficiency for prescribed actuation trajectories. A system model including the motor/pump, accumulator and valve subsystems is

presented and used to simulate sinusoid trajectories for a SEMU and a VR bundle with two recruitment states. For each type of actuator, dynamic simulations were run for continuous and intermittent motor operation and fixed and variable pump displacement configurations. The results from the continuous motor operation with constant pump displacement case showed that a SEMU and a VR bundle had nearly identical efficiencies. However, the low volume requirement of a VR bundle during lower recruitment states allowed the VR bundle actuator to operate in a broader range of frequencies. Simulation results from the intermittent motor operation with constant pump displacement showed increased efficiencies for both SEMU and VR bundles actuator types. Further increases in efficiency were shown to be possible by using variable pump displacement condition with continuous motor operation. The percentage increase in efficiency was dependent on the trajectory frequency, showing greater percentage increases at lower frequencies. The benefits of variable pump displacement were even greater for a VR bundle especially for lower recruitment states, indicating that variable displacement pump configurations may be well-suited to take advantage the reduced working fluid demand created by VR bundle actuators.

CHAPTER 4

Model-based control allocation during state transitions of a variable recruitment fluidic artificial muscle bundle

A model-based control scheme for state transitions of a variable recruitment fluidic artificial muscle (FAM) bundle is developed and experimentally validated. FAMs can be bundled together in parallel to exhibit variable recruitment functionality which is an activation strategy inspired by how motor units (MUs) in skeletal muscle are recruited. By adapting variable recruitment, a FAM bundle is able to operate efficiently over its entire force-contraction space while increasing control authority and bandwidth at low recruitment states. A variable recruitment bundle poses a hybrid control problem as it operates by controlling pressure as a continuous variable while simultaneously shifting between discrete recruitment states. During such state transitions, the bundle may experience a lag in strain if the shift timing is not properly anticipated. In this study, a model that captures the interaction effects between FAMs and a hydraulic system model is used to inform the controller of when a state transition should be made. The proposed control scheme is compared to a baseline control scheme that uses a percentage of the source pressure as the threshold for when a shift is made. The controller performance is evaluated by tracking a sinusoidal strain trajectory and the average and maximum strain errors are compared between the baseline and proposed controller. The applied FAM pressures are presented to show that the model-based compensation is able to determine when a transition needs to be made. As a result, the tracking performance of the proposed control scheme is shown to significantly decrease the integrated absolute and maximum errors.

4.1 Introduction

Fluidic artificial muscles (FAMs), also known as McKibben actuators, are either pneumatically or hydraulically powered actuators known for their compliance and high power-to-weight ratios [1], [14]. As originally conceived, FAMs are biomimetic single-acting linear actuators that, when pressurized, generate tensile force and axial contraction. The double-helix pattern mesh that is wrapped around an inner elastic bladder constrains the FAM to contract axially while expanding radially. Over the years, structural design alterations have been proposed to create different functionalities such as adding inelastic layers or inner reinforcements to produce bending or twisting motions [29], [55]–[57]. Others have developed FAMs with integrated force or strain sensing functionalities using various means including shape memory polymers or liquid metals [57]–[60]. The arrangement of FAMs into bioinspired pennate topologies have also been explored [7], [8]. The biomimetic contraction production of FAMs has attracted the interest of the robotics research community for applications such as assistive devices, orthoses, and exoskeletons as an actuation method that can augment or even replace the human skeletal muscle in the form of prosthetics [61]–[64].

FAMs, however, are fundamentally different from skeletal muscle in that they use fluid power as their activation method. The activation of skeletal muscle relies on the firing of neurons to recruit subunits of a muscle called motor units (MUs). The physiological scheme by which MUs are recruited is called the Henneman's Size Principle, stating that MUs are sequentially recruited from smallest to largest [12]. An active area of research is applying this physiological recruitment strategy to FAMs by assembling multiple FAMs together in parallel to create a bundle with variable recruitment functionality, bringing FAMs closer to skeletal muscles [9]–[11], [30]. Within a bundle, a single or multiple FAMs are grouped together as a MU for which the pressure is

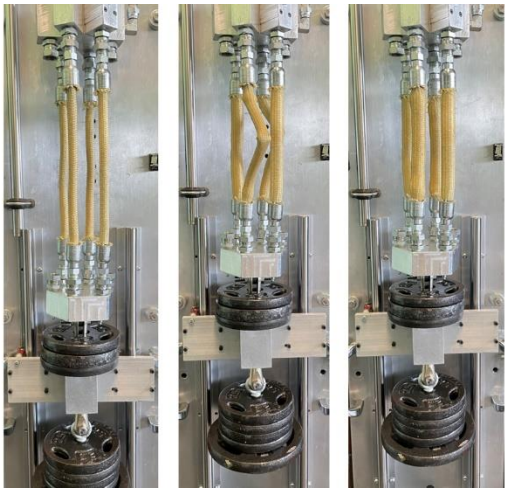

(a) (b) (c)

Figure 4.1: Variable recruitment fluidic artificial muscle (FAM) bundle with two motor units (MUs), each consisting of two FAMs in the (a) inactive resting state, (b) first recruitment state showing buckling of inactive/low-pressure FAMs, and (c) second recruitment state with all MUs fully active.

controlled separately to mimic the orderly activation of skeletal muscle as shown in Figure 4.1. This arrangement allows MUs to be either inactive (i.e. vented to the reservoir) or activated (i.e. pressurized) to meet the total force demand of the bundle while minimizing the working fluid volume consumption of the bundle. This scheme was first proposed by Bryant et al. and been shown to improve the average efficiency of the actuator across its force-contraction operating range by decreasing losses due to throttling and allow precise control by decreasing the force sensitivity to pressure at low recruitment states [9]. It has also been shown to increase actuation bandwidth at low recruitment states [13]. Different implementations of variable recruitment have been investigated. In batch recruitment, all recruited MUs are pressurized equally and the applied pressure is controlled to meet the desired force output [30]. Orderly recruitment takes a more biomimetic and sequential approach wherein newly-recruited MUs are subject to pressure while

the previously-recruited MUs are held at saturation pressure [21], [30]. Extensive research has been done on the control FAMs acting as independent actuators [65]–[71]. However, there are limited controller studies on the variable recruitment of FAM bundles [11], [22]. Variable recruitment bundle control poses an interesting challenge especially during recruitment state transitions. Meller et al. applies a batch recruitment implementation of variable recruitment and reports a lag in position tracking due to newly-recruited FAMs requiring time to fill up with working fluid [22]. A variable recruitment bundle is fundamentally similar to automotive transmission in that they shift in between finite states of operation [72], [73]. The lag effect described by Meller et al. can be thought of as analogous to the jerk event caused when shifting gear ratios. For automotive transmission, the motivation to reduce jerk lies in the comfort of passengers and to reduce shifting times while the focus of variable recruitment, the lag caused in between shifts affects its tracking performance [74]–[76].

The purpose of this study is to develop and test a controller for a variable recruitment hydraulic FAM bundle and improve its tracking performance by 1) using a model-based anticipatory method of determining when recruitment state transitions should be initiated and 2) using a model-based feedback term to account for interaction effects between FAMs. The decision to shift recruitment states is based on a hydraulic system model that takes into account the system pressure dynamics to enable anticipatory action. The pressure feedback term is based on a FAM model that captures the resistive effects of FAMs in compression within a bundle to improve position tracking during state transitions. The controller uses a cascaded structure that consists of a strain feedback outer loop with a pressure feedback inner loop. The controller used to track a sinusoidal trajectory and the integrated absolute and maximum strain errors are presented. The case of a bundle with two MUs (and therefore two recruitment states) is considered throughout

this study for simplicity, but the methods are readily extended to bundles with greater numbers of MUs.

This paper is organized in the following way. In Section 4.2, the models for the FAM and hydraulic system used and their basis for control design is established. In Section 4.3, the proposed model-based control design is introduced. In Section 4.4, the experimental setup is explained. The results are presented in Section 4.5 and the conclusions are summarized in the last section.

4.2 Modeling

4.2.1 FAM Modeling including resistive effects during compression

The force output of a FAM depends on its strain and the pressure applied. This relationship is often referred to as the ideal force model which is expressed in [19] as:

$$F_{ideal} = F_{mesh} = \pi r_0^2 P \left(\frac{1}{tan^2 \alpha_0} (\varepsilon - 1)^2 - \frac{1}{sin^2 \alpha_0} \right) \quad (4.1)$$

where, r_0 is the initial radius of the FAM, P is the applied pressure, ε is the strain, and α_0 is the initial braid angle. This model captures the axial force generated by the expanding bladder constrained by the braided mesh. Others have since further developed the model by adding effects such as bladder hyperelasticity, bladder wall thickness or tapered end geometry [1], [17], [49]. In this study, a model that also captures the axial force of a FAM as it is compressed beyond its free strain is used [21]. During operation of a variable recruitment bundle, different pressures may be applied to each MU which inevitably results in a strain difference between MUs. This strain difference causes FAMs that are at lower pressures to compress, exerting a resistive force that acts against the active force generation of higher pressure FAMs. Within the tensile region, this model uses the sum of mesh and bladder forces as the total force of a FAM developed by Klute and Hannaford expressed as [18]:

$$F_{total} = F_{mesh} + F_{bladder} = P\frac{dV}{dL} - V_b\frac{dW}{dL}, \quad (4.2)$$

where $F_{bladder}$ is the force contribution due to the hyperelasticity of the bladder and V_b is the volume of the incompressible bladder. The Mooney-Rivlin strain energy function, W, is used to characterize the energy stored and the principle of virtual work is applied to model the elastic bladder force. As the FAM is compressed past its free strain, the resistive forces when the FAM is buckled is expressed as:

$$F_{total} = F'_{mesh} + F_{bladder}(\varepsilon_{free}) + F_b \quad (4.3)$$

where F'_{mesh} is the braided mesh force using the arc length of the FAM in its buckled shape and ε_{free} is the free strain. F_b is the bladder force in the axial direction required for static equilibrium of the bladder to maintain its buckled shape, calculated using the total potential energy stored. When a FAM is further compressed in its buckled state the internal moment generated along the FAM reaches a critical value at which it collapses and folds upon itself. The resistive forces when the FAM has collapsed can be expressed by:

$$F_{total} = F_c + (F_b - F_c)^{-\beta(\varepsilon-\varepsilon_c)} \quad (4.4)$$

where F_c is the axial force of the bladder in its collapsed shape and ε_c is the strain at collapse. The transition from buckled to collapsed regions is characterized by β which is tuned based on parameter optimization. Description of this model and the presence of resistive forces are detailed in the paper by Kim et al. [21].

This model reveals two interesting effects that take place when a recruitment state shift occurs. The first is the *resistive effect* that results in a decrease in bundle overall force due to resistive forces of FAMs in compression. The second is the *de-slack effect* due to the non-zero pressure required by the subsequent MU during recruitment state upshift. The purpose of the

proposed controller design is to address both of these effects to improve tracking performance during recruitment state transitions. The resistive effect is addressed by *pressure compensation* and the de-slack effect discussed further in Section 4.3.2 and addressed by *lag compensation*.

B. Hydraulic system model

The pressures applied to MUs in a practical control application are heavily dependent on the dynamics of the hydraulic system. As discussed in Section 4.2, the subsequent MU being recruited needs to de-slack before additional force can be generated by the FAM bundle. A hydraulic system model is used to understand the pressure dynamics associated with de-slacking for the purpose of estimating the lag between when state transition is initiated and when the subsequent MU reaches its de-slack pressure and therefore begins contributing force to the bundle output. Figure 4.2 illustrates the hydraulic system that is used to deliver power to the FAMs including the hoses through which fluid is delivered, the hydraulic servo values (EHSVs) used for independent pressure control for each MU, and the pressure reducing/relief valve (PRRV) used to regulate the pressure upstream of the EHSVs.

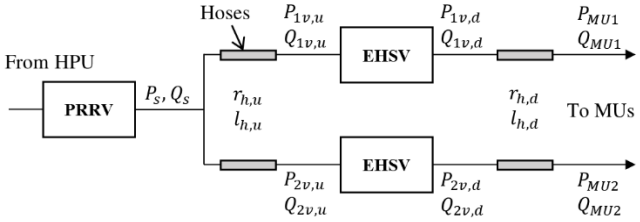

Figure 4.2:Diagram of the hydraulic system

The PRRV acts as the fluid power supply and the output pressure is henceforth referred to as the *source pressure*, P_s, which the PRRV tries to maintain as its nominal setting value, $P_{s,nom}$. P_s is dependent on the flowrate through the valve, Q_s, for which the pressure-flowrate relationship

is typically given by the manufacturer for selected setting values. For this study, the relationship is experimentally characterized and presented in Section 4.4. The flowrate equation through the EHSV is given as:

$$Q_{v,d} = c_v d_v sgn\left(P_{v,up} - P_{v,d}\right)\sqrt{\left|P_{v,u} - P_{v,d}\right|}, \tag{4.5}$$

where, d_v is the port diameter, $P_{v,u}$ is the pressure upstream of the valve and $P_{v,d}$ is pressure immediately downstream. The flow coefficient, c_v, is calculated using the nominal flowrate, Q_N, and nominal pressure drop, Δp_N, across the maximum port diameter, $d_{v,max}$. The flowrate is reduced due to the dynamics viscosity of the fluid given by the Hagen-Poiseuille Law:

$$Q_{MU} = \frac{\pi r_{h,d}^4}{8\eta}\frac{P_{v,d} - P_{MU}}{l_{h,d}}, \tag{4.6}$$

where, r_h and l_h are hose radius and length downstream of the servo valve, respectively. η is the dynamic viscosity of hydraulic fluid (ISO 32) [52]. A dynamic viscosity of 0.2856 was used which was experimentally acquired measuring the flowrate and pressure differential across a given length of hose length. Given the flowrate going into a MU, the pressure dynamics are expressed as:

$$\frac{dP_{MU}}{dt} = E\frac{Q_{MU} - \dot{V}_{MU}}{V_{MU}}, \tag{4.7}$$

where, E is the bulk modulus of the hydraulic fluid, and V_{MU} is the volume inside the MU expressed as:

$$V_{MU} = 2\pi r_0^2 l_0\left[\frac{(1-\varepsilon)}{sin^2\alpha_0} - \frac{(1-\varepsilon)^3}{tan^2\alpha_0}\right]. \tag{4.8}$$

where l_0 is the initial length of the FAM.

4.3 Controller Design

Two control schemes are presented in this section. The first control scheme is the baseline controller which uses a specified percentage of the source pressure as the *threshold pressure* at which a recruitment state transition is initiated. Next, the proposed control scheme is presented by its two components: pressure compensation and lag compensation.

4.3.1 Baseline scheme: Cascaded PI-PI control using pressure thresholds for state transitions

The block diagram for the baseline controller is presented in Figure 4.3. The controller consists of a strain feedback outer PI control loop with a nested pressure feedback inner PI control loop. A cascaded PI-PI control architecture such as this one has shown to improve the tracking performance and disturbance rejection when controlling FAMs as independent actuators [11], [66]. Because the system's pressure dynamics are fast in comparison to the strain dynamics, the gains for the inner pressure controller were tuned first and treated as part of the plant while tuning the gains for the outer strain feedback controller. The pressure measurements, P_{meas}, which consists of the MU1 and MU2 pressures from the system are used to determine the recruitment state. When in RS1, the desired pressure for MU2 is simply zero. When in RS2, the same desired pressure is used to control the pressures for both MU1 and MU2, which corresponds to the batch recruitment scheme discussed in detail by Jenkins et al. [30]

The recruitment transition logic state machine for the baseline control scheme is shown in Figure 4.4. The default recruitment state is RS1 at startup. The recruitment upshift to RS2 occurs when MU1 pressure is greater than or equal to 80% of the nominal source pressure and downshifts

when MU2 pressure is less than or equal to 40% of the nominal source pressure. These shift criteria are tuned ad hoc for a particular system, load, and trajectory.

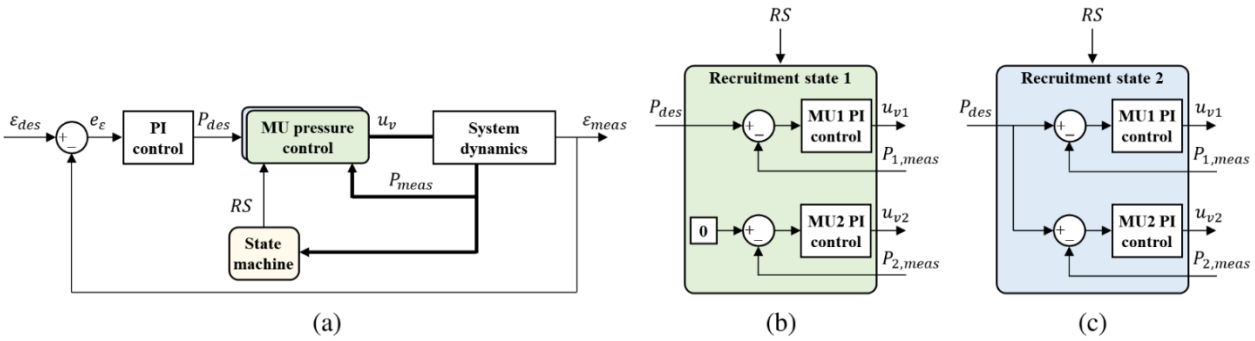

Figure 4.3: Block diagram of the baseline controller with pressure thresholds. (a) The high-level diagram showing the outer strain feedback control loop and plant. (b) The inner pressure feedback control loop that is dependent on the recruitment state. The state machine block is shown in Figure 4.4. Bold lines represent vectors with two elements corresponding to the two MUs.

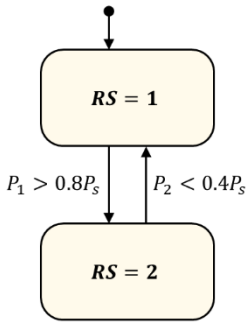

S

Figure 4.4: State machine with two MUs for the baseline controller with recruitment pressure thresholds.

4.3.2 Proposed scheme: Cascaded PI-PI control with lag and pressure compensation

The diagram for the proposed model-based controller with lag and pressure compensation is shown in Figure 4.5. On the high-level, it has the same cascaded PI-PI control architecture with the same gains as the baseline system so as to isolate the performance change due to the model-based compensation scheme. Instead of using a preset pressure threshold, recruitment state transitions are determined through *lag compensation* taking into account the dynamics of the hydraulic system. Additionally, the resistive force of MU2 before it reaches the de-slack pressure is mitigated using *pressure compensation* by an added measured pressure feedback term.

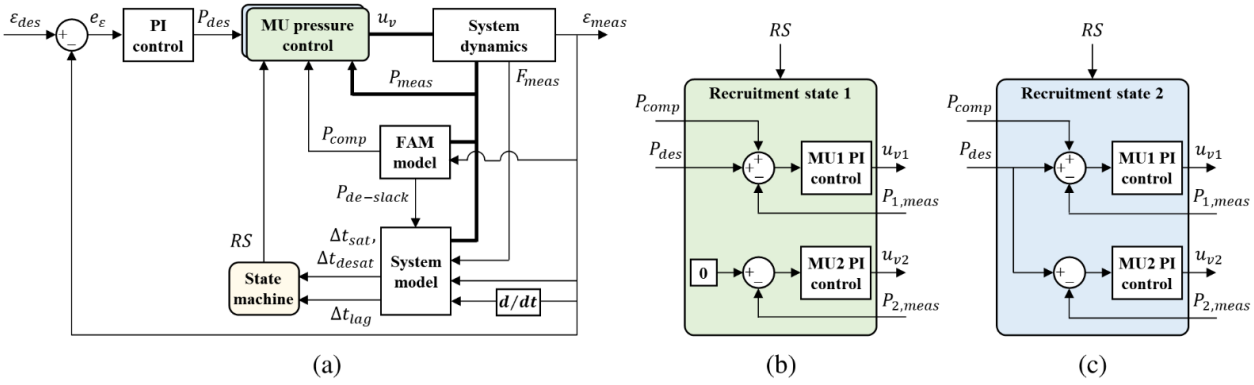

Figure 4.5: Block diagram of the proposed controller with lag and pressure compensation. (a) The high-level diagram showing the outer strain feedback control loop and plant. (b) The inner pressure feedback control loop that is dependent on the recruitment state. The state machine block is shown in Figure 4.8. Bold lines represent vectors with two elements corresponding to the two MUs.

4.3.2.1 Pressure compensation

The proposed control scheme addresses the resistive effect, aforementioned in Section 4.2, which is the effect of FAMs in compression decreasing the overall force output of a variable

recruitment bundle [21]. To counteract the resistive forces of inactive and newly-recruited FAMs in compression, the pressure of the FAMs already in the tensile region is increase by an amount of P_{comp}. First, to determine whether MU2 is in compression, the de-slack pressure is determined through a look-up table of the FAM force-strain-pressure surface that satisfies the condition:

$$F_{2,mod}(P_{de-slack}, \varepsilon_{meas}) = 0, \tag{4.9}$$

where $F_{2,mod}$ is the force of MU2 predicted by the model and ε_{meas} is the measured instantaneous strain of the bundle. It should be noted that for any MU2 pressure, P_2, below $P_{de-slack}$, the force of MU2 is negative. To compensate for the negative MU2 force when the measured pressure of MU2, $P_{2,meas}$, is less than $P_{de-slack}$, the MU1 force must increase by an amount equal to the resistive force of MU2 as:

$$\begin{aligned} F_{1,comp} &= F_{2,mod}\left(P_{2,meas}, \varepsilon_{meas}\right) \\ &= F_{1,mod}\left(P_{1,meas} + P_{comp}, \varepsilon_{meas}\right) - F_{MU1}\left(P_{1,meas}, \varepsilon_{meas}\right), \end{aligned} \tag{4.10}$$

where $F_{1,mod}$ is the force of MU1 predicted by the model, $P_{1,meas}$ is the measured pressure of MU1, and P_{comp} is the amount of additional pressure required by MU1. Thus, the predicted overall force of the bundle can be expressed by:

$$\begin{aligned} F_{bundle,mod} = F_{1,mod}&\left(P_{1,meas} + P_{comp}, \varepsilon_{meas}\right) \\ &+ F_{2,mod}\left(P_{2,meas}, \varepsilon_{meas}\right) \end{aligned} \tag{4.11}$$

where $P_{comp} = 0$ if MU2 no longer is in compression (i.e. $P_{2,meas} \geq P_{de-slack}$). At every instant of time, the P_{comp} that satisfies (4.10) is determined, fed back, and added to the desired pressure of MU1.

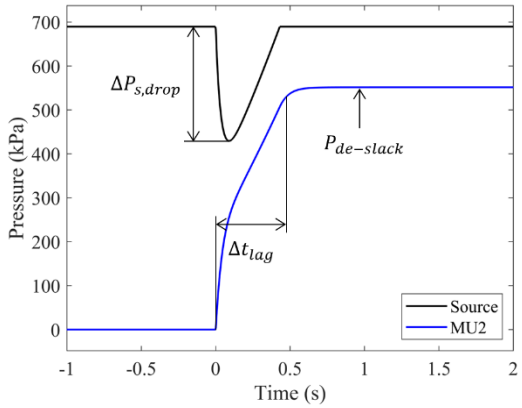

Figure 4.6: Example simulation of hydraulic system pressure dynamics for a nominal source pressure of $689.5\ kPa$ $(100\ psi)$ and a de-slack pressure of $551.6\ kPa$ $(80\ psi)$. The recruitment lag, Δt_{lag}, which is defined as the time required to reach 95% of the de-slack pressure and the maximum source pressure drop, $\Delta P_{s,drop}$, is determined.

4.3.2.2 Lag compensation

As aforementioned, the pressure dynamics of a real hydraulic system cause a lag between when the recruitment of a MU is initiated and when it reaches the de-slack pressure. This time difference is referred to as the *recruitment lag*, Δt_{lag}. The hydraulic system model from Section 4.2 is used to simulate the pressure transients as it tracks a step reference to the de-slack pressure as shown in Figure 4.6. This pressure response represents the pressure applied to a MU being newly recruited during state transition.

According to the de-slack effect, the pressure of the subsequent MU being recruited must reach the de-slack pressure before it is able to contribute any positive force or strain. Additionally, while below the de-slack pressure, the recruited MU is in a buckled state and exerting a resistive force. The recruitment lag informs the controller how much in advance the state transition must begin in order to guarantee enough time before the current MU is saturated and cannot generate

the force or strain required to track a desired reference. The determining factors of recruitment lag are the de-slack pressure, instantaneous source pressure, and the parameters of the hydraulic system. Once a simulation is run for a set of de-slack and source pressures, the time it takes for the pressure to reach 95% of the de-slack pressure is defined as the recruitment lag.

Another variable of interest is the maximum amount of source pressure drop, $\Delta P_{s,drop}$that occurs during a recruitment transition. As the MU pressure increases, the required flowrate causes the source pressure to drop. Although a PRRV is used in this study, an analogous effect is observed in any fluid power source such as a motor/pump with an accumulator. This pressure drop is used to determine the pressure margin that is required for pressure compensation to occur, expressed as:

$$P_{margin} = \Delta P_{s,drop} + P_{comp}, \tag{4.12}$$

where, both $\Delta P_{s,drop}$ and P_{comp} are instantaneous values determined online based on $P_{s,meas}$, $P_{1,meas}$, $P_{2,meas}$, and ε_{meas} measured at a given instant. The pressure margin is used to define an effective source pressure, $P_{s,eff}$ expressed as:

$$P_{s,eff} = P_{s,meas} - P_{margin}. \tag{4.13}$$

Note that the pressures applied to MUs are always limited by source pressure. The pressure margin ensures that MU1 does not become saturated by the source pressure while pressure compensation is happening. In order to reduce computation during real-time control, the recruitment lag and source pressure drop are computed for the range of possible source pressures and de-slack pressures to generate a lookup table.

Once the lag associated with recruiting MU2 is determined, the time difference between the current time and when the MU1 would become saturated during upshift is estimated. This time difference is defined as the *time-to-saturation.* During downshift, the *time-to-desaturation* is

defined as the time difference between the current time and when MU2 would no longer be required. At every instant of time, it is assumed

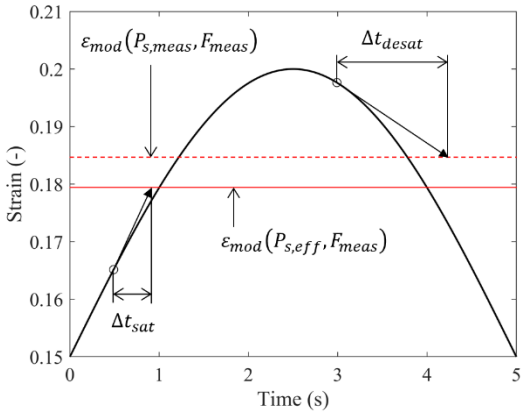

Figure 4.7: Example determination of time-to-saturation, Δt_{sat}, time-to-desaturation, Δt_{desat}.

that the bundle will continue to contract in the same direction with constant rate of contraction as illustrated in Figure 4.7. The expected strain trajectory, $E(t)$, is expressed as:

$$E(t) = \dot{\varepsilon}_{meas} t + \varepsilon_{meas} \tag{4.14}$$

where, ε_{meas} is the measured instantaneous strain. Rearranging and solving for Δt_{sat} by setting (4.14) equal to the strain at $P_{s,eff}$ and the measured instantaneous force, F_{meas}, gives us the equation for time-to-saturation and time-to-desaturation as:

$$\Delta t_{sat} = \frac{\varepsilon_{mod}(P_{s,eff},\ F_{meas}) - \varepsilon_{meas}}{\dot{\varepsilon}_{meas}}, \tag{4.15}$$

and

$$\Delta t_{desat} = \frac{\varepsilon_{mod}(P_{s,meas},\ F_{meas}) - \varepsilon_{meas}}{\dot{\varepsilon}_{meas}}. \tag{4.16}$$

where ε_{mod} is the bundle strain predicted by the model. Note that $E(t)$ can be generalized to other forms of expected trajectories such as a sinusoid instead of the linear assumption used in this study. This would be useful if some knowledge about the control application was given in advance.

For the proposed model-based control scheme, the state transition decision is made through time-to-saturation, time-to-desaturation, and recruitment lag conditions as shown in Figure 4.8. Note that the recruitment lag is an estimation of the time it takes for a newly-recruited MU to de-slack and begin to positively contribute to overall bundle output. The time-to-saturation is an estimate of how long in advance the bundle will require the newly-recruited MU to provide additional force. Thus, the state transition must occur when the time-to-saturation is less than or equal to the recruitment lag in order to ensure that the bundle is provided with the force of the newly-recruited MU in time. Note that, from an efficiency perspective, it is advantageous for a variable recruitment bundle to operate at the lowest recruitment state possible. This allows the applied pressures to the activated MUs to be closest to the source pressure, thus allowing the bundle to operate more efficiently by minimizing throttling energy losses. However, higher recruitment states provide better control authority. Therefore, properly deciding when to initiate a recruitment state transition is important for operating a variable recruitment bundle efficiently and with satisfactory tracking performance. The lag compensation method proposed in this study provides an online method of estimating that time based on information from the model and the measured states.

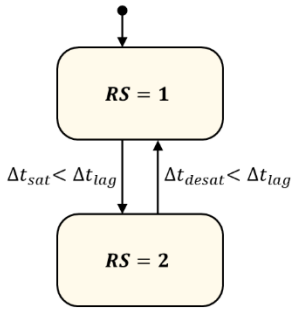

Figure 4.8: State machine with two MUs for the proposed controller using lag compensation to shift between states.

Table 4.1: FAM dimensions and specifications.

FAM dimensions	Initial inner radius (m)	r_0	0.0063
	Initial thickness (m)	t_0	0.0016
	Initial braid angle $(°)$	α_0	33
	Initial length (m)	L_0	0.222
Empirical-based tuning correction factors	Young's modulus	-	1.3
	Collapse moment	-	0.75
	Torsional spring constant	-	0.9P + 1.54
	Transition constant	β	100

4.4 Experiment setup

FAMs are constructed using silicone tubing with a Shore hardness value of A50 and a double-helix braided Kevlar mesh. A neoprene spacer is placed over the mesh at each end and crimped using a hydraulic press. The FAM assembly method is identical to that of detailed in Meller et al. 2014 [31]. FAM dimensions and specifications are summarized in Table 4.1. The force-strain relationship is then corrected using empirical-based correction factors for which the details can be found in [21]. Experiments were carried out on the linear hydraulic actuator

characterization device (LHACD) shown in Figure 4.9 which was developed in-house by Chipka et al. in 2017 [23]. The LHACD consists of a $3.73\ kW(5\ hp)$ hydraulic power unit (Concentric GC9500) capable of producing pressures up to $1.03 \times 10^4\ kPa\ (1500\ psi)$ at a rated flow of $3.78\ m^3/s\ (6\ gpm)$. A pressure reducing/relief valve (PRRV) from Sun Hydraulics (PRDV-LEV) is used to regulate the downstream circuit nominal source pressure down to $689.5\ kPa\ (100\ psi)$ for the safe operation of FAMs without rupturing. The regulated pressure output of a PRRV is dependent on the rate of fluid flow through the valve which is provided by the manufacturer for several values of operating pressure. For a source pressure of $689.5\ kPa\ (100\ psi)$, the pressure-flowrate relationship is experimentally determined for which the results are shown in Figure 4.10. It should be noted that for cases when the pressure output of the PRRV exceeds the set value of $6.89.5\ kPa\ (100\ psi)$, its relieving function is engaged and fluid is directed to the reservoir instead of the downstream circuit. Located downstream of the PRRV are two four-way directional servo valves (MOOG G761) that are used to control the pressures of the two MUs. Pressure transducers (TE MP300) are installed to measure the source pressure and the two pressures downstream of each servo valve. A flowmeter (Omega FPD2003) is installed to measure the flowrate of the PRRV output. A linear variable differential transducer (LVDT) by RDP group (DR7AC) is used to measure the contraction of the FAM bundle. Lastly, servo valve control and data acquisition are performed using a Quanser QPID I/O board.

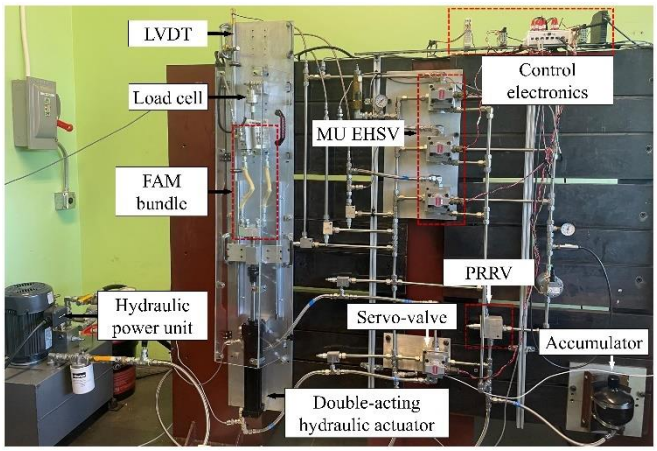

Figure 4.9: The linear hydraulic actuator characterization device (LHACD) used for experiments in this study.

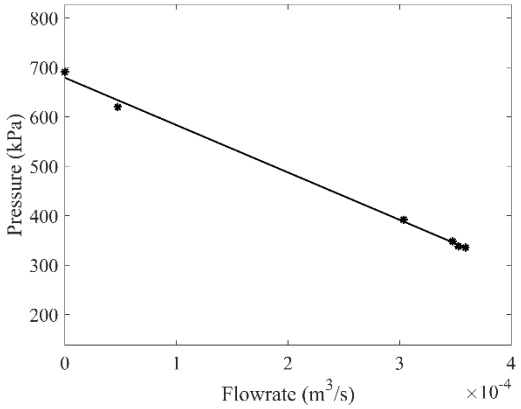

Figure 4.10: Pressure-flowrate relationship of the PRRV. Measured values are indicated in black markers. The linear line fit used for simulations is shown in solid black line.

4.5 Results

The performance of the baseline controller with state transitions based on pressure thresholds (Figure 4.11), controller with lag compensation only (Figure 4.12), and controller with both lag and pressure compensation (Figure 4.13) are presented in this section. For all control

scheme cases, a sinusoidal reference trajectory with a frequency of 0.1 Hz and a strain amplitude of 0.06 is specified. A mass of 18.8 kg was hung from the bottom of the FAM bundle.

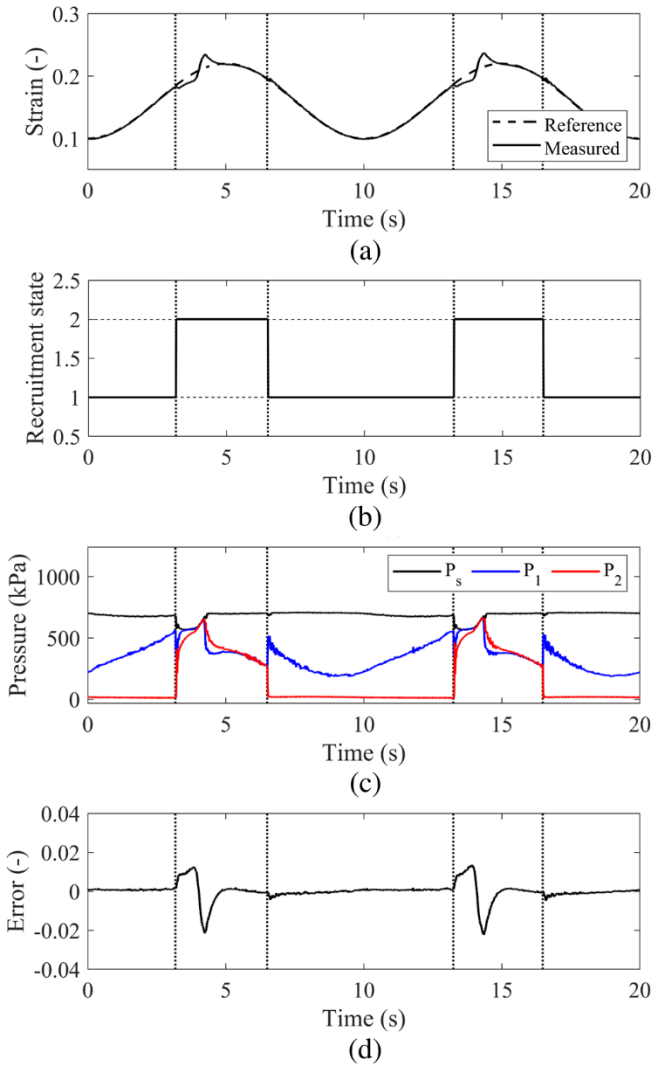

Figure 4.11: Experimental results of cascaded controller with state transitions using pressure thresholds. (a) Position tracking; (b) recruitment state; (c) pressures for source, MU1, and MU2; (d) strain tracking error.

For the system with the baseline controller, the position tracking performance is shown in Figure 4.11(a). The source pressure and the pressures applied to MU1 and MU2 are shown in

Figure 4.11(c). According to the state machine shown in Figure 4.5 the upshift to recruitment state 2 is made once MU1 pressure reaches 551.6 kPa (80 psi) which is 80% of the nominal source pressure. Recruitment state is shifted down at 40% of the nominal source pressure. The recruitment shift is depicted in all subfigures as a vertical dashed line. Immediately after state upshift, the strain lags further behind the reference strain which results in the overshoot as the controller attempts to compensate for the error due to lag. The lag is mainly attributed to the saturation of MU1 pressure as only pressures as high as the instantaneous source pressure can be applied to the MUs. As expected from simulation predictions (e.g. Figure 4.6), the recruitment of MU2 causes a drop in source that further limits the MU1 pressure.

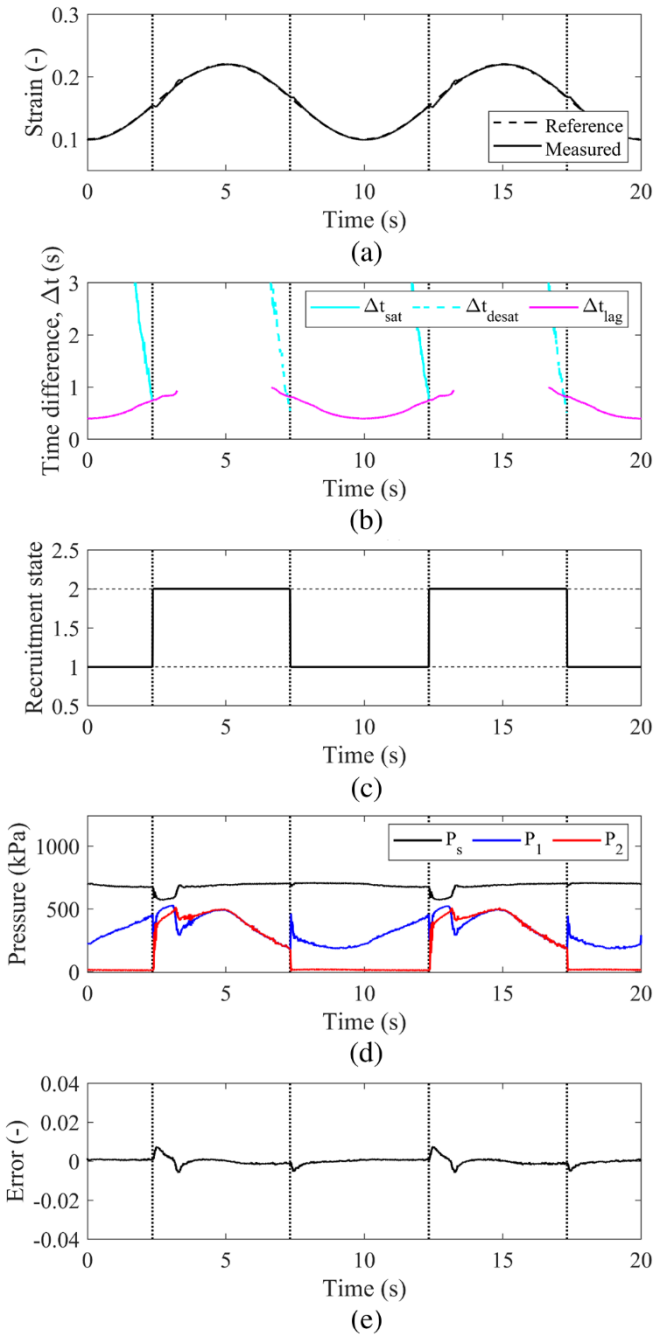

Figure 4.12: Experimental results of cascaded controller with state transitions with lag compensation applied. (a) Position tracking; (b) time-to-saturation, time-to-desaturation, and recruitment lag; (c) recruitment state; (d) pressures for source, MU1, and MU2; (e) strain tracking error.

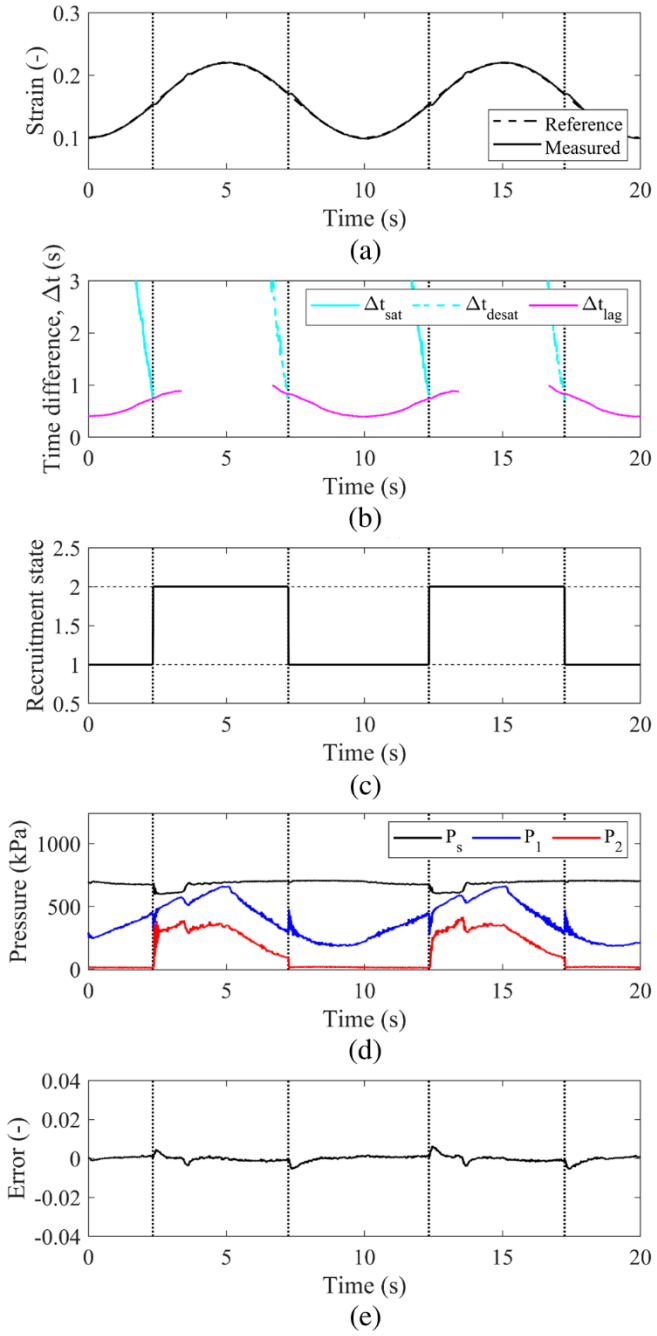

Figure 4.13: Experimental results of cascaded controller with state transitions with lag compensation and pressure compensation applied. (a) Position tracking; (b) time-to-saturation, time-to-desaturation, and recruitment lag; (c) recruitment state; (d) pressures for source, MU1, and MU2; (e) strain tracking error.

The experiment results for the controller with lag compensation applied is shown in Figure 4.12. The time-to-saturation, time-to-desaturation, and the recruitment lag are determined at every instant of time as shown in Figure 4.12 (b). As the bundle strain tracks the reference, the time-to-saturation decreases as the bundle gets closer to the time at which the recruitment state transition must occur. Simultaneously, the recruitment lag, according to the instantaneous source pressure and de-slack pressure of MU2, increases with increasing strain. The time at which recruitment state transition occurs is determined when the time-to-saturation drops below the recruitment lag as demonstrated by Figure 4.12 (b) and (c). As a result, the state upshift occurs earlier compared to the baseline controller case, thus allowing the necessary pressure of MU1 to be applied without being saturated as shown in Figure 4.12 (d). Consequently, the strain lag immediately following a state transition is significantly reduced. The argument can be made that the same effect can be achieved by lowering the pressure threshold of the baseline case. However, a certain pressure threshold is effective only for a trajectory with a specific range of amplitudes and frequencies, and thus, is only useful if the reference trajectory is known in advance. Additionally, the pressure threshold may need to be determined empirically. By determining the time-to-saturation and recruitment lag based on the instantaneous measured states during control, the proposed controller provides an online method of determining when the state transition must occur real-time.

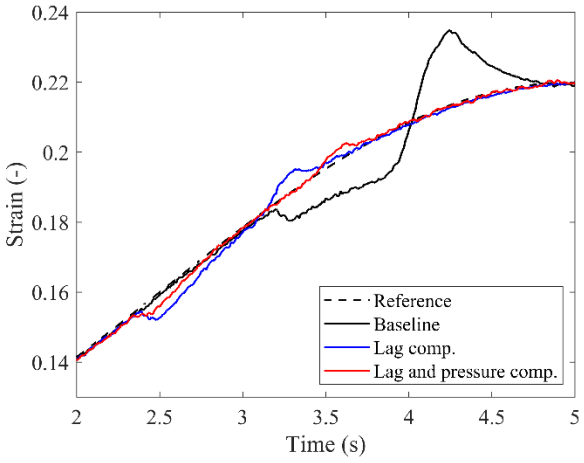

Figure 4.14: Reference and measured strain immediately following recruitment state transition of baseline and proposed controllers.

The tracking performance can be further increased by applying pressure compensation in addition to lag compensation as shown in Figure 4.13. The pressure feedback term provides anticipatory information on what the pressure of MU1 should be based on the resistive force of MU2. The state transition occurs based on lag compensation. The effect of pressure compensation is evident in MU1 pressure after the state shift as shown by Figure 4.13 (d). The improved tracking performance is better demonstrated by a zoomed-in view of the measured strains for all cases in Figure 4.14. The integral absolute error (IAE) for strain for one cycle and the maximum strain error is determined by:

$$IAE_{\varepsilon} = \int |\varepsilon_{ref} - \varepsilon_{meas}| dt, \tag{4.17}$$

where ε_{ref} is the reference strain and ε_{meas} is the measured strain. The maximum strain error, $err_{\varepsilon,max}$, is expressed as:

$$err_{\varepsilon,max} = max(|\varepsilon_{ref} - \varepsilon_{meas}|). \tag{4.18}$$

A comparison of these values is shown in Table 4.2.

Table 4.2: Comparison of integral absolute error (IAE) for strain, and maximum strain error.

	Strain IAE	Max. strain error
Baseline scheme	0.0454	0.0223
Proposed scheme with only lag compensation	0.0234	0.0075
Proposed scheme with lag and pressure compensation	0.0211	0.0064

4.6 Conclusion

This study experimentally evaluates the tracking performance of a model-based controller for state transitions of a variable recruitment FAM bundle. During variable recruitment operation, inactive/low-pressure FAMs are buckled and exert resistive forces that decrease the overall force of the bundle. This resistive effect is captured using a FAM model that predicts the axial force of FAMs beyond their free strain. A pressure feedback term is used to compensate for the decrease in force. Additionally, a hydraulic dynamics system model is used to predict the time required for a newly-recruited MU that is buckled to de-slack, coined the recruitment lag. The measured strain, strain rate, pressure, and force are used to predict the time-to-saturation and time-to-desaturation. These two variables in tandem inform the control when to initiate a state transition. The proposed controller is compared to a baseline for which a pressure threshold based on a percentage of the nominal source pressure is used to initiate state transitions. A sinusoidal strain trajectory is tracked, and the measured strain is presented, along with the source pressure and MU1 and MU2 pressures.

The controller showed its ability to determine the state transitions timing so that MU1 pressure is not saturated when the next MU is newly-recruited. The IAE and maximum strain errors are presented to show the improved tracking performance of the proposed controller. For the purposes of this study, the linear estimation methods used in lag compensation were sufficient. If more advanced estimation methods could be applied, the proposed control scheme has the potential to be used for complex non-cyclic trajectories. Another area for future investigation is the correlation between state transition timings and actuator hydraulic efficiencies.

CHAPTER 5

Key Research Contributions and Suggested Future Investigations

5.1 Modeling of resistive forces and buckling behavior in variable recruitment fluidic artificial muscle bundles

This section enumerates contributions and potential future work for material in Chapter 2.

5.1.1 Contributions

- A FAM model that predicts the negative forces of a FAM beyond its free strain was derived. The negative force has been coined the resistive forces, which has been further categorized into the post-buckled and post-collapsed regions.
- The implications of resistive forces on the force-strain space of a variable recruitment bundle were presented to demonstrate an overlapping region between consecutive recruitment states that had been present using previous models.
- Empirical-based correction factors were developed to better improve the model's match with experimental data.
- A phenomenon called the free strain gradient reversal was revealed that shows the overall force of a variable recruitment bundle initially decreases due to low-pressure MUs.

5.1.2 Future investigations

Future work should address the sensitivity of forces in the compressed region to FAM dimensions such as bladder thickness or FAM slenderness ratio. Future modeling efforts should focus on refining the effects of the hyperelasticity of the inner bladder and density of the braided mesh. This model does not address the effect of friction between the mesh and bladder and thus neglects any hysteresis of the FAM during actuation. Further investigations to include such effects into the model will be able to achieve better matching with experimental data.

5.2 Electrohydraulic system analysis of variable recruitment fluidic artificial muscle bundles with interaction effects

This section enumerates contributions and potential future work for material in Chapter 3.

5.2.1 Contributions

- An analytical study of volume and pressure requirements during recruitment state transition based on a model that captures FAM buckling behavior and resistive effects was conducted to demonstrate the limit of practical electrohydraulic systems due to pressure dynamics.
- Developed a recruitment state transition strategy considering resistive and de-slack effects of inactive/low-pressure motor units considering system dynamics.
- Perform a system-level analysis for a variable recruitment FAM bundle model including inter-FAM effects under a variable pump displacement operating condition to reveal significant increases in overall efficiencies and bandwidth limit.

5.2.2 Future investigations

Understanding system efficiency and bandwidth limits are crucial in developing any robotic application in which variable recruitment is applied. Future system level analyses should focus on experimental validation of the overall efficiency and bandwidth advantages of applying variable recruitment. Additional electrohydraulic circuit topologies can be investigated such as the use of ORVs which would lower circuit complexity.

5.3 Model-based control allocation during state transitions of a variable recruitment fluidic artificial muscle bundle

This section enumerates contributions and potential future work for material in Chapter 4.

5.3.1 Contributions

- A model-based cascaded PI-PI control scheme with model-based lag and pressure compensations was developed and tested on the LHACD.
- The lag associated with system dynamics during state transitions has been coined the recruitment lag. Furthermore, an anticipatory method of estimating the time-to-saturation and time-to-desaturation is developed, which are used, in tandem with recruitment lag, to determine the state transition timing online.
- A pressure compensation method of using the pressure of the previously-recruited MU.to compensate for the resistive forces of newly-recruited MU below its de-slack pressure is developed and tested to show significant increases in the IAE and maximum errors.

5.3.2 Future investigations

The tracking performance of the proposed control scheme has been evaluated compared to a baseline control scheme that uses a state shift pressure threshold. Although the proposed control scheme performs better in terms of reducing tracking error, transition timings and its effect on hydraulic efficiency have not been evaluated. Furthermore, the proposed control scheme has the potential to be applied to complex strain trajectories.

5.4 Final conclusions

This study begins by modeling the buckling phenomenon of FAMs within a variable recruitment bundle. From the developed model that captures these resistive forces of FAMs, this study expands its scope by exploring the system-level dynamics and its control through simulation and experiments. The potential for variable recruitment of FAM bundles will continue to grow with further insights and research advancements.

REFERENCES

[1] B. Tondu, “Modelling of the McKibben artificial muscle: A review,” *J. Intell. Mater. Syst. Struct.*, vol. 23, no. 3, pp. 225–253, 2012, doi: 10.1177/1045389X11435435.

[2] J. Garbulinski, S. C. Balasankula, and N. M. Wereley, “Characterization and analysis of extensile fluidic artificial muscles,” *Actuators*, vol. 10, no. 2, pp. 1–26, 2021, doi: 10.3390/act10020026.

[3] H. Al-Fahaam, S. Davis, and S. Nefti-Meziani, “The design and mathematical modelling of novel extensor bending pneumatic artificial muscles (EBPAMs) for soft exoskeletons,” *Rob. Auton. Syst.*, vol. 99, pp. 63–74, 2018, doi: 10.1016/j.robot.2017.10.010.

[4] P. Ohta *et al.*, “Design of a Lightweight Soft Robotic Arm Using Pneumatic Artificial Muscles and Inflatable Sleeves,” *Soft Robot.*, vol. 5, no. 2, pp. 204–215, 2018, doi: 10.1089/soro.2017.0044.

[5] T. Park, K. Kim, S. R. Oh, and Y. Cha, “Electrohydraulic Actuator for a Soft Gripper,” *Soft Robot.*, vol. 7, no. 1, pp. 68–75, 2020, doi: 10.1089/soro.2019.0009.

[6] L. Qin, X. Liang, H. Huang, C. K. Chui, R. C. H. Yeow, and J. Zhu, “A Versatile Soft Crawling Robot with Rapid Locomotion,” *Soft Robot.*, vol. 6, no. 4, pp. 455–467, 2019, doi: 10.1089/soro.2018.0124.

[7] T. Jenkins and M. Bryant, “Pennate actuators: Force, contraction and stiffness,” *Bioinspiration and Biomimetics*, vol. 15, no. 4, 2020, doi: 10.1088/1748-3190/ab860f.

[8] E. Duan and M. Bryant, “Implications of Spatially Constrained Bipennate Topology on Fluidic Artificial Muscle Bundle Actuation,” *Actuators*, vol. 11, no. 3, 2022, doi: 10.3390/act11030082.

[9] M. Bryant, M. A. Meller, and E. Garcia, “Variable recruitment fluidic artificial muscles: Modeling and experiments,” *Smart Mater. Struct.*, vol. 23, no. 7, 2014, doi: 10.1088/0964-1726/23/7/074009.

[10] S. A. Delahunt, T. E. Pillsbury, and N. M. Wereley, “Variable recruitment in bundles of miniature pneumatic artificial muscles,” *Bioinspiration and Biomimetics*, vol. 11, no. 5, 2016, doi: 10.1088/1748-3190/11/5/056014.

[11] R. M. Robinson, C. S. Kothera, and N. M. Wereley, “Variable Recruitment Testing of Pneumatic Artificial Muscles for Robotic Manipulators,” *IEEE/ASME Trans. Mechatronics*, vol. 20, no. 4, pp. 1642–1652, 2015.

[12] E. Henneman, G. Somjen, and D. O. Carpenter, “Excitability and inhibitibility of motoneurons of different sizes,” *J. Neurophysiol.*, vol. 28, no. 3, 1965, doi: 10.1152/jn.1965.28.3.599.

[13] E. M. Chapman, T. Jenkins, and M. Bryant, “Design and analysis of electrohydraulic pressure systems for variable recruitment in fluidic artificial muscles,” *Smart Mater. Struct.*, vol. 27, no. 10, p. 105024, 2018, doi: 10.1088/1361-665X/aadbff.

[14] B. Tondu and P. Lopez, “Modelling and Control of McKibben Artificial Muscle Robot Actuators,” *Control Syst.*, vol. 20, no. 2, pp. 15–38, 2000, doi: 10.1109/37.833638.

[15] C. S. Kothera, M. Jangid, J. Sirohi, and N. M. Wereley, “Experimental characterization and static modeling of McKibben actuators,” *J. Mech. Des. Trans. ASME*, vol. 131, no. 9, pp. 0910101–09101010, 2009, doi: 10.1115/1.3158982.

[16] E. Ball and E. Garcia, “Effects of bladder geometry in pneumatic artificial muscles,” *J. Med. Devices, Trans. ASME*, vol. 10, no. 4, pp. 1–11, 2016, doi: 10.1115/1.4033325.

[17] Z. Yu, T. Pillsbury, G. Wang, and N. M. Wereley, “Hyperelastic analysis of pneumatic arti fi cial muscle with fi lament-wound sleeve and coated outer layer,” *Smart Mater. Struct.*, vol. 28, no. 10, p. 105019, 2019, doi: 10.1088/1361-665X/ab300d.

[18] K. G. and H. B., “Accounting for Elastic Energy Storage in McKibben Artificial Muscle Actuators,” *J. Dyn. Sys., Meas., Control*, vol. 122, no. 2, pp. 386–388, 1998, doi: 10.1260/0957456991496565.

[19] C. P. Chou and B. Hannaford, “Measurement and modeling of McKibben pneumatic artificial muscles,” *IEEE Trans. Robot. Autom.*, vol. 12, no. 1, pp. 90–102, 1996, doi: 10.1109/70.481753.

[20] J. Y. Kim, N. Mazzoleni, and M. Bryant, “Investigation of Resistive Forces in Variable Recruitment Fluidic Artificial Muscle Bundles,” *Conf. Proc. Soc. Exp. Mech. Ser.*, vol. 8, 2020, doi: 10.1007/978-3-030-47717-2_32.

[21] J. Y. Kim, N. Mazzoleni, and M. Bryant, “Modeling of Resistive Forces and Buckling Behavior in Variable Recruitment Fluidic Artificial Muscle Bundles,” *Actuators*, vol. 10, no. 3, p. 42, 2021, doi: 10.3390/act10030042.

[22] M. Meller, J. Chipka, A. Volkov, M. Bryant, and E. Garcia, “Improving actuation efficiency through variable recruitment hydraulic McKibben muscles: Modeling, orderly recruitment control, and experiments,” *Bioinspiration and Biomimetics*, vol. 11, no. 6, 2016, doi: 10.1088/1748-3190/11/6/065004.

[23] J. Chipka, M. A. Meller, A. Volkov, M. Bryant, and E. Garcia, “Linear dynamometer testing of hydraulic artificial muscles with variable recruitment,” *J. Intell. Mater. Syst. Struct.*, vol. 28, no. 15, pp. 2051–2063, 2017, doi: 10.1177/1045389X16682845.

[24] B. Tondu, S. Ippolito, J. Guiochet, and A. Daidie, “A Seven-degrees-of-freedom robot-arm driven by pneumatic artificial muscles for humanoid robots,” *Int. J. Rob. Res.*, vol. 24, no. 4, pp. 257–274, 2005, doi: 10.1177/0278364905052437.

[25] K. E. Gordon, G. S. Sawicki, and D. P. Ferris, “Mechanical performance of artificial pneumatic muscles to power an ankle-foot orthosis,” *J. Biomech.*, vol. 39, no. 10, pp. 1832–1841, 2006, doi: 10.1016/j.jbiomech.2005.05.018.

[26] M. Mori *et al.*, “Development of power robot hand with shape adaptability using hydraulic McKibben muscles,” *Proc. - IEEE Int. Conf. Robot. Autom.*, pp. 1162–1168, 2010, doi: 10.1109/ROBOT.2010.5509489.

[27] E. M. Chapman, T. E. Jenkins, and M. Bryant, “Modeling and analysis of a meso-hydraulic climbing robot with artificial muscle actuation,” *Bioinspiration and Biomimetics*, vol. 12, no. 6, 2017, doi: 10.1088/1748-3190/aa7eb0.

[28] S. Kurumaya, H. Nabae, G. Endo, and K. Suzumori, “Exoskeleton inflatable robotic arm with thin McKibben muscle,” *2018 IEEE Int. Conf. Soft Robot. RoboSoft 2018*, pp. 120–125, 2018, doi: 10.1109/ROBOSOFT.2018.8404907.

[29] P. T. Phan, T. T. Hoang, M. T. Thai, H. Low, N. H. Lovell, and T. N. Do, “Twisting and Braiding Fluid-Driven Soft Artificial Muscle Fibers for Robotic Applications,” *Soft Robot.*, vol. 9, no. 4, pp. 820–836, 2022, doi: 10.1089/soro.2021.0040.

[30] T. E. Jenkins, E. M. Chapman, and M. Bryant, “Bio-inspired online variable recruitment control of fluidic artificial muscles,” *Smart Mater. Struct.*, vol. 25, no. 12, 2016, doi: 10.1088/0964-1726/25/12/125016.

[31] M. A. Meller, M. Bryant, and E. Garcia, “Reconsidering the McKibben muscle: Energetics, operating fluid, and bladder material,” *J. Intell. Mater. Syst. Struct.*, vol. 25, no. 18, pp. 2276–2293, 2014, doi: 10.1177/1045389X14549872.

[32] R. M. Jones, *Buckling of Bars, Plates, and Shells*. Blacksburg, VA, USA: Bull Ridge Publishing, 2006.

[33] G. Simitses, “Buckling and postbuckling of imperfect cylindrical shells under external pressure,” *Thin-Walled Struct.*, vol. 39, no. 10, pp. 1517–1524, 1986, doi: 10.1115/1.3149506.

[34] L. G. Brazier, P. Character, and N. Sep, “On the Flexure of Thin Cylindrical Shells and Other " Thin " Sections,” *Proc. R. Soc. London . Ser. A*, vol. 116, no. 773, pp. 104–114, 1927.

[35] S. B. Krenk, *In Mechanics and Analysis of Beams, Columns and Cables*, 2nd ed. Berlin/Heidelberg, Germany: Springer-Verlag, 2001.

[36] J. D. Wood, “The flexure of a uniformly pressurized, circular, cylindrical shell,” *J. Appl. Mech.*, vol. 25, pp. 453–458, 1958.

[37] M. Stein and J. M. Hedgpeth, “Analysis of Partly Wrinkled Membranes,” Washington,

Dc, USA, 1961.

[38] G. W. Zender, “The Bending Strength of Pressurized Cylinders,” *J. Aerosp. Sci.*, vol. 29, pp. 362–363, 1961.

[39] S. L. Veldman, O. K. Bergsma, and A. Beukers, “Bending of anisotropic inflated cylindrical beams,” *Thin-Walled Struct.*, vol. 43, pp. 461–475, 2005.

[40] S. Kurumaya, H. Nabae, G. Endo, and K. Suzumori, “Design of thin McKibben muscle and multifilament structure,” *Sensors Actuators, A Phys.*, vol. 261, pp. 66–74, 2017, doi: 10.1016/j.sna.2017.04.047.

[41] M. Meller, B. Kogan, M. Bryant, and E. Garcia, “Model-based feedforward and cascade control of hydraulic McKibben muscles,” *Sensors Actuators, A Phys.*, vol. 275, pp. 88–98, 2018, doi: 10.1016/j.sna.2018.03.036.

[42] C. Wielsgosz and J. C. Thomas, “Deflections of inflatable fabric panels at high pressure,” *Thin-Walled Struct.*, vol. 40, no. 523–536, 2002, doi: 10.1016/S0263-8231(02)00010-1.

[43] W. B. Stephans, J. H. Starnes, and B. O. Almroth, “Collapse of Long Cylindrical Shells under Combined Bending and Pressure Loads,” *AIAA J.*, vol. 13, pp. 20–25, 1975, doi: 10.2514/3.49624.

[44] J. Diani, B. Fayolle, and P. Gilormini, “A review on the Mullins effect,” *Eur. Polym. J.*, vol. 45, pp. 601–612, 2009, doi: 10.1016/j.eurpolymj.2008.11.017.

[45] M. F. Cullinan, E. Bourke, K. Kelly, and C. McGinn, “A mckibben type sleeve pneumatic muscle and integrated mechanism for improved stroke length,” *J. Mech. Robot.*, vol. 9, no. 1, pp. 1–9, 2017, doi: 10.1115/1.4035496.

[46] S. Kurumaya, K. Suzumori, H. Nabae, and S. Wakimoto, “Musculoskeletal lower-limb robot driven by multifilament muscles,” *ROBOMECH J.*, vol. 3, no. 1, pp. 1–15, 2016, doi: 10.1186/s40648-016-0061-3.

[47] D. Vemula, J. Y. Kim, N. Mazzoleni, and M. Bryant, “Design, analysis, and validation of an orderly recruitment valve for bio-inspired fluidic artificial muscles,” *Bioinspiration and Biomimetics*, vol. 17, no. 2, 2022, doi: 10.1088/1748-3190/ac4381.

[48] E. M. Chapman and M. Bryant, “Bioinspired passive variable recruitment of fluidic artificial muscles,” *J. Intell. Mater. Syst. Struct.*, vol. 29, no. 15, pp. 3067–3081, 2018, doi: 10.1177/1045389X18783070.

[49] D. Sangian, S. Naficy, G. M. Spinks, and B. Tondu, “The effect of geometry and material properties on the performance of a small hydraulic McKibben muscle system,” *Sensors Actuators A. Phys.*, vol. 234, pp. 150–157, 2015, doi: 10.1016/j.sna.2015.08.025.

[50] N. Mazzoleni, J. Y. Kim, and M. Bryant, “Motor unit buckling in variable recruitment fluidic artificial muscle bundles: implications and mitigations,” *Smart Mater. Struct.*, vol. 31, no. 3, 2022, doi: 10.1088/1361-665X/ac49d9.

[51] N. D. Manring and R. C. Fales, *Hydraulic Control Systems*. John Wiley and Sons, 2019.

[52] M. Jelali and A. Kroll, *Hydraulic Servo-systems: Modeling, Identification and Control*. London: Springer-Verlag, 2003.

[53] J. J. Craig, *Introduction to Robotics: Mechanics and Control*. Upper Saddle River, MJ: Pearson Prentice Hall, 2005.

[54] M. Meller, J. Chipka, A. Volkov, M. Bryant, and E. Garcia, “Improving actuation efficiency through variable recruitment hydraulic McKibben muscles: modeling, orderly recruitment control, and experiments,” *Bioinspiration and Biomimetics*, vol. 11, pp. 1–17, 2016.

[55] W. Xiao, D. Hu, W. Chen, G. Yang, and X. Han, “Modeling and analysis of bending pneumatic artificial muscle with multi-degree of freedom,” *Smart Mater. Struct.*, vol. 30, no. 9, 2021, doi: 10.1088/1361-665X/ac1939.

[56] J. Zou *et al.*, “Muscle-fiber array inspired, multiple-mode, pneumatic artificial muscles through planar design and one-step rolling fabrication,” *Natl. Sci. Rev.*, vol. 8, no. 10, 2021, doi: 10.1093/nsr/nwab048.

[57] J. Wirekoh, L. Valle, N. Pol, and Y. L. Park, “Sensorized, Flat, Pneumatic Artificial Muscle Embedded with Biomimetic Microfluidic Sensors for Proprioceptive Feedback,” *Soft Robot.*, vol. 6, no. 6, pp. 768–777, 2019, doi: 10.1089/soro.2018.0110.

[58] H. D. Yang, B. T. Greczek, and A. T. Asbeck, “Modeling and analysis of a high-displacement pneumatic artificial muscle with integrated sensing,” *Front. Robot. AI*, vol. 6, no. JAN, pp. 1–13, 2019, doi: 10.3389/frobt.2018.00136.

[59] L. O. Tiziani and F. L. Hammond, “Optical Sensor-Embedded Pneumatic Artificial Muscle for Position and Force Estimation,” *Soft Robot.*, vol. 7, no. 4, pp. 462–477, 2020, doi: 10.1089/soro.2019.0019.

[60] J. Legrand, B. Loenders, A. Vos, L. Schoevaerdts, and E. Vander Poorten, “Integrated Capacitance Sensing for Miniature Artificial Muscle Actuators,” *IEEE Sens. J.*, vol. 20, no. 3, pp. 1363–1372, 2020.

[61] G. Andrikopoulos, G. Nikolakopoulos, and S. Manesis, “A Survey on applications of Pneumatic Artificial Muscles,” *2011 19th Mediterr. Conf. Control Autom. MED 2011*, pp. 1439–1446, 2011, doi: 10.1109/MED.2011.5982983.

[62] K. Ogawa, C. Thakur, T. Ikeda, T. Tsuji, and Y. Kurita, “Development of a pneumatic

artificial muscle driven by low pressure and its application to the unplugged powered suit," *Adv. Robot.*, vol. 31, no. 21, pp. 1135–1143, 2017, doi: 10.1080/01691864.2017.1392345.

[63] M. V. Pawar, "Experimental Modelling of Pneumatic Artificial Muscle Systems Designing of Prosthetic Robotic Arm," *2018 3rd Int. Conf. Converg. Technol. I2CT 2018*, pp. 18–23, 2018, doi: 10.1109/I2CT.2018.8529453.

[64] H. S. Choi, C. H. Lee, and Y. S. Baek, "Design and Validation of a Two-Degree-of-Freedom Powered Ankle-Foot Orthosis with Two Pneumatic Artificial Muscles," *Mechatronics*, vol. 72, no. September, p. 102469, 2020, doi: 10.1016/j.mechatronics.2020.102469.

[65] M. Focchi *et al.*, "Water/air performance analysis of a fluidic muscle," *IEEE/RSJ 2010 Int. Conf. Intell. Robot. Syst. IROS 2010 - Conf. Proc.*, pp. 2194–2199, 2010, doi: 10.1109/IROS.2010.5650432.

[66] T. V. Minh, T. Tjahjowidodo, H. Ramon, and H. Van Brussel, "Cascade position control of a single pneumatic artificial muscle-mass system with hysteresis compensation," *Mechatronics*, vol. 20, no. 3, pp. 402–414, 2010, doi: 10.1016/j.mechatronics.2010.03.001.

[67] S. Ganguly, A. Garg, A. Pasricha, and S. K. Dwivedy, "Control of pneumatic artificial muscle system through experimental modelling," *Mechatronics*, vol. 22, no. 8, pp. 1135–1147, 2012, doi: 10.1016/j.mechatronics.2012.09.010.

[68] D. X. Ba, T. Q. Dinh, and K. K. Ahn, "An Integrated Intelligent Nonlinear Control Method for a Pneumatic Artificial Muscle," *IEEE/ASME Trans. Mechatronics*, vol. 21, no. 4, pp. 1835–1845, 2016, doi: 10.1109/TMECH.2016.2558292.

[69] Z. Zhang and M. Philen, "Pressurized artificial muscles," *J. Intell. Mater. Syst. Struct.*, vol. 23, no. 3, pp. 255–268, 2012, doi: 10.1177/1045389X11420592.

[70] Q. Ai *et al.*, "High-Order Model-Free Adaptive Iterative Learning Control of Pneumatic Artificial Muscle with Enhanced Convergence," *IEEE Trans. Ind. Electron.*, vol. 67, no. 11, pp. 9548–9559, 2020, doi: 10.1109/TIE.2019.2952810.

[71] N. Sun, Di. Liang, Y. Wu, Y. Chen, Y. Qin, and Y. Fang, "Adaptive Control for Pneumatic Artificial Muscle Systems with Parametric Uncertainties and Unidirectional Input Constraints," *IEEE Trans. Ind. Informatics*, vol. 16, no. 2, pp. 969–979, 2020, doi: 10.1109/TII.2019.2923715.

[72] M. Kulkarni, T. Shim, and Y. Zhang, "Shift dynamics and control of dual-clutch transmissions," *Mech. Mach. Theory*, vol. 42, no. 2, pp. 168–182, 2007, doi: 10.1016/j.mechmachtheory.2006.03.002.

[73] S. Kahlbau and D. Bestle, “Optimal shift control for automatic transmission,” *Mech. Based Des. Struct. Mach.*, vol. 41, no. 3, pp. 259–273, 2013, doi: 10.1080/15397734.2012.756719.

[74] K. L. Kuo, “Simulation and analysis of the shift process for an automatic transmission,” *World Acad. Sci. Eng. Technol.*, vol. 76, no. 4, pp. 341–347, 2011.

[75] P. Walker, B. Zhu, and N. Zhang, “Powertrain dynamics and control of a two speed dual clutch transmission for electric vehicles,” *Mech. Syst. Signal Process.*, vol. 85, pp. 1–15, 2017, doi: 10.1016/j.ymssp.2016.07.043.

[76] Q. Zhang and X. Liu, “Optimization of the Quality of the Automatic Transmission Shift and the Power Transmission Characteristics,” *Energies*, vol. 15, no. 13, pp. 1–15, 2022, doi: 10.3390/en15134672.